DEVELOPMENT AND IMPLEMENTATION OF A WORKFLOW FOR MEASUREMENT OF SURFACE TEMPERATURE BY MEANS OF INFRARED THERMOGRAPHY
AND
THERMODYNAMIC AND ECONOMIC ANALYSIS OF THE INCORPORATION OF THE SUPERCRITICAL CARBON DIOXIDE BRAYTON CYCLE INTO COMBINED CYCLE POWER PLANTS

A Thesis
Presented to
The Academic Faculty

By

Jacob Austin Cloward

In Partial Fulfillment
of the Requirements for the Degree
Master of Science in the
School of Mechanical Engineering

Georgia Institute of Technology
University of Stuttgart

August 2020

DEVELOPMENT AND IMPLEMENTATION OF A WORKFLOW FOR MEASUREMENT OF SURFACE TEMPERATURE BY MEANS OF INFRARED THERMOGRAPHY
AND
THERMODYNAMIC AND ECONOMIC ANALYSIS OF THE INCORPORATION OF THE SUPERCRITICAL CARBON DIOXIDE BRAYTON CYCLE INTO COMBINED CYCLE POWER PLANTS

Approved by:

Dr. Devesh Ranjan, Advisor
School of Mechanical Engineering
Georgia Institute of Technology

Dr. Peter Loutzenhiser
School of Mechanical Engineering
Georgia Institute of Technology

Dr.-Ing Rico Poser, Advisor
Faculty for Aerospace Engineering
University of Stuttgart

Prof.Dr.-Ing.Dr.h.c. Oliver Sawodny
Faculty for Mechanical Engineering
University of Stuttgart

Date Approved: July 10, 2020

ACKNOWLEDGEMENTS

This work would of course not have been possible without the support of my advisors, Dr. Devesh Ranjan at Georgia Tech and Dr.-Ing. Rico Poser at the University of Stuttgart. I would like to thank them, along with my other thesis reading committee members, Dr. Peter Loutzenhiser and Prof. Dr. Oliver Sawodny. I am also grateful to Prof. Sawodny for his guidance in his role overseeing the joint master's program, as I am to his counterparts in Atlanta, Dr. Paul Neitzel and Dr. Andrei Fedorov.

I had the pleasure of completing part one of my thesis as part of an internship at Robert Bosch GmbH, where I won the lottery in having Dr.-Ing. Marco Lorenz as my supervisor. I am greatly indebted to him for his mentorship, patience, and confidence in my abilities. I would also like to thank Joachim "Joe" Schmid, Maik Doil, and Marius Imiolcyzk, whose support and companionship made my time at Bosch more successful and enjoyable.

Thanks should also go to Stefanie Herre and Stefan Schaut, of the Institute for System Dynamics at the University of Stuttgart, for providing structure to help me overcome my "inner pig-dog", proof-reading my drafts, and encouraging me to complete the document.

I would also like to express my appreciation to all the members of the Shock Tube and Advanced Mixing lab at Georgia Tech, especially Sandeep Pidaparti, who was my primary mentor there and suggested the topic for part two of my thesis, as well as Stephen Johnston, who showed me the ropes and helped me to feel more a part of the lab. I gratefully acknowledge Shrey Baid's help in the early stages of information gathering for my thesis.

I owe particular thanks to those who provided emotional support while I worked on this thesis. Many thanks to Jay, Kiri, Stefan, and Frau Renner, to Alex and all the other Stuggi Super Friends, and to Alex Olson. I'm extremely grateful to my family, both immediate and extended, for their cheers and empathetic ears. Most of all I am grateful to my wife, Anna, who bore the brunt of the ups, downs, and roundabouts that have accompanied my efforts to complete this thesis and its associated degree.

TABLE OF CONTENTS

LIST OF TABLES

LIST OF FIGURES

LIST OF SYMBOLS

Latin Symbols

a_0, b_0	m	coefficients used in plane projective transformation
a_1, a_2, b_1, b_2	$\mathrm{m/pixel}$	coefficients used in plane projective transformation
b	$\mathrm{arbitrary\,units}$	experimentally calibrated parameter
Bi	$-$	Biot number
c	$2.998 \times 10^8 \mathrm{m/s}$	speed of light
c_1, c_2	$1/\mathrm{pixel}$	coefficients used in plane projective transformation
$c_{p,n}$	$\mathrm{arbitrary\,units}$	coefficients determined by pixelwise radiometric self calibration
f	$\mathrm{arbitrary\,units}$	experimentally calibrated parameter
f_{plant}	$-$	plant utilization factor
h	$6.626 \times 10^{-34} \mathrm{J\,s}$	Planck's constant
h	$\mathrm{W/(m^2K)}$	heat transfer coefficient
h	$\mathrm{kJ/kg}$	specific enthalpy
I^*	$\mathrm{W/m^2}$	irradiance
I	$\mathrm{arbitrary\,units}$	scaled irradiance
I_{offset}	$\mathrm{arbitrary\,units}$	experimentally calibrated parameter
k	$\mathrm{W/(m\,K)}$	thermal conductivity
k_B	$1.3806 \times 10^{-23} \mathrm{m/s}$	Boltzmann's constant
$\dot{m}$	$\mathrm{kg/s}$	mass flow ratio

N	$-$	order of polynomial relating detector signal to scaled irradiance
P	kPa or MPa	pressure
Q	$-$	number of images used for pixelwise radiometric self calibration
$\dot{Q}$	kW	heat transfer rate
r	$\mathrm{arbitrary\ units}$	experimentally calibrated parameter
r_d	$-$	discount rate
r_{tax}	$-$	tax rate
s	$\mathrm{kJ/(kg\ K)}$	specific entropy
T	K or $^\circ\mathrm{C}$	temperature
t	$\mu\mathrm{s}$	integration time
$t_{\text{plant life}}$		expected lifetime of plant
U	$-$	detector signal
W	$\mathrm{W/(sr\ m^3)}$	spectral radiant emittance
$\dot{W}$	kW	power
X	m	horizontal coordinate in the object plane
x	pixels	horizontal coordinate in the image plane
X	$-$	H_2O quality
X	$-$	arbitrary monetary quantity
Y	m	vertical coordinate in the object plane
y	pixels	vertical coordinate in the image plane
y	$-$	fraction of mass flow split

Greek Symbols

α	$-$	absorptivity
ε	$-$	emissivity

ϵ	$-$	error minimized in pixelwise radiometric self calibration
η	$-$	efficiency
λ	m	wavelength
ρ	$-$	reflectivity
σ	$\mathrm{arbitrary\ units}$	standard deviation
τ	$-$	transmissivity

Indices

amb	ambient
atm	atmospheric
b	for a blackbody
cc	combustion chamber
cold	cold fluid
$comp$	compressor
e	units of electrical energy
el	electrical
ec	economizer
ev	evaporator
fj	joining of a split flow
hot	hot fluid
in	inlet
IR	as measured with infrared camera with in situ calibration
k	for a given image combination
$lens$	for the lens
NUC	nonuniformity corrected

obj	for the object of interest
out	outlet
$mech$	mechanical
p	for a given pixel
pp	pinch point
PV	present value
q	for a given image
Rec	recuperator
s	for an isentropic process
sh	super heater
TC	as measured with a thermocouple
turb	turbine
0	excluding reflected ambient radiation (as in $I_{\text{offset},0}$)
1	pertaining to image 1 (as in I_1 in NUC determination)
2	pertaining to image 2
%	on a percentage basis

Abbreviations

CCPP	combined cycle power plant
CR	compression ratio
EES	engineering equation solver (Fchart Software)
Eff	heat exchanger effectiveness
HDR	high dynamic range
HEX	heat exchanger
HRSG	heat recovery Steam generator

HTR	high temperature recuperator
LCOE	levelized cost of electricity
LMTD	log mean temperature difference
LTR	low temperature recuperator
NG	natural gas cycle
NUC	nonuniformity correction
O&M	operation and maintenance
sCO_2	supercritical carbon dioxide
SLDS	straight line depreciation schedule
TCCPP	traditional combined cycle power plant
WHR	waste heat recovery

SUMMARY

In part one a workflow for the measurement of surface temperature by means of infrared thermography using a semi empirical equation based on Planck's law of radiation is designed and implemented in Matlab. Procedures for acquiring scaled irradiance from camera detector signal using pixelwise radiometric self calibration and nonuniformity correction are described and implemented. Thermographic images are rectified using a plane projective transformation to transform pixel location into physical locations on the object plane. Parameters of the semi empirical equation for the determination of temperature from scaled irradiance are precalibrated. A procedure for the determination of surface emissivity is designed and employed to determine the emissivity of various surface coatings. A method for in situ calibration of the relationship between temperature and scaled irradiance is shown and used for subsequent measurements. Experiments are carried out for validation of the technique. For the in situ adjustment of a single parameter with the support of a single thermocouple, a measurement uncertainty of 2 K is found, and for the case of two parameter adjustment with support from two thermocouples, a measurement uncertainty of 1.2 K is found.

In part two the profitability of several combined cycle power plant layouts incorporating supercritical carbon dioxide Brayton bottoming cycles is investigated comparative to traditional combined cycle power plants. Estimated levelized cost of electricity and steady state design point thermodynamic analysis are used to determine profitability. Five supercritical carbon dioxide cycle layouts are investigated both as a replacement to and in tandem with the traditional steam Rankine bottoming cycle. High uncertainty in cost estimation and limitations of the constraints in the thermodynamic model prevent a definitive conclusion, but the results suggest that the incorporation of supercritical carbon dioxide cycles into combined cycle power plants has the potential to improve upon traditional combined cycle power plants in terms of profitability.

CHAPTER 1
BRIEF INTRODUCTION

This work is composed of two parts, each of which explores a separate topic.

Part one outlines a procedure developed to facilitate surface temperature measurement with infrared thermography. An infrared camera measures the amount infrared light within a given wavelength range incident on its detectors. The relationship between the temperature of an object and the radiation it emits is well established, but a host of environmental factors beyond object temperature influence the irradiance that reaches and is measured by a camera detector. These factors include, among others, ambient temperature and radiation, object surface emissivity, and transmissivity of lenses and the air between camera and object. Effective temperature measurement by means of infrared thermography therefore requires calibration to account for such factors. Additional aspects required of the procedure include digital detector signal interpretation, the correction of nonuniformities between camera detectors, and spatial rectification of the thermographic images.

Part two investigates potential layouts of combined cycle power plants incorporating supercritical CO_2 Brayton power cycles for waste heat recovery, comparing options to the well established technology of traditional combined cycle power plants in terms of profitability. In order to make this comparison, costs must be estimated for both the traditional and theoretical power plant layouts. A thermodynamic analysis models the layouts' performance characteristics, such as electrical power output and efficiency, which are used to determine how cost effectively electrical energy can be produced as a means of comparing potential profit margins.

Beyond authorship and a general relationship to thermodynamics there is no significant connection between the two parts.

PART 1

DEVELOPMENT AND IMPLEMENTATION OF A WORKFLOW FOR MEASUREMENT OF SURFACE TEMPERATURE BY MEANS OF INFRARED THERMOGRAPHY

CHAPTER 2
BACKGROUND

2.1 Surface Temperature Measurement

Surface temperature measurement is important for the characterization of many heat transfer applications. There are many techniques for surface temperature measurement.

One of the most common and simplest methods is measurement with thermocouples, which are relatively cheap, can measure a large range of temperatures and there are many types, ideal for diverse conditions [1]. Thermocouples are less well suited for applications where surface temperature needs to be measured with a relatively high spatial resolution. Under such circumstances a high quantity of thermocouples is required and their application can be time consuming and costly.

The liquid crystal temperature measurement technique, reviewed in detail by Ireland and Jones [2], allows for global measurement across a surface by relying on the preferential reflection of light in the visible range by the liquid crystals. This method can be applied in temperature ranges referred to as bandwidths or color play corresponding to the transition of the crystals between solid and liquid states. The broadest bandwidth for any crystal is about 20 K, and the temperatures that can be measured by liquid crystal range from -30 °C to 115 °C. The technique is well suited for transient measurements such as those carried out by Poser *et al.* [3], but ill-suited for instantaneous steady state measurement of surfaces where there are higher temperature differences.

Thermographic phosphor thermometry uses luminescence lifetime to measure temperature across a wide range of temperatures. [4] At higher temperatures highly time resolved measurements are required when luminescence lifetimes drop below $4 \times 10^{-3} s$.

Temperature sensitive paint can also be used to measure surface temperature using light

in the visible range. Lorenz *et al.* [5] developed a procedure with temperature sensitive paint capable of measuring temperatures between 270 K and 430 K.

Infrared thermography makes use of the electromagnetic radiation in the infrared range emitted from a surface of interest to determine temperature. It can deliver spatially resolved surface temperature data when calibrated properly. Martiny *et al.* [6] developed an in situ calibration procedure which was further developed by Ochs *et al.* [7] and made applicable for high dynamic range (HDR) images, making a broader range of temperatures measurable in a single image by Ochs *et al.* [8].

2.2 Infrared Thermography

All matter emits thermal radiation. Infrared thermography involves measuring the thermal radiation incident on the camera detectors, also known as thermal irradiance, from the object of interest. The irradiance is then used to determine the temperature of an object. Many factors need to be taken into account for such calculation to be performed.

Planck's law of radiation describes the relationship between temperature and spectral radiant emittance for an ideal radiator, also known as a blackbody.

$$W_b(\lambda, T_{obj}) = \frac{2\pi hc^2}{\lambda^5(e^{\frac{hc}{\lambda k_B T_{obj}}} - 1)} \tag{2.1}$$

where $W_b(\lambda, T_{obj})$ is the spectral radiant emittance of a blackbody at temperature T_{obj}, h is Planck's constant, c is the speed of light, k_B is Boltzmann's constant, and λ is the wavelength.

In reality, objects emit only a fraction of the thermal radiation emitted by a blackbody. This fraction is referred to as the emissivity, ε. Emissivity can vary with wavelength, temperature and angle. A graybody is a body whose emissivity does not vary with wavelength. The objects in this work are treated as graybodies within the spectral range of camera sen-

sitivity. The spectral emittance of a graybody with emissivity ε_{obj} can be expressed as

$$W_{obj}(\lambda, T_{obj}) = \varepsilon_{obj} \cdot W_b(\lambda, T_{obj}) = \varepsilon_{obj} \cdot \frac{2\pi hc^2}{\lambda^5(e^{\frac{hc}{\lambda k_B T_{obj}}} - 1)}. \tag{2.2}$$

This expression can be rearranged to present T_{obj} as a function of W_{obj}:

$$T_{obj} = \frac{\frac{hc}{\lambda k_B}}{ln(\frac{\varepsilon_{obj} 2\pi hc^2}{\lambda^5 W_{obj}(\lambda, T_{obj})} + 1)}. \tag{2.3}$$

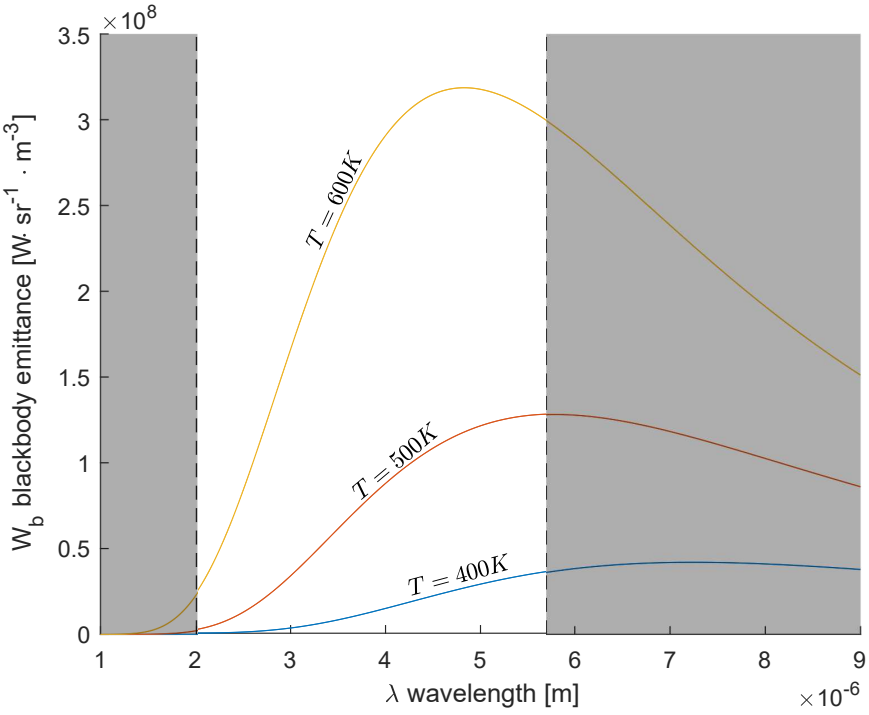

Figure 2.1: Blackbody emittance relative to detector wavelength range

Figure 2.1 shows the radiant emittance $W_b(\lambda, T)$ of blackbodies with temperatures of $400K$, $500K$, and $600K$ according to Planck's law with the spectral detector range where the InfraTec ImageIR 8340 hp S, the infrared camera used for this work, is sensitive to radiation superimposed. A data sheet for the camera can be found in appendix A.1. The camera's InSb infrared detectors are capable of detecting thermal radiation of wavelengths between $2.0\mu m$ and $5.7\mu m$. The plot background is white within the detector range with

the wavelengths out of range shown in gray. The figure therefore demonstrates the thermal radiation emitted by a blackbody that could be detected by the infrared camera.

The radiation incident on the camera will differ from the radiation emitted by the body of interest. While W_{obj} is the radiation emitted by the object, the information available to the infrared detectors in the camera is the irradiance, or the total radiation incident upon the detector, over the detector's spectral range of sensitivity. The irradiance is a function of the object emmitence, but is also influenced by detector geometry, the optical path through which the radiation travels, radiation of the surroundings, and other factors:

$$I = f(\int_{t_0}^{t}\int_{\lambda_{min}}^{\lambda_{max}} W_{obj}\, d\lambda dt,\ \text{detector geometry},\ \text{optical path},\ \text{surroundings}, etc.). \tag{2.4}$$

Moreover, the value I obtained from the detector signal is the actual irradiance I^* multiplied by an unknown arbitrary factor. The procedure for determining I from the electrical output signal U of the detector is discussed in section 3.3.

Martiny *et al.* [6] and subsequently Ochs *et al.* [7] used a semi empirical equation of a similar form to Planck's law as expressed in equation 2.3 for use in infrared thermography which makes use of scaled irradiance I in the place of W_{obj} and wavelength λ dependence:

$$T_{obj} = \frac{b}{ln(\frac{r}{I - I_{offset}} + f)}. \tag{2.5}$$

With proper calibration of the parameters b, r, f, and I_{offset}, scaled irradiance, due to its relationship with emittance, can be used to successfully measure temperature. These parameters will be specific to the camera used for measurement and may also vary with other factors in measurement setup.

Because the equation mimics the form of Planck's law, it is possible to represent the underlying physics described by Planck's law, while the calibrated adjustment allows for flexibility where the many factors affecting measurement quickly become too complex to account for analytically.

Because of their empirically determined nature, the exact physical meaning of these parameters is elusive, but a comparison of equation 2.3 and equation 2.5 reveals the general role of each parameter. The parameter b can be seen to have a wavelength dependence and corresponds otherwise only to physical constants and can therefore be expected to vary little so long as basic measurement setup and the units of scaled irradiance and temperature are consistent. The parameter f, which corresponds only to the scalar 1 in 2.3, can similarly be expected to vary little. The parameter r corresponds to physical constants, but also scales with emissivity, ε . The parameter I_{offset} is introduced to account for the irradiance incident on the camera from sources other than the object of interest, such that

$$I_{obj} = I - I_{\text{offset}}, \tag{2.6}$$

where I_{obj} is the irradiance measured by the camera due to the emittance of the object of interest.

The need for this parameter becomes clear with investigation of figure 2.2, which symbolizes a typical infrared thermography measurement situation. Each detector in the camera measures irradiance, which can come from several sources, though only the irradiance from the object is of interest. The surroundings, the atmosphere, and even the lens and other camera parts emit radiation that can contribute to the irradiance registered by the detectors. In the figure, the total irradiance I incident on the camera detector would be

$$I = I_{obj} + I_{amb} + I_{atm} + I_{lens}. \tag{2.7}$$

The magnitude of each of the contributing irradiances is dependent on, in addition to temperature, physical properties of the matter they are emitted from and passed through.

When thermal radiation is incident on an object or surface, the material will transmit, reflect, or absorb the radiation. Absorbtivity, α, transmissivity, τ, and reflectivity, ρ, are material properties that describe what fraction of the incident radiation is absorbed, trans-

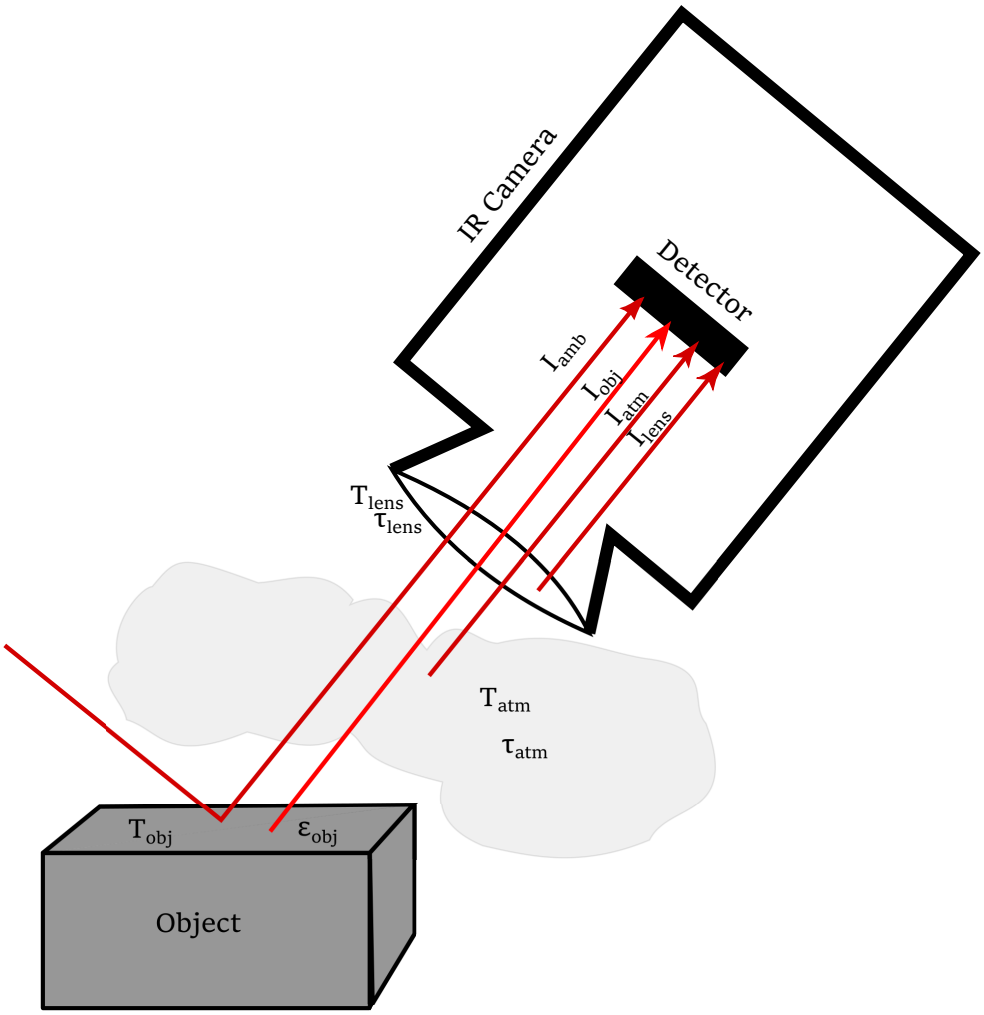

Figure 2.2: Thermal irradiance influenced by surroundings

mitted, or reflected. The sum of the three will always equal one.

$$\alpha + \tau + \rho = 1. \tag{2.8}$$

In the case of an opaque surface, $\tau = 0$, and therefore

$$\alpha + \rho = 1. \tag{2.9}$$

In addition to being an ideal radiator ($\varepsilon = 1$), a blackbody also absorbs all radiation incident upon it ($\alpha = 1$). Kirchhoff's law further describes that the emissivity of a body is

equal to its absorptivity. Therefore the emissivity of an opaque object can be described as

$$\varepsilon = \alpha = 1 - \rho. \tag{2.10}$$

To return to figure 2.2, I_{obj} would then be the thermal radiation emitted from the object in the direction of the detector (which itself includes a factor of the object emissivity, ε_{obj}), multiplied by the factors τ_{atm} and τ_{lens}, the transmissivities of the things it passes through. I_{amb}, which results from a reflection of surrounding radiation off of the object would include the factor $\rho_{obj} = (1 - \varepsilon_{obj})$.

The interplay between all of these factors is further complicated in measurement situations with additional elements. Some infrared measurements, for instance, measure temperatures of a surface inside of an enclosure with use of a window made of sapphire or another material with high transmissivity in the infrared range.

It is impractical to measure and account for all of these various factors directly, especially as some of these factors may change from measurement to measurement. By calibrating the parameters b, r, f, and I_{offset} from 2.5, these factors can be accounted for. Due to its dependence on surroundings, the parameter I_{offset} is expected to be most highly variable and to require in situ calibration for accurate temperature measurement.

2.3 Objectives

Building off of the procedure outlined by Ochs *et al.* [7], this work will establish a workflow for surface temperature measurements using the InfraTec ImageIR 8340 hp S infrared camera with Matlab scripts for processing and calibration.

This includes preparation of the infrared thermographic measurement, such as the determination across integration times of scaled irradiance from detector signal, nonuniformity correction, and rectification of the image plane.

Temperature will then be determined from scaled irradiance by in situ calibration with

the use of a thermocouple, aided by precalibration and emissivity determination processes.

Finally, an example measurement will be carried out, demonstrating the system and its application producing high dynamic range thermographic images, thereby validating the measurement procedure and quantifying the measurement uncertainty.

CHAPTER 3
INFRARED IMAGE PREPARATION

In order to determine surface temperature of an object by thermographic means, infrared detector input and output must be appropriately handled. The detector input is the thermal irradiance incident on the detector, which, as discussed in section 2.2, includes the radiation emitted from the object of interest as well as ambient radiation. The process of determining object temperature from irradiance is discussed in chapter 3. The focus of this chapter is determining thermal irradiance (detector input) from detector signal (detector output).

This requires understanding of the relationship between irradiance, integration time, and the detector signal, eliminating infrared data that is not in a useful range, defining the function relating irradiance, integration time and detector signal for each pixel through the process of pixelwise radiometric self calibration, and making each pixel comparable to the others through nonuniformity correction.

3.1 Integration Time

The infrared detector signal is dependent not only on the irradiance, but also on the integration time, which is the amount of time for which the detector records its exposure to thermal radiation.

The irradiance multiplied by integration time, $t \cdot I^*$, is referred to as the exposure. The detector signal, U, is then some unknown function of the exposure:

$$U = f(t \cdot I^*). \tag{3.1}$$

Figure 3.1 shows the approximate expected shape of the relationship between exposure and detector signal. There is a portion, known as the linear range, where the relationship

is nearly linear. Above a certain exposure value, the detector is saturated. Outside of the linear range, the detector signal is no longer useful for determining irradiance.

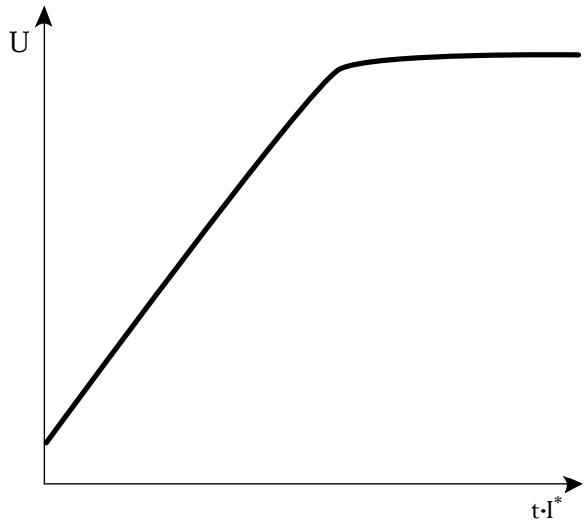

Figure 3.1: Expected detector signal exposure relationship

Because the detector signal is a function of the product of the two values, a scaling of either the integration time or the irradiance will have the same effect on the detector signal. The relationship can therefore be characterized based on the variation of integration time with a constant irradiance.

A comparison of the images in figure 3.2 and demonstrates the impact of integration time on detector signal. The two images are measurements of the same isothermal object at the same temperature, with the only difference being that the image in figure 3.2a was taken with an integration time of 2000 μs and the image in figure 3.2b was taken with an integration time of 200 μs. Represented in each of the images is the raw detector signal of each pixel. Detector signal values can range from 0 to $2^{14} - 1$. In these particular images, any value less than or equal to 1500 is depicted as black and any value greater than or equal to 9000 is depicted as white, with the values in between on the grayscale. The longer integration time allows for more light exposure and therefore a higher detector output value.

The usefulness of integration time variation to determine detector response is demon-

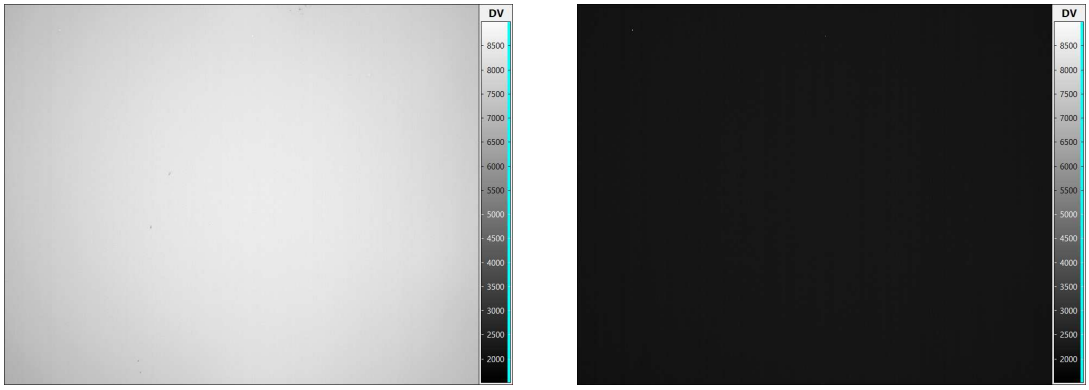

(a) $t = 2000\mu s$ (b) $t = 200\mu s$

Figure 3.2: Thermograms of an isentropic surface with differing integration times, t

strated in figure 3.3, which shows the detector signal values of three arbitrarily chosen pixels from images taken of an isothermal surface at 21°C (and therefore uniform thermal radiation) with various integration times. The linear range is apparent, and it is clear that with too high of an integration time, the detector signal is no longer useful in determining irradiance and subsequently temperature. It can also be noted that the three detectors have a slightly different response to the same irradiance, which underscores the importance of determining the response function for each pixel individually.

As long as all acquired detector values are within the linear range, the same information on irradiance can be extracted from each image. Integration time should be selected according to the level of irradiance such that detector values are within the linear range, where irradiance and detector signal are proportional. In this range, meaningful calibrations can be applied to determine temperature. An integration time between 1000 and 3000 μs would for example be an appropriate match for measurements of the object and temperature represented in the figure 3.3.

For measurements with a high difference in local surface temperature it is necessary to incorporate two or more integration times into one high dynamic range image. The Irbis software can be used to take high dynamic range images, but only with the calibrations included with the software, and only the resultant combined images are accessible. The

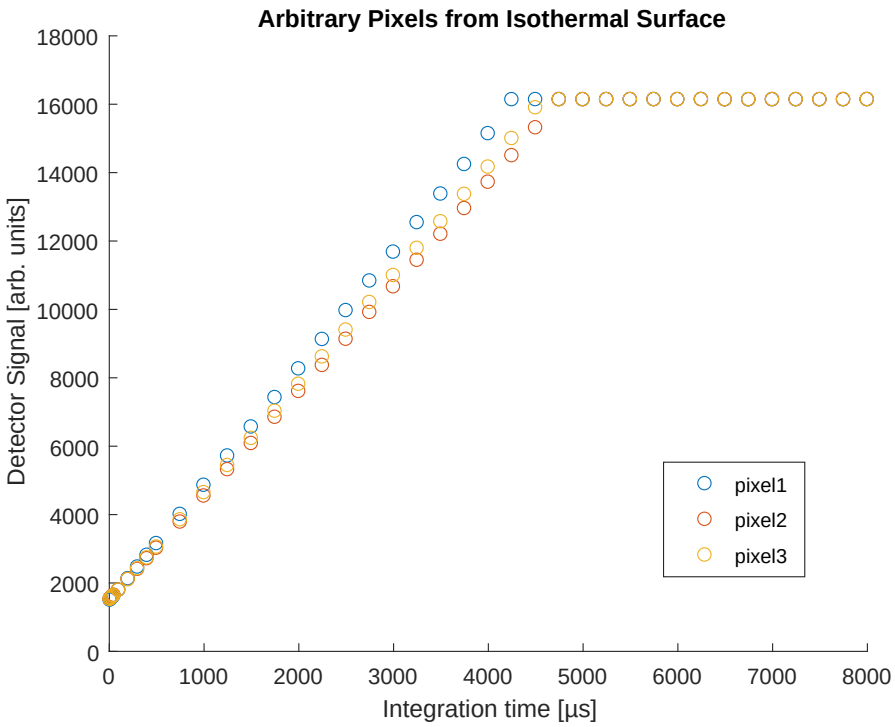

Figure 3.3: Detector signal response to integration times

software provides no way to programmatically adjust integration time without appling the irbis calibrations, and so to obtain raw data for high dynamic range images, measurements at one integration time must first be made, followed by those at another. For this reason it is especially important that such measurements be made under steady state conditions.

3.2 Elimination of Unhelpful Pixels

Thermographic images, made up of an array of camera detector signals corresponding to pixels, are saved from the irbis software as ASCII files, which are then read into Matlab for further processing.

In order to limit the data to pixels well within the linear range of the detector, any values greater than 80% or less than 20% of the maximum possible detector signal value $(2^{14} - 1)$ are eliminated by replacement with NaN (not a number) values. These cutoffs, which are represented by the dashed lines in figure 3.4 (which depicts the same data as figure 3.3),

are arbitrarily chosen, but ensure that the detector signal values to be analyzed are within the linear range and will yield meaningful irrandiance values. The detector signal values are then normalized to range from 0 to 1, for the sake of convenience.

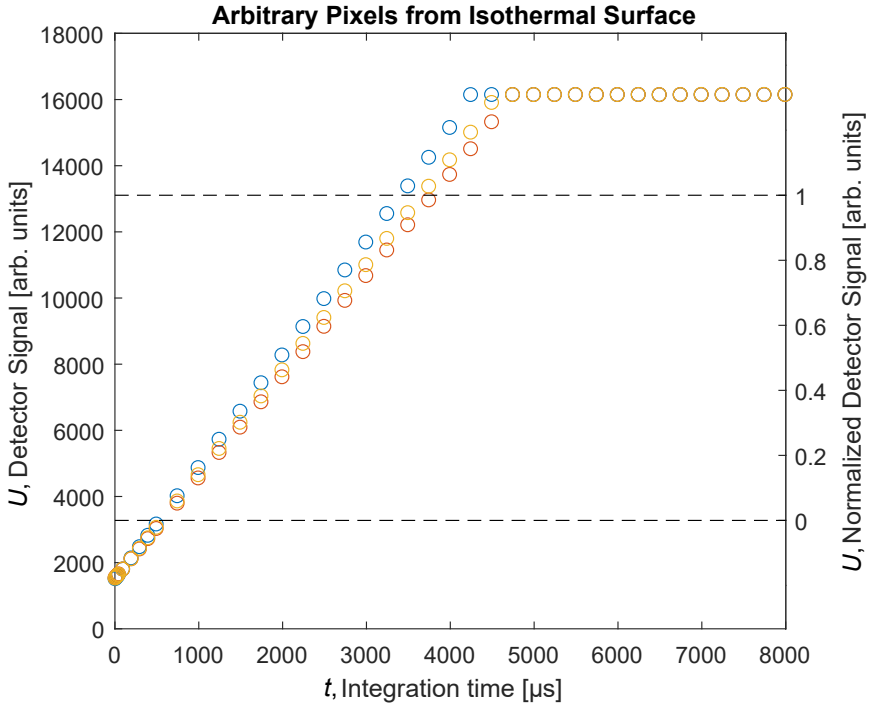

Figure 3.4: Detector signal response to integration times with cutoff values

Of the more than 300,000 detectors in the focal plane array of the Infratec ImageIR 8340 hp S infrared camera, a few consistently provide detector values well outside of the acceptable range. The author elects to eliminate the resulting bad pixels by replacement with NaN values.

3.3 Conversion of Detector Signal to Scaled Irradiance through Pixelwise Radiometric Self Calibration

The function relating the output signal of each detector to the integration time and the thermal irradiance incident upon that detector can be approximated as a polynomial such

that:

$$I_p = \frac{1}{t} \sum_{n=0}^{N} c_{p,n} \cdot U_p^n, \tag{3.2}$$

where I_p is the scaled irradiance of a given pixel, t is the integration time, U_p is the detector signal of said pixel, $c_{p,n}$ are the coefficients that must be determined for the pixel, and N is the order of the polynomial used.

It can be noted that although the usable range of the detector is refered to as the linear range, and the detector signal is very nearly directly proportional to the exposure $t \cdot I$, the small terms added by the use of a second order polynomial ($N = 2$) led to noticable improvements in temperature measurements. Therefore second order polynomials are used.

The coefficients $c_{p,n}$ are found using a procedure for radiometric pixelwise self calibration based on the one outlined by Ochs [9].

A series of thermographic images are taken of an isothermal surface, all at the same temperature, but at varying integration times.

The coefficients are then found for each pixel by solving the least squares problem minimizing the error ϵ_p:

$$\epsilon_p = \sum_{q=1}^{Q-1} \sum_{k=1}^{Q-q} \left[\sum_{n=0}^{N} c_{p,n} \cdot U_{p,q}^n - \frac{t_q}{t_{q+k}} \sum_{n=0}^{N} c_{p,n} \cdot U_{p,q+k}^n \right]^2, \tag{3.3}$$

where Q is the number of images used. The interaction between the indices q and k ensures that each possible combination of images is used to help determine the coefficients.

With this method, irradiance can only be found scaled by some unknown factor. The coefficients must then be arbitrarily constrained, and for mathematical convenience the requirement is applied that

$$\sum_{n=0}^{N} c_{p,n} = 1. \tag{3.4}$$

Once the self calibration has been performed and coefficients are determined, these can be applied to images taken with the same camera with the use of equation 3.2.

3.4 Nonuniformity Correction (NUC)

In the radiometric pixelwise self calibration each pixel is handled individually, meaning each has been scaled differently and no correction has been made for other nonuniformities caused by the optical path. The radial variation of scaled irradiance in figure 3.5, which features a measurement of an isothermal surface that has been transformed from detector signal to scaled irradiance, demonstrates this nonuniformity and the need for a correction.

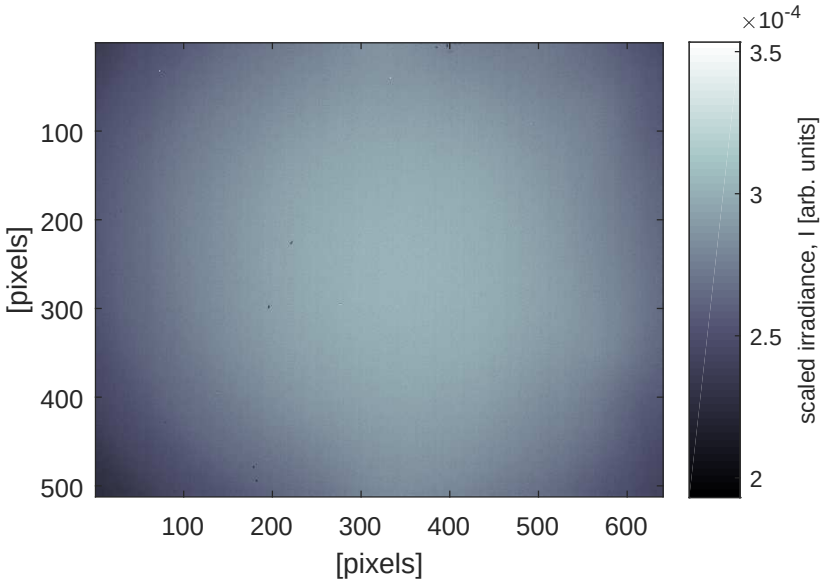

Figure 3.5: Thermographic image of an isothermal surface without NUC

The nonuniformity correction (NUC) is meant to even out the values of all the pixels so that they have meaning relative to one another and can be directly compared, which is essential for temperature measurement.

One method for quantifying nonuniformity takes the form

$$\text{nonuniformity} = \frac{\sigma}{\bar{I}} \cdot 100\%, \tag{3.5}$$

where σ is the standard deviation of the set of all pixel scaled irradiance values from an image and $\bar{I}$ is the average scaled irradiance value. The image in figure 3.5 has a nonuniformity of 5.6%.

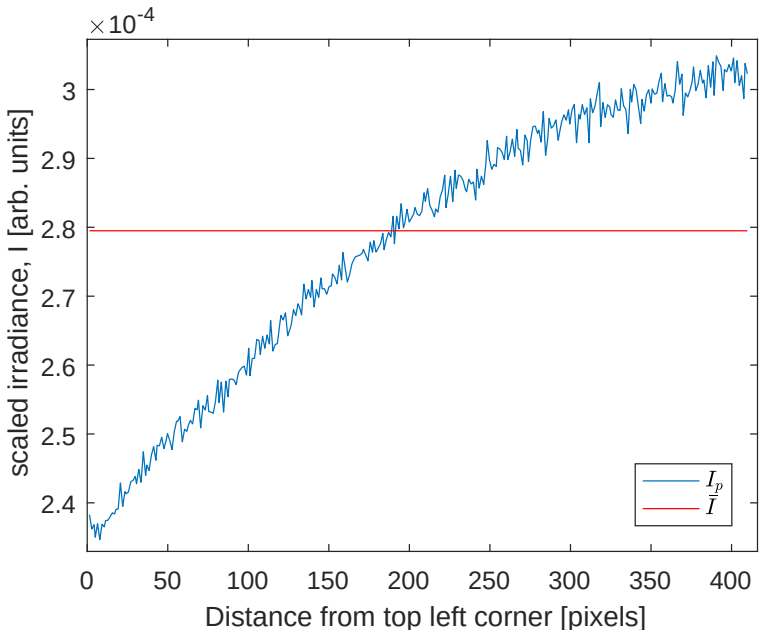

Figure 3.6: Pixel scaled irradiance values along diagonal and average value

Figure 3.6 plots the scaled irradiance values of the pixels along the diagonal from the top left corner to the center of the thermographic image in figure 3.5. An ideal NUC, when applied to a measurement of a perfectly isothermal surface would transform the value of each pixel to the average value, $\bar{I}$.

The NUC is applied to each pixel as a linear function of the scaled irradiance:

$$I_{\text{NUC},p} = \text{Slope}_{\text{NUC},p} \cdot I_p + \text{Intercept}_{\text{NUC},p} \tag{3.6}$$

The NUC slope and intercept for each pixel are determined by a two point NUC, which operates on the basis of images of two isothermal surfaces, each at different temperatures. A two point NUC provides not only an offset adjustment but accounts for the difference in detector response as scaled irradiance increases or decreases.

Then, because each pixel in either image of an isothermal surface would ideally have the same value as all other pictures in the image, pixel values can be linearly adjusted to fit the rest of the image.

The NUC slope can be found by

$$\text{Slope}_{\text{NUC},p} = \frac{\bar{I}_2 - \bar{I}_1}{I_{p,2} - I_{p,1}}, \tag{3.7}$$

where $\bar{I}_1$ is the average pixel value in the measurement taken at the first temperature and $I_{p,1}$ is the value of an individual pixel, p, taken at the first temperature and $\bar{I}_2$ and $I_{p,2}$ are respectively the average and individual pixel values at the second temperature. The NUC intercept is then found by

$$\text{Intercept}_{\text{NUC},p} = \frac{\bar{I}_2 - \bar{I}_1}{I_{p,2} - I_{p,1}} \cdot I_{p,1} + \bar{I}_1. \tag{3.8}$$

After the NUC slope and intercept have been determined, they can be applied to images taken with the same camera and lens and with the scaled irradiance transformation applied from the same radiometric self calibration.

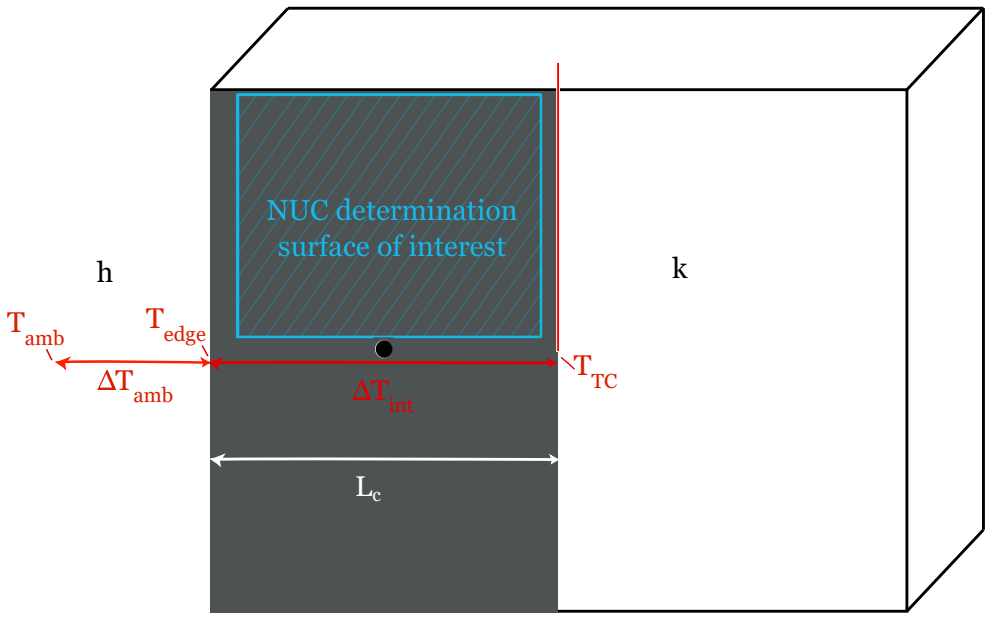

Figure 3.7: Copper Block used for isothermal surface in NUC determination

The above described procedure is applied to determine a NUC which is used throughout this work using a copper block for the isothermal surface. This copper block has measurements of 120mm×90mm×40mm. Half of the top surface is covered with Nextel Velvet

Coating, which is discussed in more detail in sections 4.1 and 4.2. The infrared measurements are taken such that the camera's entire field of view is within the surface of interest, contained within the portion of the block coated with Nextel Velvet Coating, which ensures that emissivity will not vary greatly from pixel to pixel. The block is represented in figure 3.7, with the surface of interest used for the NUC determination marked in blue.

The copper block was chosen for its high thermal conductivity, which in combination with the low heat transfer coefficient from the block to its surroundings by natural convection ensures a homogeneous temperature distribution throughout the copper. The thermal conductivity of copper is $k = 400\frac{W}{mK}$ and heat transfer coefficient between the block and the surroundings is assumed to be $h < 10\frac{W}{m^2K}$. Then, with a choice of characteristic length of $L_C = 60mm$, half the length of the block and slightly more than the width of the surface of interest used for NUC determination, the Biot number is found to be:

$$Bi = \frac{L_C h}{k} < \frac{0.06m(10\frac{W}{m^2K})}{400\frac{W}{mK}} = 0.0015. \tag{3.9}$$

This Biot number is well below 1 and justifies consideration of the copper block as an isothermal mass. To estimate the magnitude of temperature variation within the block, it can be noted that

$$\frac{\Delta T_{int}}{\Delta T_{amb}} = Bi, \tag{3.10}$$

where ΔT_{int} is the temperature difference within the block and ΔT_{amb} is the temperature difference between the block surface and the surroundings. Then, taking $\Delta T_{amb} = 100K$ as a reference,

$$\Delta T_{int} < (0.0015)(100K) = 0.15K. \tag{3.11}$$

The image in figure 3.8 shows the result of applying the NUC to the image in figure 3.5. This corrected image has a nonuniformity of 0.1%, a considerable improvement from the

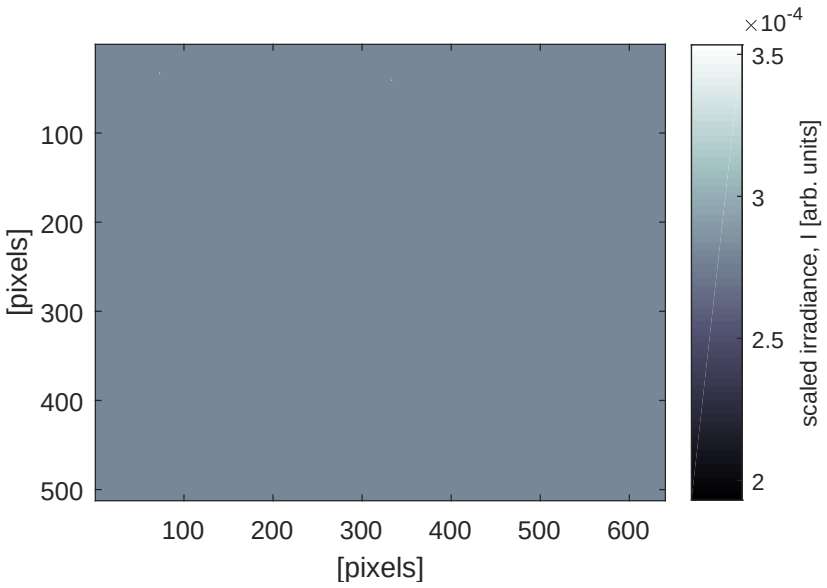

Figure 3.8: Thermographic image of an isothermal surface with NUC

images original nonuniformity, 5.6%. To gain an approximate understanding in terms of temperature measurement, a precalibration (to be discussed in section 4.1) can be applied. This suggests that the uncorrected image yields a total range of approximately 25 K with a standard deviation of 2.4 K, and the corrected image yields a total range of 0.4 K with a standard deviation of 0.05 K. A comparison to the estimated value of temperature variation within the block, $\Delta T_{int} < 0.15$ K (see equation 3.11), reveals an additional uncertainty of $< \pm 0.15$ K. Figure 3.9 plots the scaled irradiance values of the pixels along the diagonal from the top left corner to the center of both the uncorrected and corrected thermographic image in figures 3.5 and 3.8.

3.5 Image Plane Rectification

As the objective of the infrared measurements is to obtain a temperature field, the physical coordinates corresponding to the measured irradiances must also be determined.

The photograph of a copper block in figure 3.10, taken with a digital camera, demonstrates the perspective distortion that needs to be corrected in order to determine the physical coordinates on a surface from the corresponding pixels in the image. This image is taken

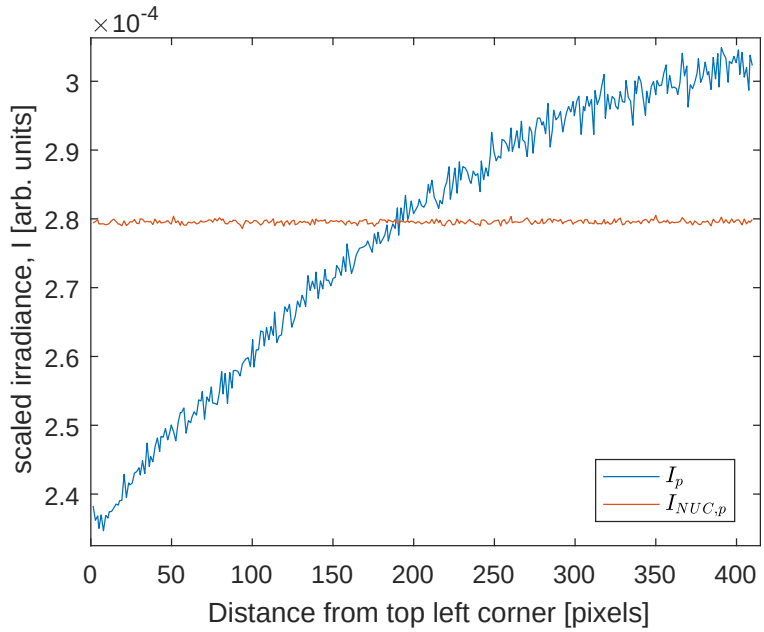

Figure 3.9: Pixel scaled irradiance values along diagonal and average value

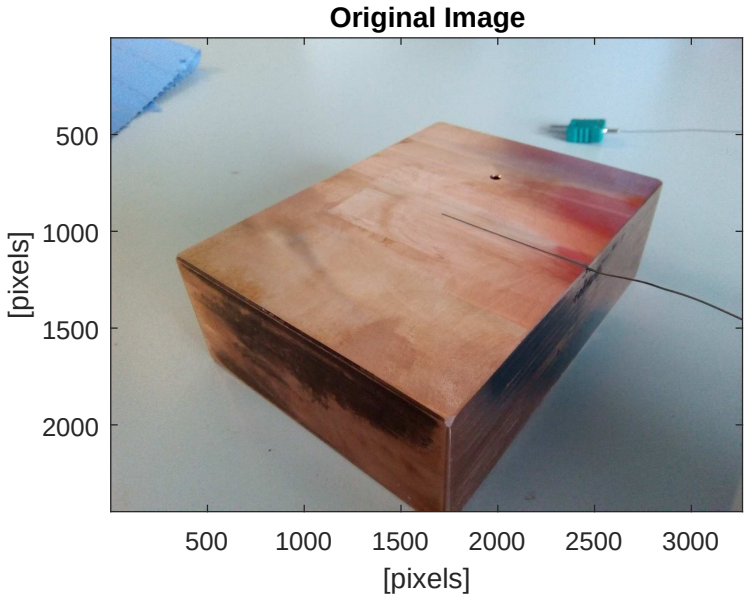

Figure 3.10: Original Photograph of Copper Block

at a much more extreme angle than is typical for a measurement for emphasis, but certain conditions require measurements be made at an angle. In fact, when the measurements are made directly perpendicular to a surface, even with surfaces with high emissivities, there is a danger that the camera will detect the reflection of its own thermal radiation, introducing

considerable error into a measurement. This issue is easily eliminated by taking images at a slight angle such that the reflection is not within the field of view. Even in the case where the image plane and the object plane are perfectly parallel, the image coordinates must be transformed into object coordinates.

The measurements made in this work are all of flat surfaces and it is therefore sufficient to transform the entire image with respect to this single plane. This can be done with a projective transformation of the plane.

Plane projective transformations, discussed in detail by Kyle *et al.* [10], relate the image plane to the object plane with the assumption that projective rays from a point on one plane to the corresponding point on the other all intersect at a single perspective center. Such transformations can be represented mathematically as

$$\begin{aligned} X &= \frac{a_0 + a_1 x + a_2 y}{c_1 x + c_2 y + 1} \\ Y &= \frac{b_0 + b_1 x + b_2 y}{c_1 x + c_2 y + 1}, \end{aligned} \tag{3.12}$$

where X and Y represent coordinates in the object plane, x and y represent coordinates in the image plane, and the eight coefficients must be determined for a given image, which requires four non-collinear points with known coordinates on each plane. In the case of the copper block, the four corners of the top surface are used. For the first of the four points used for the copper block, the coordinates in the object plane are chosen to be an origin at $X = 0$cm and $Y = 0$cm, while the same point corresponds to the pixel values $x = 353$ and $y = 1134$ in the image plane.

Equations 3.12 can be rearranged to form the linear system of equations

$$\begin{aligned} a_0 + a_1 x_i + a_2 y_i - c_1 x_i X_i - c_2 y_i X_i &= X_i \\ b_0 + b_1 x_i + b_2 y_i - c_1 x_i Y_i - c_2 y_i Y_i &= Y_i, \end{aligned} \tag{3.13}$$

with the index i representing known points one through four. These can furthermore be

written in matrix form, from which the coefficients can be easily determined.

$$\begin{bmatrix} 1 & x_1 & y_1 & 0 & 0 & 0 & -x_1X_1 & -y_1X_1 \\ 0 & 0 & 0 & 1 & x_1 & y_1 & -x_1Y_1 & -y_1Y_1 \\ 1 & x_2 & y_2 & 0 & 0 & 0 & -x_2X_2 & -y_2X_2 \\ 0 & 0 & 0 & 1 & x_2 & y_2 & -x_2Y_2 & -y_2Y_2 \\ 1 & x_3 & y_3 & 0 & 0 & 0 & -x_3X_3 & -y_3X_3 \\ 0 & 0 & 0 & 1 & x_3 & y_3 & -x_3Y_3 & -y_3Y_3 \\ 1 & x_4 & y_4 & 0 & 0 & 0 & -x_4X_4 & -y_4X_4 \\ 0 & 0 & 0 & 1 & x_4 & y_4 & -x_4Y_4 & -y_4Y_4 \end{bmatrix} \cdot \begin{bmatrix} a_0 \\ a_1 \\ a_2 \\ b_0 \\ b_1 \\ b_2 \\ c_1 \\ c_2 \end{bmatrix} = \begin{bmatrix} X_1 \\ Y_1 \\ X_2 \\ Y_2 \\ X_3 \\ Y_3 \\ X_4 \\ Y_4 \end{bmatrix} \tag{3.14}$$

The transformation of the copper block is demonstrated in figure 3.11. Outlined in red is the rectangle by the four known points used to define the transformation.

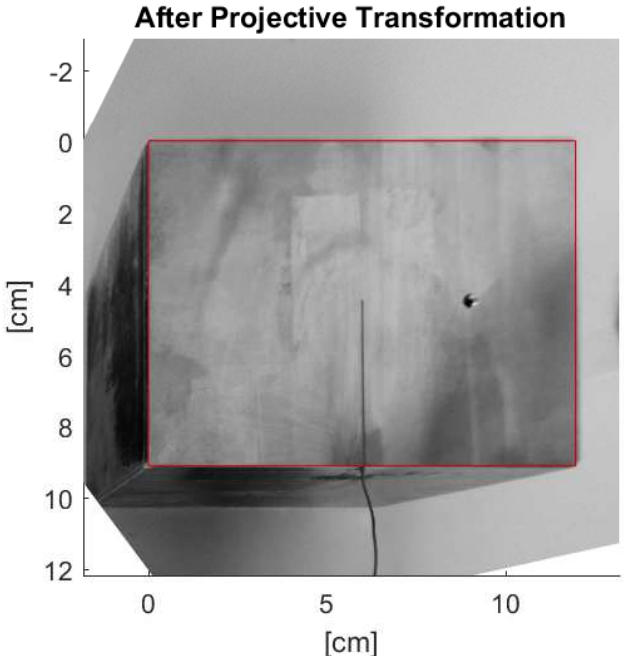

Figure 3.11: Photograph with projection transformation applied

The grid on the graph paper photographed in figure 3.12 helps to demonstrate more closely the effectiveness of the transformation. As can be seen in the close up of the transformed image in figure 3.12b, the calculated object coordinates match the actual object

coordinates well, but the two diverge farther away from the known points used to define the transformation. This is caused largely by radial distortion, which is not taken into account by the projective transformation. In extreme cases a distortion correction would need to be applied, but plane projective transformation is deemed sufficient for the thermographic images in this work.

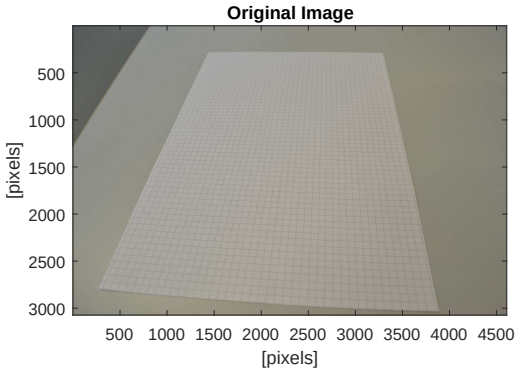

(a) Original photograph

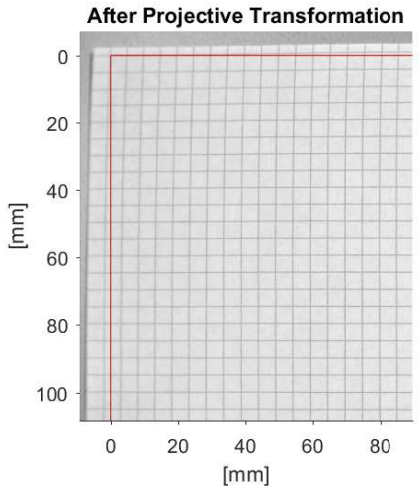

(b) With transformation applied (zoomed in)

Figure 3.12: Photo of graph paper to demonstrate plane projective transformation accuracy

Figure 3.13 demonstrates the plane projective transformation applied to a thermographic image.

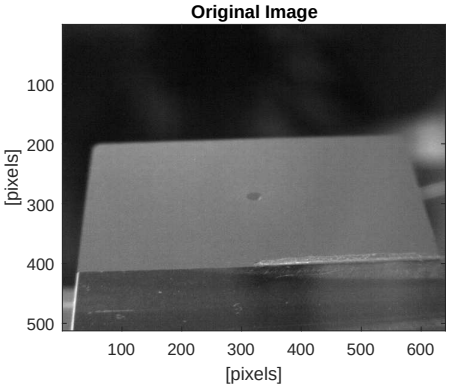

(a) Original

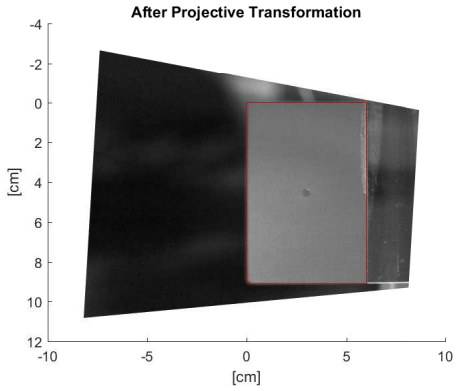

(b) With transformation applied

Figure 3.13: Plane projective transformation of a thermogram

CHAPTER 4
TEMPERATURE DETERMINATION

4.1 Precalibration

In order to measure a gray body's surface temperature by infrared thermography a relation between the surface temperature and the infrared irradiance is needed. In section 2.2 a temperature relation based on Planck's law of radiation has been introduced:

$$T_{obj} = \frac{b}{ln(\frac{r}{I - I_{\text{offset}}} + f)} \qquad \text{(2.5 revisited)}$$

In this relation r, b, f, and I_{offset} are parameters that have to be determined by a precalibration, where I is the scaled irradiance obtained from the detector signal as explained in section 3.3.

In order to determine the four parameters a calibration setup has been designed. It consists of the copper block previously referenced in section 3.4, a hot plate used to heat the block to distinct temperatures, and the infrared camera InfraTec ImageIR 8340 hp S for measuring the infrared irradiance. The setup is shown in figure 4.1. On the surface of the copper block is a type K thermocouple embedded in a groove to measure the surface temperature as seen in figure 4.2.

The copper block is painted with black paint, Nextel Velvet-Coating 811-21, which has been well documented by Lohrengel and Todtenhaupt [11], and a datasheet for which can be found in appendix A.2. The coating and thinner are pictured in figure 4.3.

Moreover, the copper block contains a hole with a diameter of 3mm and a depth of 25mm, the interior of which is also coated in Nextel Velvet-Coating. According to VDI/VDE3511 [12], such a cavity with a depth five times its diameter and an internal coating with emissivity $\varepsilon = 0.5$, can be expected to have an emissivity of $\varepsilon = 0.99$. It is

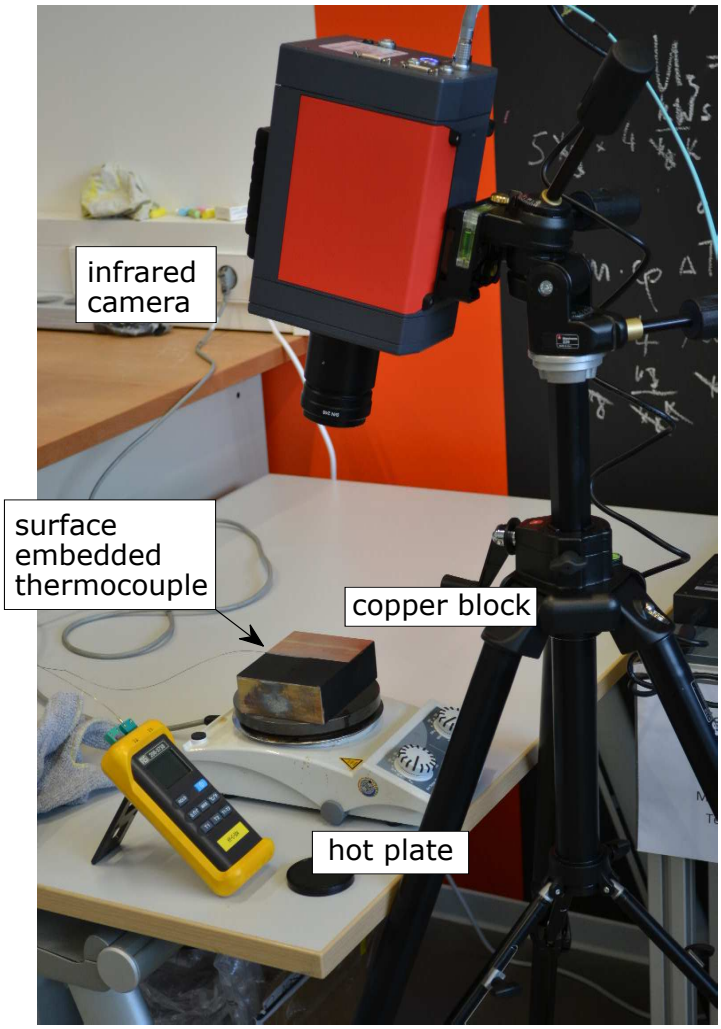

Figure 4.1: Experimental Setup for a precalibration

therefore reasonable to approximate this hole, with a depth to diameter ratio greater than 7 and with the inner surface coated with Nextel Velvet-Coating, which has an emissivity of approximately $\varepsilon = 0.97$ (see [11]), as a blackbody.

As discussed in section 3.4, the copper block can be considered to be an isothermal mass. This ensures that the temperature recorded by the thermocouple is homogeneous over the entire surface within the blackbody approximating cavity, which is necessary for an accurate precalibration.

To perform a precalibration, the copper block is heated to a range of temperatures, at each of which the infrared irradiance is measured by the infrared camera and the temper-

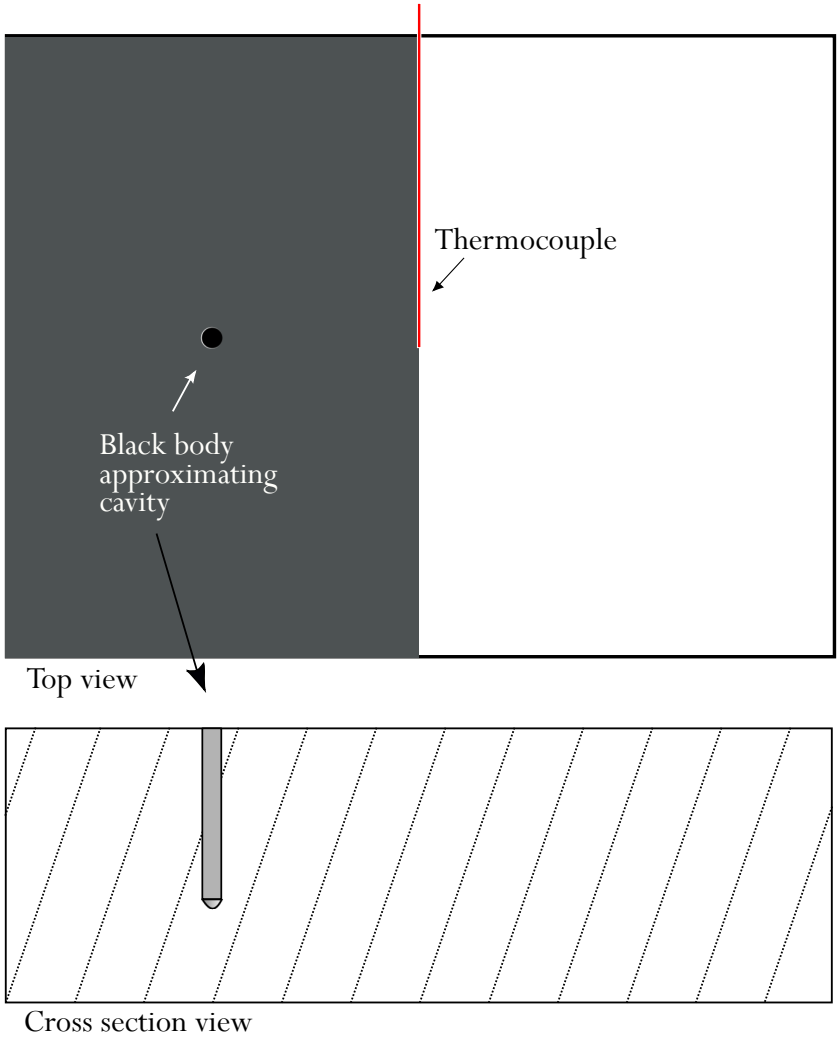

Figure 4.2: Copper block used for precalibration

ature is measured by the embedded thermocouple. A least squares fit of equation 2.5 is applied to the data to determine the parameters b, r, f, and I_{offset}. Figure 4.4 shows a plot of block temperatures relative to scaled irradiance as well as the resultant temperature curve fit.

The thermocouple embedded in the block is a class 1 Type K thermocouple, which is rated by the standard IEC 584-3 to have an uncertainty of ± 1.5 K and is used with a National Instruments CDAQ 9214 module rated with an uncertainty of ± 0.37 K. This gives the thermocouple a total uncerainty of approximately ± 1.9 K. The precalibration can

Figure 4.3: Nextel Velvet Coating with thinner

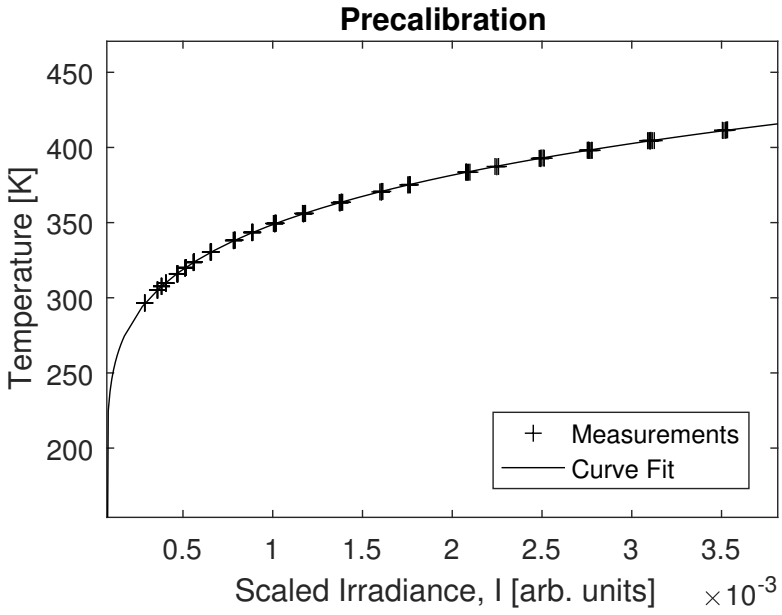

Figure 4.4: Resulting fit of a Precalibration

therefore be expected to provide temperatures with an uncertainty exceeding ± 1.9 K.

These parameters determined through precalibration could theoretically be used, in conjunction with a known emissivity, to determine surface temperatures from other infrared camera measurements, but such temperature measurements would suffer from inaccuracies caused by variation in the measurement suroundings, especially differences in the level of ambient thermal radiation. For this reason, the precalibrated parameters are used only as a starting point for in situ calibration, which is able to adjust the temperature curve for conditions at the time of measurement.

Precalibrations are performed in conditions that approximate the conditions of measurement as closely as possible. The measurements made in the course of this work are all done in open air, and so the precalibration is done as well. In the case of some measurements, however, it could be important to view the object of interest in an enclosure, through a sapphire window or another material that is highly transmissive in the spectral range of the camera. In such cases, it would be important to perform a precalibration specifically for that set up.

The blackbody approximating cavity, as described above is ideal for this precalibration method, but any isothermal surface with a known emmissivity can be used for such a precalibration. The relationship of emissivity with the precalibration parameters is discussed further in section 4.2.

4.2 Determination of emissivity for different coatings

The emissivity determination procedure is very similar to precalibration. Using the same setup described in section 4.1 and figure 4.1, temperature of the copper block is varied while measurements are taken with both the infrared camera and embedded thermocouple, in order to compare the irradiance measured from the black body approximating cavity and the surface of the block, covered with a coating of interest. With the emissivity of the cavity assumed to be $\varepsilon = 1$, the emissivity of the surface coating can be determined by

comparison.

Surfaces are considered to be gray bodies, meaning the emissivity is assumed to be constant for the wavelengths of infrared light that the camera records (2,7 μm - 5,0μm). Emissivity is also necessarily assumed to be constant across the temperature range tested.

Parameters, now including emissivity, ε, are found by means of a least squares fit to an altered form of equation 2.5, shown below as equation 4.1, simultaneously applied to the black body approximating cavity and the surface of interest.

$$T_{obj} = \frac{b}{ln(\frac{\varepsilon r}{I - I_{\text{offset},0} - (1-\varepsilon)\cdot I_{\text{offset,amb}}} + f)} \tag{4.1}$$

Incorporation of emissivity into equation 4.1 is facilitated by two changes in parameters from equation 2.5. Firstly, the parameter r is replaced with the product εr, due to the relationship between emissivity and the parameter r, as discussed in section 2.2. This does not alter the parameter r because in the case of precalibration using the blackbody approximating cavity, the emmissivity is assumed to be equal to one, in which case $\varepsilon r = r$. Second, I_{offset} is split into two components to account for the thermal radiation reflected off of the coated surface which does not reflect off of the blackbody approximating cavity:

$$I_{\text{offset}} = I_{\text{offset},0} + (1 - \varepsilon) \cdot I_{\text{offset,amb}}, \tag{4.2}$$

where $1 - \varepsilon$ represents the reflectivity, ρ, according to Kirchhoff's Law (see section 2.2).

Because the blackbody approximating cavity has an assumed emissivity of $\varepsilon = 1$, equation 4.1 takes a form nearly identical to the original equation 2.5:

$$T_{obj} = \frac{b}{ln(\frac{r}{I - I_{\text{offset},0}} + f)}. \tag{4.3}$$

With this procedure, the emissivity, ε, along with the parameters b, r, f, $I_{\text{offset},0}$, and $I_{\text{offset,amb}}$ can be determined. Alternatively, the parameters b, r, and f can be assumed to

be constant from a previous precalibration, such that only ε, $I_{\text{offset},0}$, and $I_{\text{offset,amb}}$ must be determined.

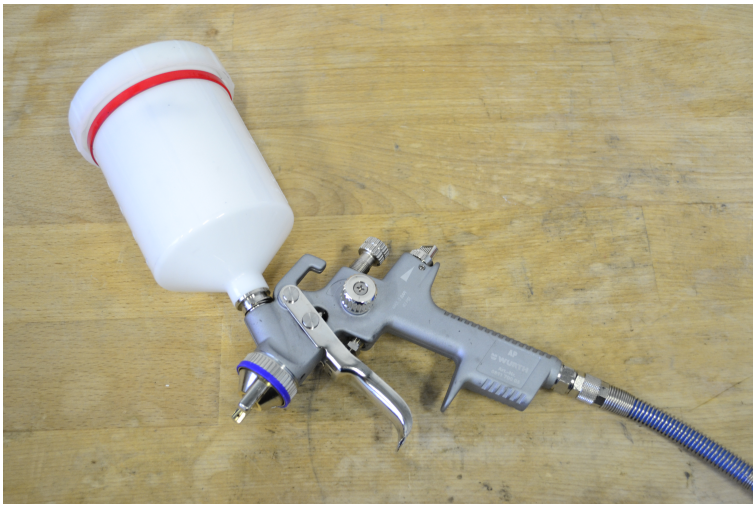

Figure 4.5: Paint Gun used for Nextel Velvet Coating application

The surface coating of greatest interest is the Nextel Velvet Coating 811-21, as its high emissivity yields better measurement results. This coating is applied using a paint gun such as the one pictured in figure 4.5. In some cases for a fast measurement a coating that can be applied more quickly and later easily removed is favorable. A chalk spray and a developer spray are available to the author for this purpose, and their emissivities are investigated according to the procedure described above. The chalk spray is pictured in figure 4.6 and a datasheet can be found (in German) in appendix A.3. The developer, Ardrox NQ1, is pictured in figure 4.7 with a datasheet in appendix A.4.

A thermogram of the copper block used for the determination of the emissivity of the three surface coatings is displayed in figure 4.8. This image was taken with an integration time of 200 μs while the copper block was heated to approximately 125 °C.

Figure 4.9 and table 4.1 present the results of the emissivity determination process. The emissivity values can then be used in later temperature measurements.

The procedure is validated by the fact that the measured emissivity of $\varepsilon = 0.972$ for the Nextel Velvet coating across the wavelength range from 2μm to 5.7μm corresponds closely

Figure 4.6: Chalk Spray

Table 4.1: Results from emissivity determination

Surface Coating	**Nextel Velvet Coating**	**Photo Developer**	**Chalk Spray**
Emissivity, ε	0.972	0.222	0.458

$I_{\text{offset,0}}$	$I_{\text{offset,amb}}$	b	r	f
9.65×10^{-12}	3.03×10^{-4}	2.48×10^{3}	1.17	81.86

to the emissivity measured by Lohrengel and Todtenhaupt [11], who found an emissivity of 0.975 for a wavelength of 4μm and 0.966 for a wavelength of 5μm.

Figure 4.7: Ardrox NQ1 Developer

4.3 Measurement with In Situ Calibration

A known surface emissivity and the parameters obtained from a precalibration are sufficient to approximate the temperature field over a surface in an infrared thermographic image, but as discussed in section 2.2, several factors in the surroundings of a measurement can alter the relationship between measured scaled irradiance and actual surface temperature, making it necessary to perform an in situ calibration to increase the accuracy of the final temperature measurement.

Figure 4.8: Thermogram of the copper block used for emissivity determination

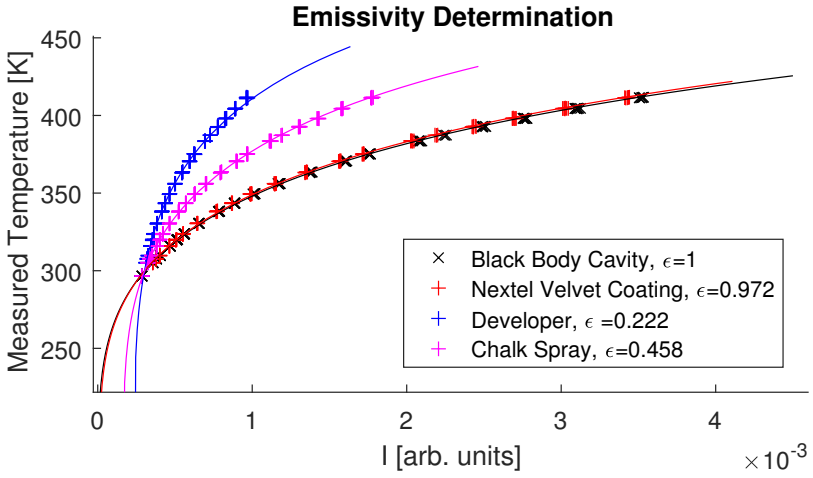

Figure 4.9: Temperature fit for emissivity determination

The in situ calibration is performed by measuring the temperature of a point within the surface of interest with a thermocouple simultaneously with infrared image capture. The parameter I_{offset} is adjusted to better fit the thermocouple measurement, providing a new set of parameters specific to the temperature fit of the current measurement. This is

accomplished with a least squares fit to the equation

$$T_{obj} = \frac{b}{ln(\frac{\varepsilon r}{I - I_{\text{offset}}} + f)}, \tag{4.4}$$

much like the precalibration. The initial value for I_{offset} as well as the parameters b, r, and f are taken from a previously performed precalibration and the emissivity, ε, is determined as described in section 4.2.

When only I_{offset} is adjusted, it is advantageous if the thermocouple is placed in a region of the surface expected to have a lower temperature. This is due to the form of the equation and the role of I_{offset} within it. The difference in calculated temperature caused by a shift in I_{offset} decreases as scaled irradiance increases. The in situ adjustment will have the greatest influence on temperature where there is a lower scaled irradiance (and therefore lower temperature), so it is advantageous to place the thermocouple in such a region, where temperature accuracy is most dependent on the fit.

In certain cases it may be possible to use more than a single thermocouple measurement to support the in situ fit. This could be accomplished if multiple thermocouples can be embedded in the surface or if measurements can be taken at different surface temperatures. In such cases, it may be advantageous to vary the other parameters in addition to I_{offset}. A particular instance where this might be especially useful is if a surface of unknown emissivity is being measured, the parameter r could be adjusted to account for emissivity. It is of course preferable to more rigorously determine emissivity beforehand, but in cases where that is impractical, or where the emissivity of the surface coating in question varies significantly with application, this provides a good possibility.

CHAPTER 5
EXPERIMENTAL APPLICATION OF THE TEMPERATURE MEASUREMENT WORKFLOW

The techniques and process laid out/discussed in the previous chapters is meant to describe a procedure for surface temperature measurement of flat surfaces using infrared thermography. This procedure is meant to be widely applicable for use in a variety of potential situations, and can be applied as the need arises for a surface temperature measurement. In this chapter, the procedure is applied in a temperature measurement in order to validate it and illustrate its use.

5.1 Experimental Setup

The measurements taken in this chapter use a 100mm$\times$150mm$\times$3mm aluminum plate with a temperature gradient across it. A 46mm$\times$150mm portion of the plate is coated in Nextel Velvet-Coating and serves as the surface of interest for the temperature measurements. The plate is represented in figure 5.1. Four type K 0.25mm thermocouples are embedded in the surface beneath the coating for the in situ calibration and temperature field evaluation. The thermocouples, referred to as TC_1, TC_2, TC_3, and TC_4, and which measure the temperatures T_1, T_2, T_3, and T_4 respectively, had each been calibrated relative to a PT100 resistance temperature detector with a linear fit based upon two points, one at room temperature and one at approximately 90°C. The PT100 detector is rated according to the standard IEC 751 to have an uncertainty of $\pm$0.5 K at 150°C measured with a National Instruments CDAQ 9216 module rated with a $\pm$0.15 K uncertainty, making a total uncertainty of $\pm$0.65 K. The uncertainty of the calibrated thermocouples is assumed to be in the same range.

A temperature gradient is created across the plate by cooling one side of the plate and heating the other. This is done by resting each side of the aluminum plate on a copper

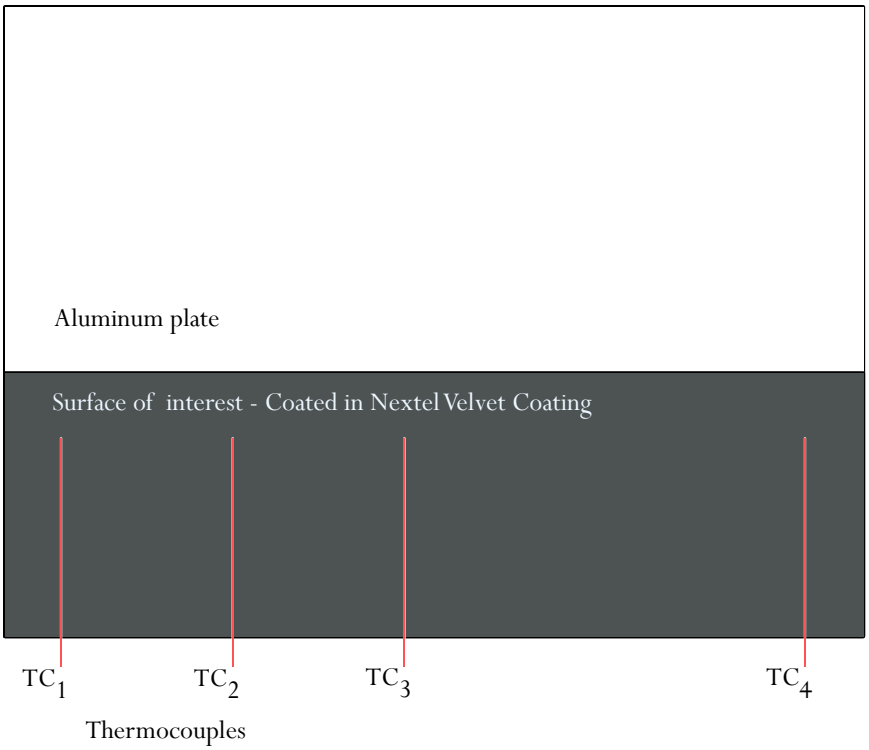

Figure 5.1: Aluminum plate used for measurements

block, with weights on the aluminum plate but away from the surface of interest to improve thermal contact. One of the copper blocks, used for cooling, has channels drilled through it, through which water passes. The water temperature is controlled by a thermostat to a steady temperature of 10.5°C. The copper block on which the other side of the aluminum plate rests is heated by a hot plate to a range of temperatures. Measurements are made at eight different temperature configurations, four with TC_1 on the hotter end and TC_4 on the colder end, and four with TC_1 on the colder end and TC_4 on the hotter end. It is relevant which thermocouple is at a higher temperature because TC_2 and TC_3 are not evenly spaced between TC_1 and TC_4. For each temperature configuration, the temperature field is left to reach steady state before measurements are taken.

The resulting temperatures reached on either side of the plate as indicated by thermocouples TC_1 and TC_4 are shown in table 5.1.

In most of the included cases the difference in temperature across the plate requires images to be captured at multiple integration times which are then combined into one high

Table 5.1: Temperatures measured

T_1 [°C]	T_4 [°C]
33.6	88.9
38.7	108.9
45.5	134.2
50.8	154.0
87.1	27.1
106.5	31.2
132.2	36.3
141.6	38.2

dynamic range image. In all cases images are taken at three integration times.

The procedures desribed in chapter 3 are applied to each of the thermographic images captured: Detector signal values higher than 80% or less than 20% of the maximum possible value are removed, the detector signal values are then normalized, are transformed into scaled irradiance through the application of the coefficients from a previously performed pixelwise radiometric self calibration, and finally a NUC is applied.

The scaled irradiance value for each pixel in the final high dynamic range image comes from only one of the three source images, with the image with the highest integration time that includes a value for that pixel being selected.

In the determination of temperature from the scaled irradiance, the procedure outlined in section 4.3 is followed to perform an in situ calibration. The value used for the emissivity of the surface of interest is $\varepsilon = 0.972$, the value determined as outlined in section 4.2. The parameter values from section 4.1 are also used.

For the in situ calibration, various techniques, including variation of multiple parameters and the use of multiple thermocouples are used for the purpose of comparison.

The main method for in situ calibration requires one thermocouple in the surface of interest and adjusts only the parameter I_{offset}. This approach is deemed to be the most practical, as it will often be difficult to attach multiple thermocouples to surfaces of interest. It is also expected to be sufficient in most cases because I_{offset} is expected to capture any effects of the thermal radiation of the surroundings.

The technique with the use of one thermocouple and the adjustment of only I_{offset} is therefore the focus, but other options are examined as well for cases where they might also be useful.

5.2 Results

In the following sections the results of the temperature measurements are shown and discussed. Section 5.2.1 presents an in situ calibration adjusting the single parameter I_{offset} using one of the four thermocouples for calibration. Section 5.2.2 presents an in situ calibration adjusting the two parameters I_{offset} and r using two of the four thermocouples for calibration.

5.2.1 In situ fit of a single parameter, I_{offset}

The following paragraphs discuss the results of the measurements analyzed using one thermocouple to adjust only the parameter I_{offset} to determine temperature.

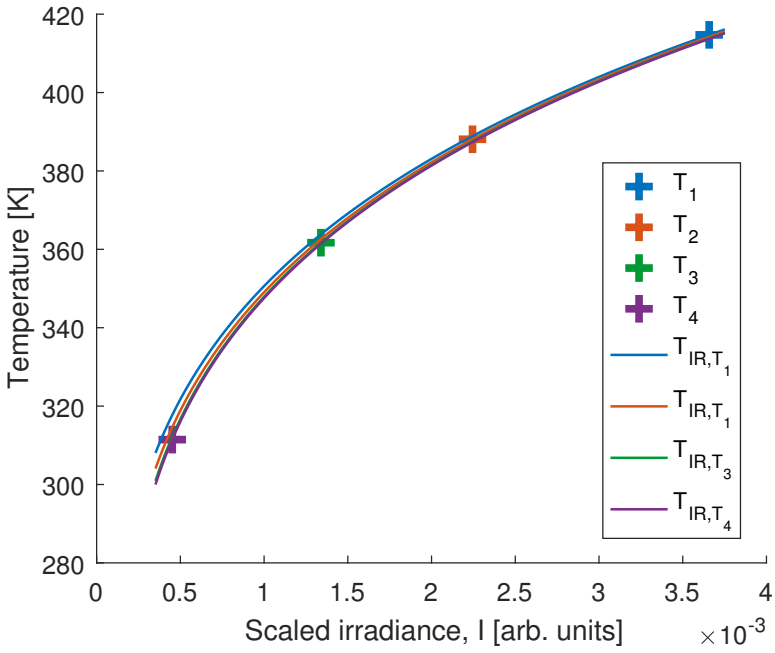

Figure 5.2: Resulting in situ fits based on each of the four thermocouples

Figure 5.2 shows four different in situ fits that could be applied to the measurement taken with T_1 at 142 °C and T_4 at 38 °C. Each of the in situ fits displayed are made by adjusting only I_{offset}, and each is based off of the temperature measured by a single one of the thermocouples, TC_1, TC_2, TC_3, and TC_4. Let T_{IR,TC_1} be the temperature curve defined by the in situ fit based on TC_1, etc.

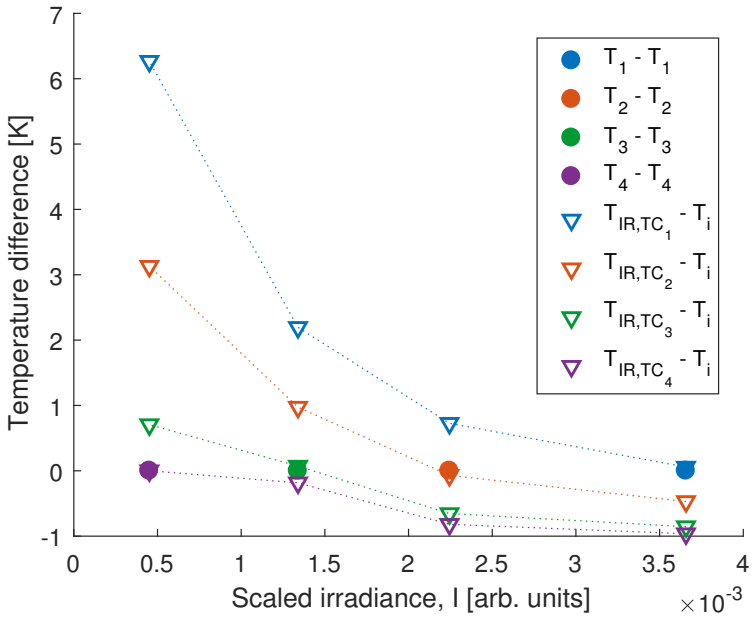

Figure 5.3: Magnitude of temperature difference between the thermocouple measurements and the in situ fits of I_{offset} based on each of the thermocouples TC_1 through TC_4

As stated in section 4.3, the fit based on the thermocouple placed in the coldest region (in this case TC_4) is expected to be the most accurate. The fits are compared by evaluating the difference between the temperature as determined by the fit and as measured by each of the thermocouples at each of the four thermocouple locations. Figure 5.3 visualizes the magnitude of temperature error due to the in situ calibration of I_{offset} with each of the four thermocouples by plotting the temperature difference between the in situ fit and the thermocouples. The trend is clearly displayed in the figures: the lower the temperature that the in situ fit is based on, the smaller the deviation between in situ fit and thermocouple values. This is corraborated by the other seven experimental runs and is to be expected simply

because of the form of the calibration curve. At lower temperatures, a change in scaled irradiance corresponds to a larger temperature difference than the same change would at a higher temperature. It is therefore recommended to base in situ calibrations on temperature sensors placed in the portion of the surface expected to have a lower temperature. Subsequently, only the calibration curve based on the coldest thermocouple measurement will be discussed for measurements using this set up for the in situ technique.

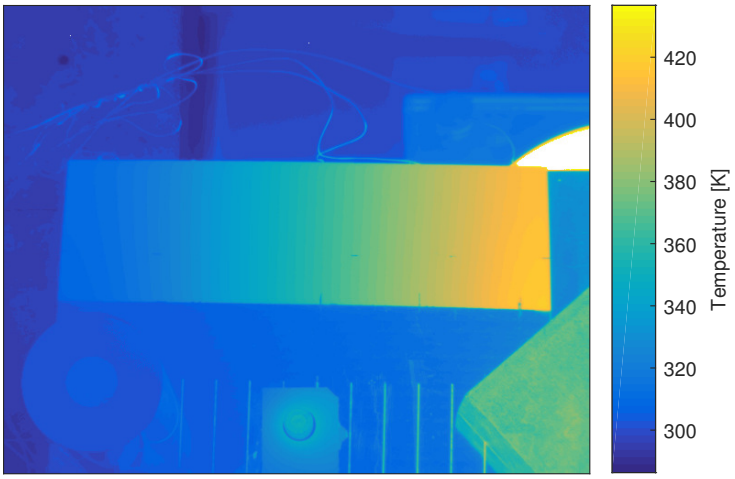

Figure 5.4: Temperature result using in situ adjustment of I_{offset} based on T_4

Figure 5.4 shows the thermographic image taken from the measurement of the case where T_4 measures 38 °C and T_1 measures 142 °C, with the equation for temperature with the parameter I_{offset} adjusted to fit the measurement at T_4 applied, resulting in temperature. Figure 5.5 displays the same temperature field with image plane rectification and figure 5.6 is cropped to display only the calculated temperature of the surface of interest.

The temperature curve determined by in situ calibration of the parameter I_{offset} is compared to the temperature curve defined by the precalibrated parameters in figure 5.7.

Each of the infrared measurements were taken with a high dynamic range at three different integration times. The value of each pixel comes from the image with the highest integration time that still had a value within the linear range for that pixel. Figure 5.8 shows

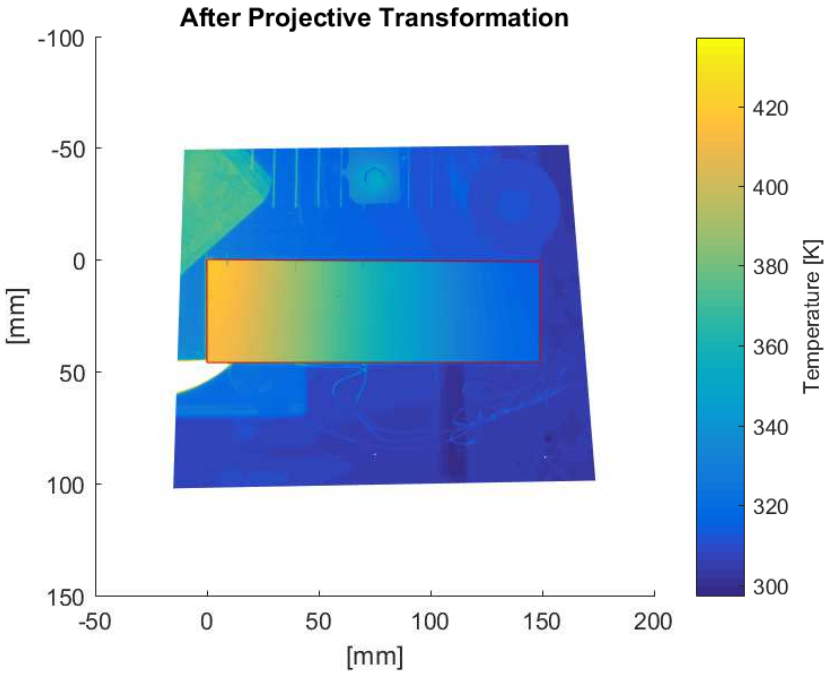

Figure 5.5: Plane projection transformed temperature result using in situ adjustment of I_{offset} based on T_4

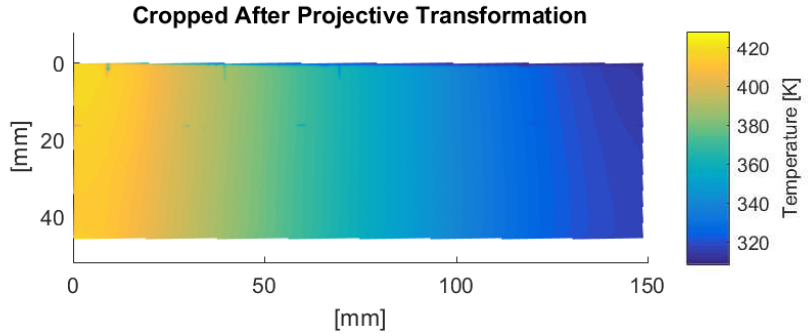

Figure 5.6: Plane projection transformed temperature result using in situ adjustment of I_{offset} based on T_4

which integration time each pixel was taken with for the measurement shown in figure 5.6.

With only one of the four available thermocouples being used for the in situ calibration, the remaining three thermocouples are used to evaluate the temperature curve determined by the fit. The thermocouple measurements taken at the same time as the thermographic measurement corresponding to the pixels in the region of a given thermocouple are used for this purpose (the time beween measurements at different integration times used for the HDR

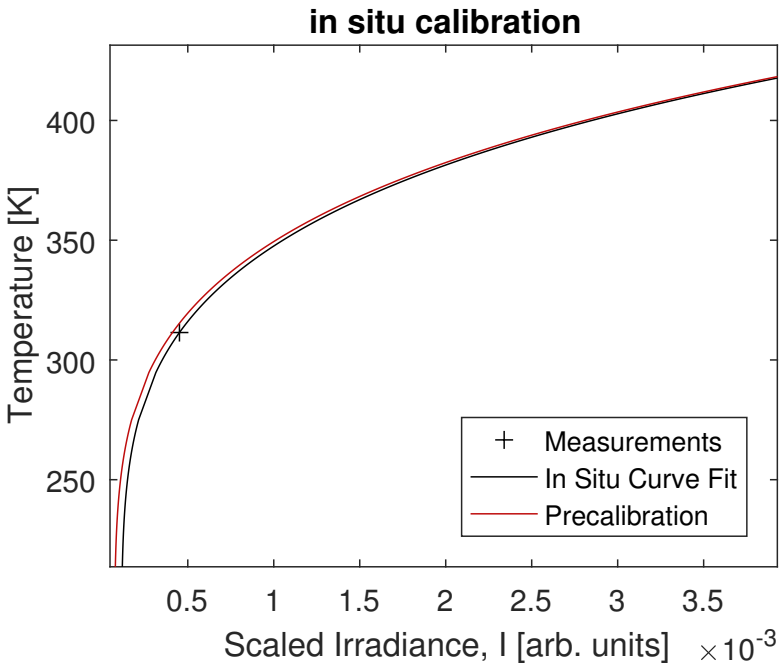

Figure 5.7: Precalibration and in situ with I_{offset} adjustment temperature curves

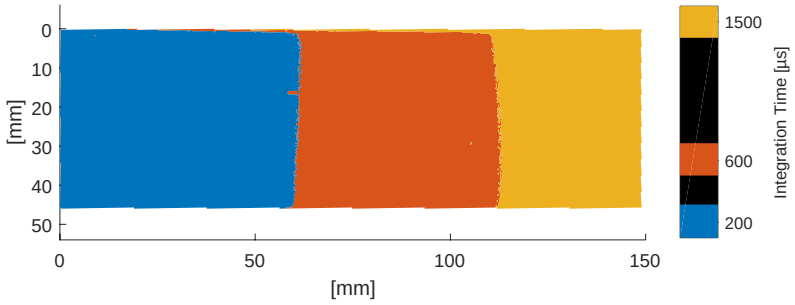

Figure 5.8: Integration times used for in situ adjustment of I_{offset} based on T_4

image makes this necessary). Figure 5.9 shows the difference in temperature measured by the unused thermocouples and the temperature curve determined by the thermocouple at the coldest location for each of the eight measurements, relative to the temperature difference between the given thermocouple and the thermocouple used for the fit.

The error seems to generally increase with an increasing temperature difference between thermocouples, but the specifics of the trend are unclear. The maximum error temperature difference recorded was 1.93 K which occured with a 103 K difference between T_1, which was at approximately 50°C and T_4 at approximately 150°C. The second highest

was 1.02 K, also with a 103 K difference between T_1 and T_4. All other temperature error differences were below 1 K.

It is recommended that measurements made using this method be treated with a ± 2 K uncertainty. Recall that the estimated uncertainty of the calibrated thermocouples used for in situ calibration is ± 0.65 K (see section 5.1).

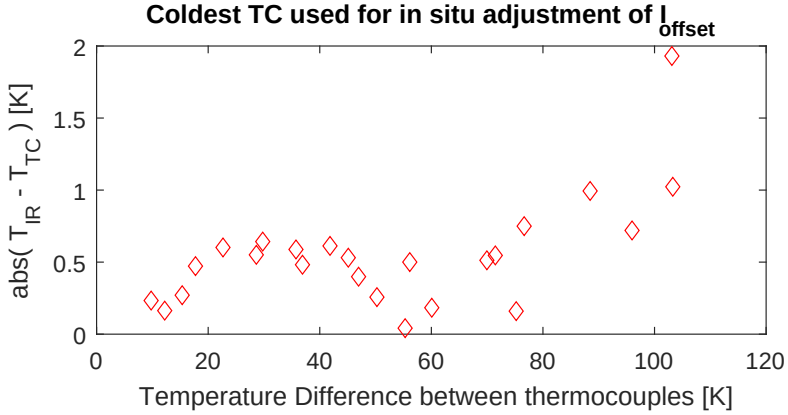

Figure 5.9: Temperature error for measurements fitting I_{offset} only with single thermocouple in lower temperature region

In reality the temperature of the surface of interest is not perfectly steady state, and with the time between measurements at different integration times, an actual, albeit slight, temperature difference is detected. In order to better understand the magnitude of the uncertainty due to these slight temperature variations with time, figure 5.10 additionally shows the maximum temperature difference for each pixel between images taken at different integration times. This was done by applying the semi empirical temperature function complete with in situ adjusted I_{offset}, as described above, to all usable pixels of each of the images, including pixels not used in the final HDR image. It is the difference between these calculated temperatures for each pixel between images taken with different integration times displayed in figure 5.10. Pixels that were available from only one image are represented with a zero value in the figure. The maximum calculated temperature difference between measurements at different integration times for any of the pixels of interest is 1.2 K, with the majority of pixels showing a difference well below 1 K. A distribution of non-zero

temperature differences is shown in figure 5.11.

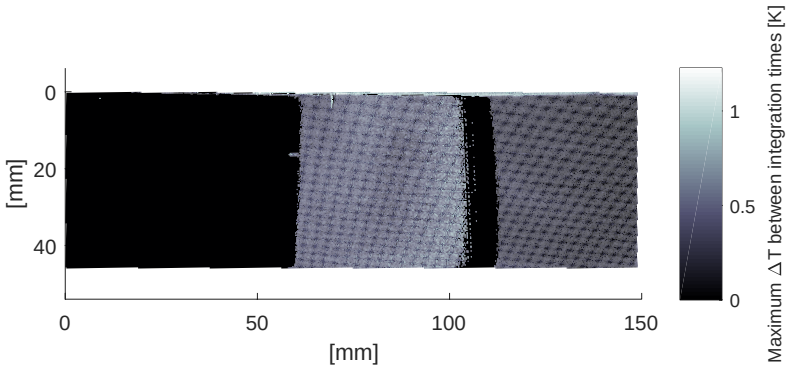

Figure 5.10: Difference in calculated temperature between measurements at different integration times

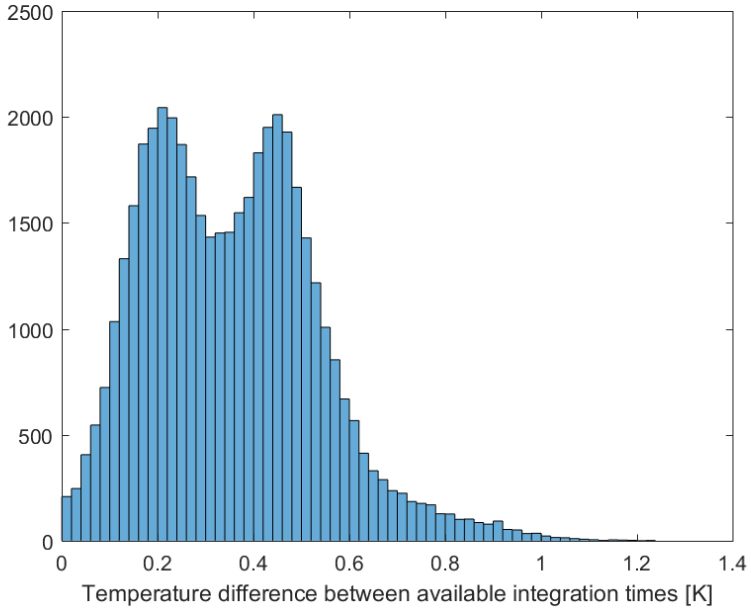

Figure 5.11: Distribution of temperature differences from figure 5.10

In addition to an actual difference in temperature with time, the uncertainty shown in these figures could derive in part from random variation in detector signal and uncertainty in the polynomials from pixelwise radiometric self calibration applied to the detector signal at various integration times. These uncertainties are independent of any uncertainty from the in situ determination of the temperature relation.

The uncertainties discussed here and displayed in figures 5.10 and 5.11 do not contribute further to the error measured and shown in figure 5.9 or the recommendation to treat measurements with an uncertainty of 2K, but give additional insight into some sources of uncertainty and underscore the importance of measuring under steady state conditions when using HDR.

5.2.2 In situ fit of two parameters, I_{offset} and r

The thermocouples in the regions of highest and lowest temperature are used for the adjustment of the parameters I_{offset} and r.

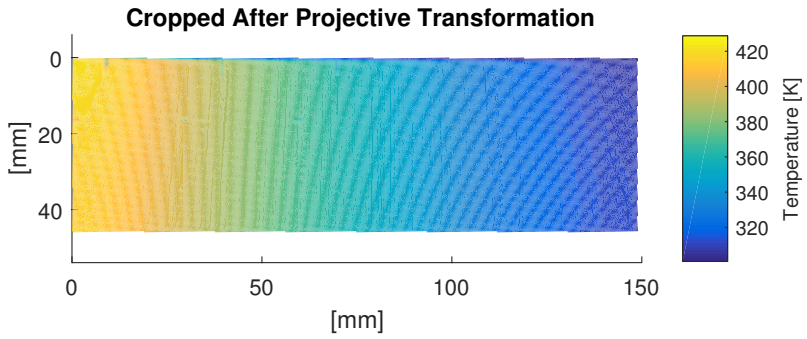

Figure 5.12: Plane projection transformed temperature result using in situ adjustment of I_{offset} and r based on T_1 and T_4

Figure 5.12 displays the temperature field for the surface of interest calculated by in situ fit of I_{offset} and r to the thermocouple measurements T_1 and T_4 for the same measurement as above in section 5.2.1 with the temperatures $T_1 = 142°\text{C}$ and $T_4 = 38°\text{C}$.

The temperature relationship to scaled irradiance determined by the in situ adjustment of the parameters I_{offset} and r based on the temperatures T_1 and T_4 for the same experimental run is plotted in figure 5.13. In this instance, the differences between the temperature measured by the thermocouples and calculated with the in situ fit for the thermocouplces not used for calibration are $T_{2,IR} - T_{2,TC} = 0.12$ K and $T_{3,IR} - T_{3,TC} = 0.41$ K.

The temperature curve determined by in situ calibration of the parameters I_{offset} and r is compared to the temperature curve defined by the precalibrated parameters in figure 5.14.

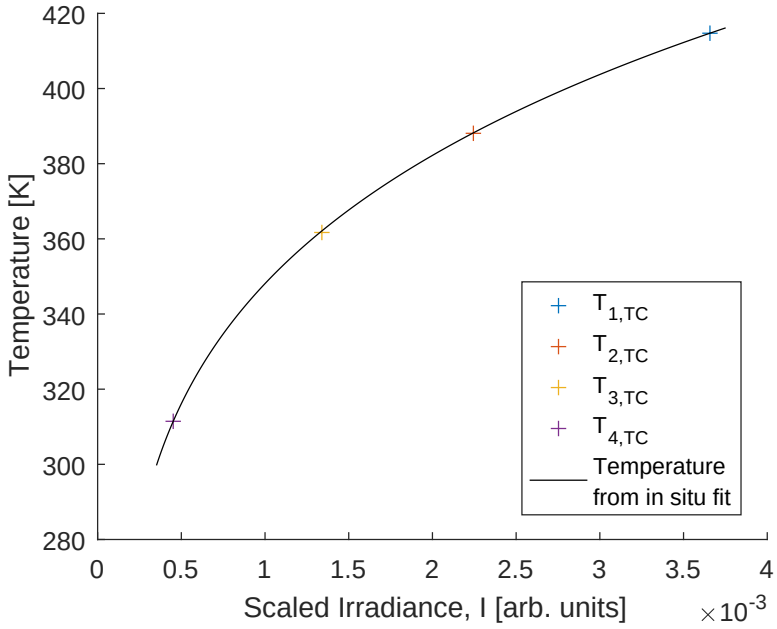

Figure 5.13: Resulting in situ fit based on T_1 and T_4

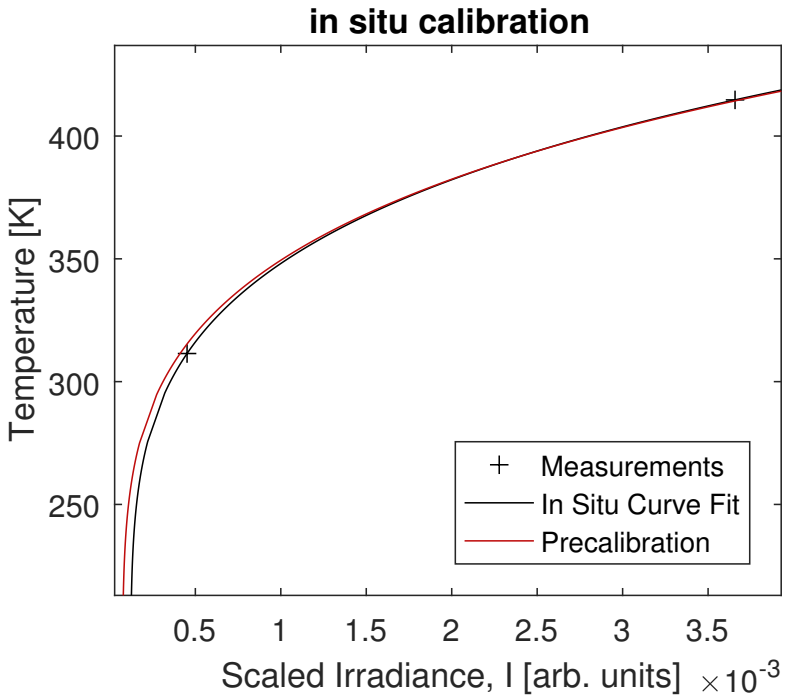

Figure 5.14: Precalibration and in situ with I_{offset} adjustment temperature curves

The temperature error for all eight of the experimental runs is plotted relative to the minimum temperature difference between the thermocouple used for the measurement and

the thermocouples used in the in situ calibration in figure 5.15. The temperature error is once again quantified as the magnitude of the difference between the temperature measured by the thermocouple not used in the in situ calibration and the temperature calculated by the in situ fit at the corresponding scaled irradiance. It can be noted that there are 16 points available as opposed to the 24 available for the in situ fit of only I_{offset}, due to the use of an additional thermocouple for the in situ calibration.

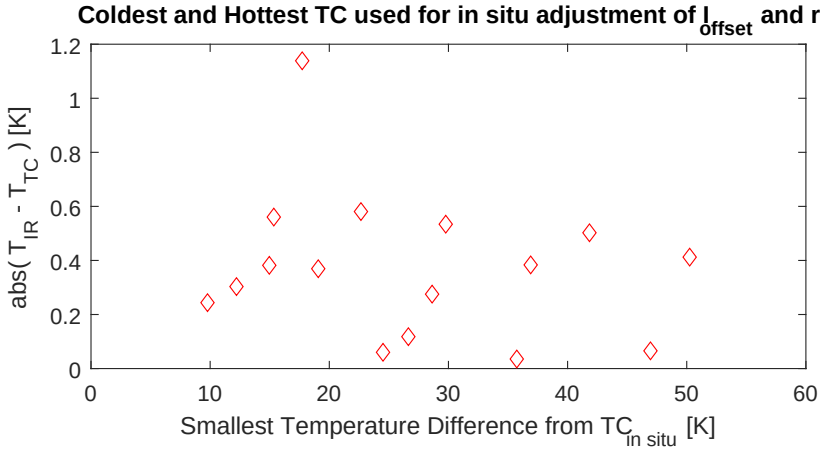

Figure 5.15: Temperature error for measurements of T_2 and T_3 fitting I_{offset} and r using T_1 and T_4

The maximum error temperature difference recorded was 1.14 K. This occured with a temperature difference of 18.7 K between T_2, which was the source of the error and T_1, which was used for the in situ calibration. This measurement was from the same experimental run as the maximum error in section 5.2.1 which had a 103 K difference between T_1, which was at 51°C and T_4 at 154°C. All other temperature error differences were below 0.6 K.

It is recommended that measurements made using this method be treated with a $\pm$1.2 K uncertainty. This demonstrates an improvement over the method using one thermocouple to fit only the parameter I_{offset}. The reason for this is probably that the emissivity of the surface of interest deviated slightly from that of the surface used for emissivity determination. Such deviation is taken into account by the additional in situ fitting of the parameter r. The uncertainty was also likely improved simply by the use of two thermocouples covering

the range of temperatures rather than one and a smaller temperature difference between thermocouples used for in situ calibration and those used for error determination.

CHAPTER 6
CONCLUDING SUMMARY

A workflow for the measurement of surface temperature by means of infrared thermography has been designed and implemented.

Procedures for acquiring scaled irradiance from camera detector signal using pixelwise radiometric self calibration and nonuniformity correction have been described and implemented using matlab scripts. A plane projective transformation procedure has also been outlined and implemented with a matlab script in order to transform the temperature data from pixel locations in a thermographic image to physical locations on the object plane.

A procedure for the precalibration of the parameters a semi empirical equation based on Planck's law of radiation has been outlined and implemented using a matlab script. A procedure for the determination of emissivities of surfaces has been designed and implemented using a matlab script. A procedure for the in situ calibration of infrared thermal measurements has been outlined and implemented.

Experimental measurements have been carried out for validation of the technique using both in situ adjustment of a single parameter, I_{offset}, and with the two parameters, I_{offset} and r. For the single parameter case, a measurement uncertainty of 2 K has been found, and for the case of two parameter adjustment, a measurement uncertainty of 1.2 K has been found.

Potential future improvements on the work done include the incorporation of matlab scripts into a user interface to allow measurement without manipulation of a script, the incorporation of the procedures with direct connection to the camera to allow for real time or near real time temperature measurement, and the incorporation of protocol to map temperatures to geometries of greater complexity than a flat surface and to correct image distortions of a more complicated nature, such as radial distortions.

PART 2

THERMODYNAMIC AND ECONOMIC ANALYSIS OF THE INCORPORATION OF THE SUPERCRITICAL CARBON DIOXIDE BRAYTON CYCLE INTO COMBINED CYCLE POWER PLANTS

CHAPTER 7
INTRODUCTION AND BACKGROUND

7.1 Combined Cycle Power Plants

Power plants are important for the supply of electricity to everything we do as humans. We are consistently looking for more efficient methods of power generation for both economic and environmental reasons.

Natural gas power plants are a well established source of electricity. Natural gas turbines, whose early development was largely for military aircraft propulsion, have been in use for robust, land-based power since the 1940s. [13] The U.S. Energy Information Administration (EIA) reports that in 2019 approximately 1582 TWh of energy was produced in the U.S. using natural gas at utility scale facilities, which makes up 38% of the total 4118 TWh of energy produced. [14] This makes natural gas the most common source of energy generation in the U.S. Natural gas power plants typically use a Brayton power cycle, wherein air is taken in, pressurized, and with the addition of natural gas is combusted. The resulting heat energy is harvested as electrical energy with the use of a turbine and generator. The entire process is generally incorporated into a single unit, with the compressor proceeding the combustion chamber which is followed directly by the turbine.

Natural gas power plants have typical thermal efficiencies in the 30% to 40% range. The majority of the remaining 60% to 70% of energy is lost as waste heat. This flow of energy is represented visually in figure 7.1. With such high energy losses in the exhaust gas, methods to convert the waste heat into useful energy are clearly beneficial. Waste Heat Recovery (WHR) increases the thermal efficiency and the potential for improved cost efficiency.

Combined cycle power plants (CCPPs) combine a natural gas cycle with a WHR cycle

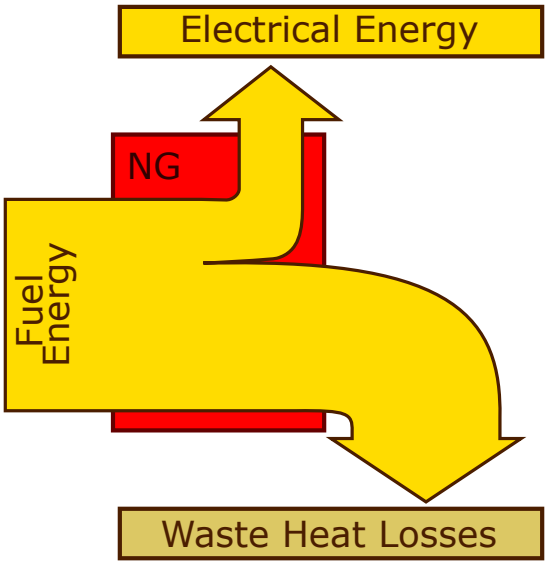

Figure 7.1: Energy flow for a standalone natural gas cycle. [15]

(also known as a bottoming cycle), which converts the waste heat into electrical energy. The flow of energy in a CCPP is represented in figure 7.2. Traditional CCPPs use a steam Rankine bottoming cycle and are the standard method for WHR for a natural gas power plant. The technology is very well established. The EIA reports that in 2019 1330 TWh of energy was generated by natural gas combined cycle power plants in the United States, which makes up 84 % of the energy generated from natural gas. [16]

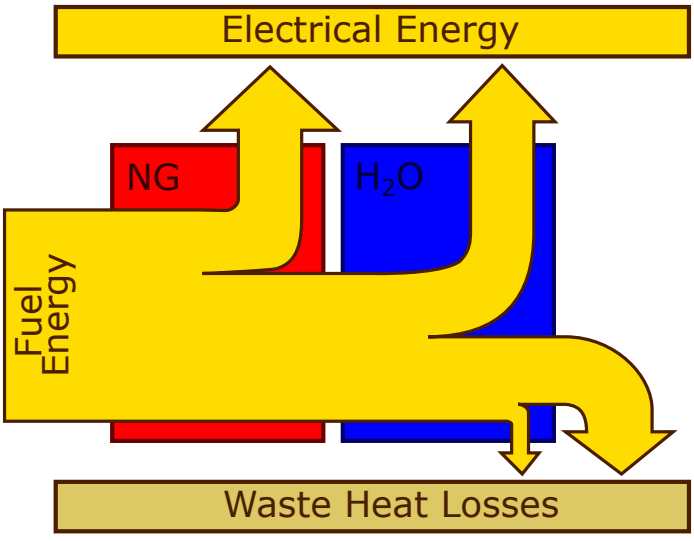

Figure 7.2: Energy flow for a traditional combined cycle power plant. [15]

In a traditional CCPP, the exhaust gas from the natural gas turbine is led through a heat recovery steam generator (HRSG) and serves as the energy source for the steam Rankine cycle. The HRSG includes a series of heat exchangers through which the exhaust gases transfer heat to the water: the economizer, the evaporator and the super heater. Pressurized water enters the HRSG where it is warmed to the saturation temperature by the economizer, undergoes a state change into water vapor in the evaporator, and is heated further in the super heater. The super-heated steam is channeled through a turbine which converts the heat energy into mechanical energy which is converted by a generator into electrical output.

CCPP readily reach efficiencies approaching 60%. [15] In recent years, some CCPP have exceeded 60% net efficiency and there is talk in the industry of reaching 65% efficiency in the next ten years, though that is a very optimistic estimate. [17] [18]

The increased fuel efficiency makes combined cycle power plants environmentally friendlier than standalone natural gas power plants, which in turn are more environmentally friendly than other fossil fuel power production methods, but combined cycle power plants still release CO_2 and other pollutants into the environment. Carbon capture technology has been implemented in many HRSGs to reduce the carbon footprint of power plants, but also comes with a high price tag. Any gains in thermal efficiency also lead to lower fuel consumption and emissions for the same energy output.

7.2 sCO_2 Power Cycles

Supercritical carbon dioxide (sCO_2) Brayton power cycles, which take place entirely in a supercritical state with compression near the critical point, provide numerous benefits for power production and have been the subject of great interest and much research in recent years. These cycles take advantage of the changing thermodynamic properties of the fluid near its critical point. In this region the fluid can be efficiently compressed with relatively little work input required, which allows for a higher net work output and therefore thermal efficiency. The expansion of the fluid in a supercritical state avoids some of the

complications of turbine blade erosion that occur with expansion in the two phase region. The high pressures and thermal properties of CO_2 near the critical point allow for relatively large quantities of energy to be transferred through the fluid with a relatively low volumetric flow. This allows for a much smaller footprint compared to that required for other working fluids, saving space and potentially construction and maintenance costs.

Feher and Angelino independently proposed (sCO_2) power cycles in 1968. Angelino refers to his proposed cycles as condensation cycles, in which the heat rejection take place in the two phase region, but with the fluid in a supercritical state for the majority of the cycle. [19] Feher's cycle occurs entirely at supercritical pressures and he refers to it as the supercritical cycle. Feher presents CO_2 as one of several pure substances fit for his cycle. [20]

Interest in the cycles was minimal in the subsequent decades until it was reinvigorated in the early 2000s, with the doctoral thesis of Vaclav Dostal playing a notable role. Dostal thoroughly investigated the potential of sCO_2 power cycles for use in Gen IV nuclear power plants with promising results. [21] In the intervening years many researchers have presented their findings on the potential of sCO_2 power cycles for a multitude of power applications.

Informative reviews of sCO_2 power cycles have also been published. The book, *Fundamentals and Applications of Supercritical Carbon Dioxide Based Power Cycles* [22], provides an introduction to various topics relevant in sCO_2 power cycle research and applications. Ahn et. al.'s 2015 review [23] provides an overview of the technology and research. The 2017 review by Crespi et al. [24] gives a thorough summary of the cycle configurations that have been investigated in which applications.

The efficacy of sCO_2 power cycles in conjunction with natural gas power plants is among the applications that have been investigated and with promising results. Cho et al., for example, examine potential sCO_2 bottoming cycles for a large scale natural gas turbine (288 MW). Two of the seven cycle configurations examined provide higher efficiencies than the reference traditional combined cycle power plant. [25] From a practical economic

standpoint for the immediate future, the most promising sCO_2 bottoming cycles are for smaller scale natural gas power plants for which the incorporation of a steam Rankine cycle in a traditional combined cycle power plant would be impractical. [26] Incorporation at a larger scale also shows potential to improve upon combined cycle power plants, but these have the disadvantage of competing with the well established steam Rankine bottoming cycles.

7.3 Power Plant Profitability

Prediction of profitability is vital to the decision-making process in power plant development. Countless factors influence financial outcomes and metrics have been developed to estimate costs and returns and to allow financial comparison of of potential power plant types and layouts. One such metric is the levelized cost of electricity (LCOE) [27], which can be broadly defined as

$$\text{LCOE} = \frac{\text{sum of costs over plant lifetime}}{\text{total electrical energy production over plant lifetime}}. \tag{7.1}$$

Profitability can be determined by the difference of the sale price of electricity and LCOE. In this manner the LCOE provides a convenient value for comparison between the profitability of energy generation alternatives.

Wright and Scammell provide the following simplified formula for LCOE:

$$\text{LCOE} = \frac{\text{Cost}_{\text{project}} - \text{tax shield}_{\text{depreciation,PV}} + \text{Cost}_{\text{lifetime operation,PV}} - \text{Cost}_{\text{salvage,PV}}}{\text{lifetime electrical energy production}}, \tag{7.2}$$

where PV refers to the present value of expenses distributed across the lifetime of the power plant. $\text{Cost}_{\text{project}}$ refers to the initial capital cost to bring the power plant into operation. Depreciation Tax Shield can be estimated as the product of the project cost and an assumed tax rate. Lifetime operating costs include expenses across the lifetime of the plant

such as fuel and maintenance costs. Salvage costs are the expected value of the plant at the end of its lifetime. Lifetime electricity production is determined with the design power output of the plant multiplied by the expected plant lifetime and an estimated plant utilization factor. [26]

The actual project costs of completed power plants currently in operation can inform the estimation of natural gas and steam Rankine cycle project costs. Project Cost estimation for sCO_2 Brayton cycle power plants is more speculative, as the technology is still in development.

The 2014-15 Gas Turbine World Handbook reports the net plant output, steam turbine output and budget plant price of several combined cycle power plants. [28] Many variables influence the cost, but a general trend can be recognized relative to plant net power output, as shown in figure 7.3.

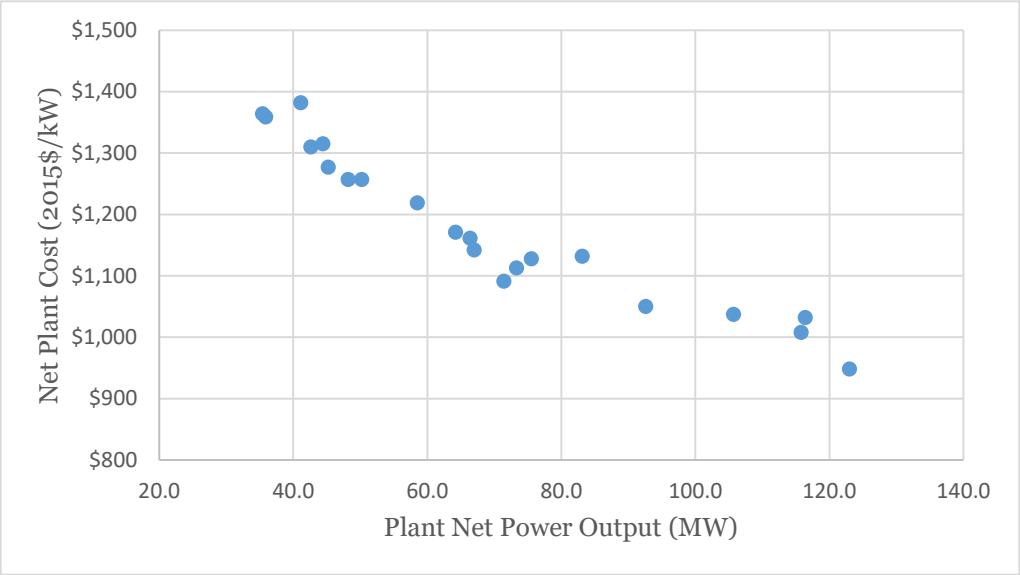

Figure 7.3: CCPP project cost as a function of net plant power output. [28]

Kehlhofer et al. [15] demonstrate in an example that in a traditional CCPP, the gas turbine, with its associated auxiliary systems and civil work, constitutes approximately half of the total plant capital cost while providing two thirds of the power output. This results in the electrical energy produced by the steam turbine costing approximately double

Table 7.1: Estimated cost of sCO_2 components. [29]

Component	specific cost
Recuperators	$2500\ [\frac{\$}{\mathrm{kW}_{th}/\mathrm{K}}]$
Primary WHR Heat Exchanger	$5000\ [\frac{\$}{\mathrm{kW}_{th}/\mathrm{K}}]$
Chiller	$1700\ [\frac{\$}{\mathrm{kW}_{th}/\mathrm{K}}]$
Other Components	$1000\ [\frac{\$}{\mathrm{kW}_{e}}]$

that produced by the natural gas turbine.

The method provided by Wright et al. estimates sCO_2 Brayton cycle cost on a component basis. The heat exchangers, as the costliest portion of the cycles, are considered most closely. Heat exchanger cost is assumed to be proportional to the heat energy transferred divided by the log mean temperature difference. A cost is estimated in $^{\$}/_{\frac{\mathrm{kW}}{\mathrm{K}}}$, which can then be scaled for heat exchangers with given heat transfer rates and design temperature difference.

For a plant in the 10 MW_e power range Wright et al. estimate the costs displayed in table 7.1, with an estimated uncertainty of $\pm 30\%$.

7.4 Project Objectives

The objective of this project is to analyze several configurations of possible combined cycle power plants with an integrated sCO_2 Brayton power cycle in order to determine the most profitable of those layouts and compare their profitability to combined cycle power plants currently in operation. The layouts to be investigated are outlined in section 7.4.1 and background on profitability determination is provided in section 7.4.2

7.4.1 Layouts

Five different sCO_2 Brayton cycle layouts will be examined in this work. Each of the five sCO_2 configurations will be investigated as part of three plant layouts: one with the sCO_2 Brayton cycle replacing the steam Rankine cycle as the sole bottoming cycle, and two in which both the sCO_2 Brayton cycle and the steam Rankine cycle are used as bot-

toming cycles, one with the sCO_2 cycle following the steam cycle, and another with the order reversed. These plant layouts are represented with their energy flow diagrams in figures 7.4, 7.5, and 7.6.

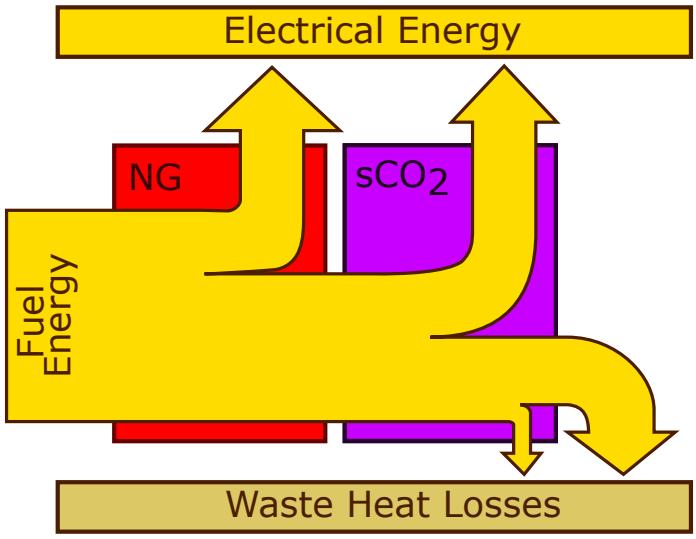

Figure 7.4: Energy flow for a CCPP with sCO_2 bottoming cycle. [22]

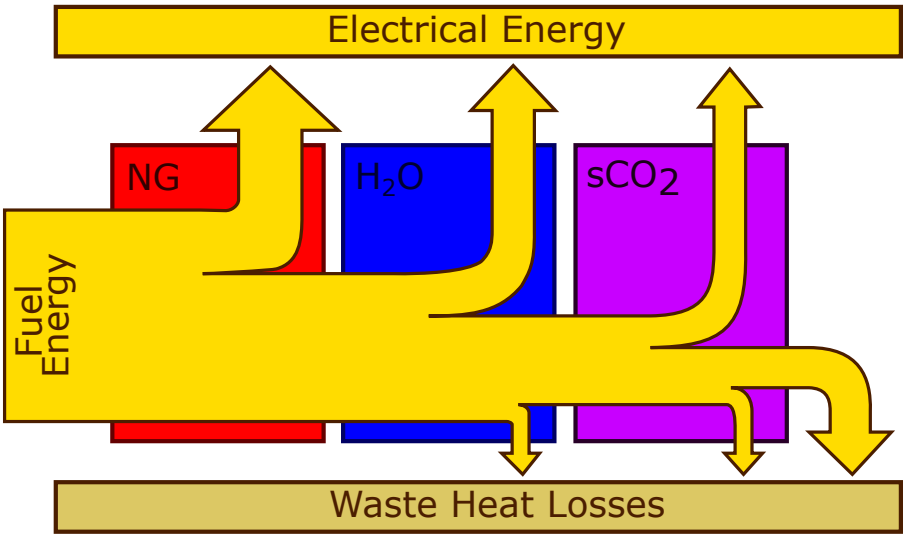

Figure 7.5: Energy flow for a CCPP with a steam Rankine bottoming cycle and subsequent sCO_2 Brayton bottoming cycle.

The sCO_2 Brayton cycle layouts will be referred to as the simple cycle, the simple recuperated cycle, the dual recuperated cycle, the recompression cycle, and dual recuperated

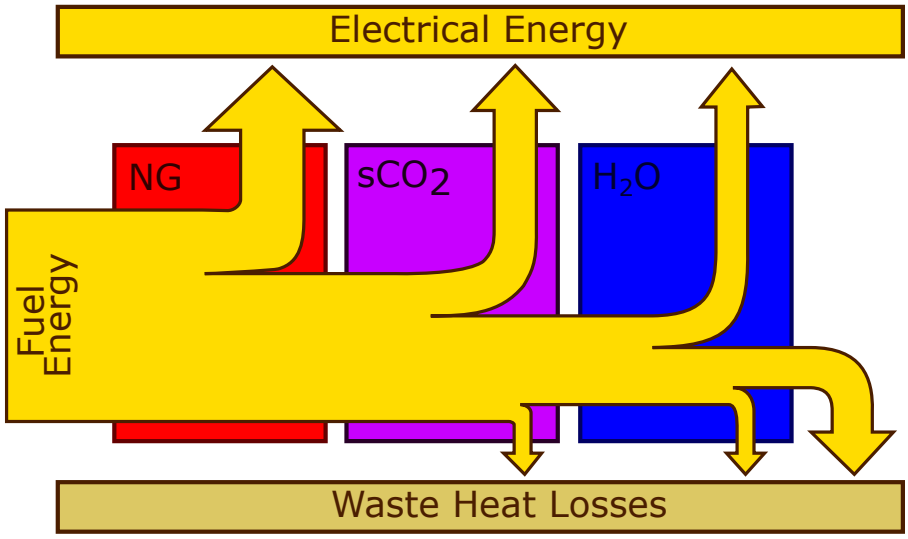

Figure 7.6: Energy flow for a CCPP with sCO_2 Brayton bottoming cycle and subsequent steam Rankine bottoming cycle.

Table 7.2: Components present in each cycle layout.

	Compressor	Turbine	WHR HEX	Chiller	Recuperator
Simple	1	1	1	1	-
Simple Recuperated	1	1	1	1	1
Dual Recuperated	1	2	1	1	2
Recompression	2	1	1	1	2
Dual Recuperated w/ split heating	1	2	2	1	2

cycle with split heating. Each of the cycles is made up of different combinations of the same components: compressors, turbines, and heat exchangers, including WHR heat exchangers, chillers, and recuperators. The more advanced sCO_2 cycle layouts incorporate various additional components in order to increase the thermal efficiency of the cycle. The inclusion of additional components of course also incurs additional costs, which must be weighed against efficiency gains. Table 7.2 shows the number of each component in a given cycle layout.

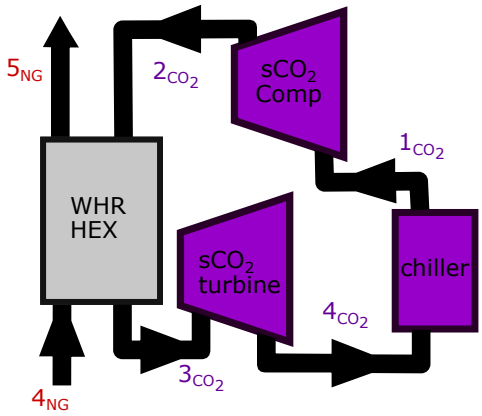

Figure 7.7: Simple sCO_2 Brayton cycle. [30]

Simple Brayton Cycle

The simple brayton cycle includes a compressor, a primary waste heat recovery heat exchanger, a turbine, and a chiller. The cycle layout is shown in figure 7.7.

Simple Recuperated Brayton Cycle

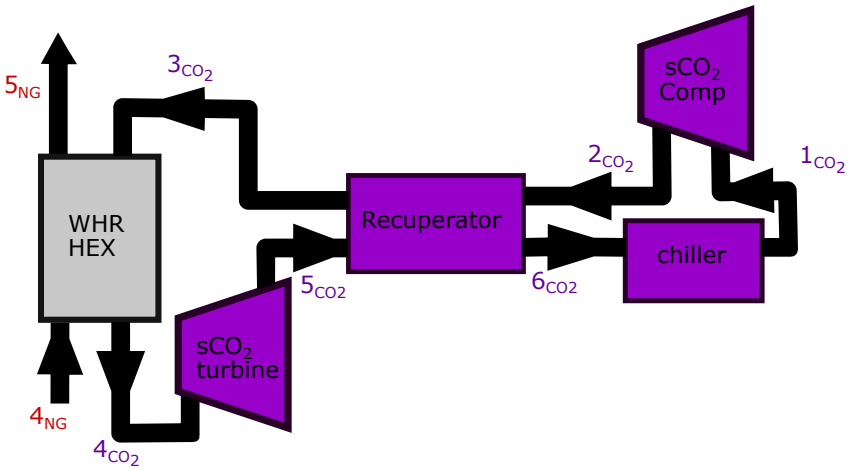

Figure 7.8: Simple recuperated sCO_2 Brayton cycle. [22]

The simple recuperated Brayton Cycle includes a compressor, a primary waste heat recovery heat exchanger, a recuperator, a turbine, and a chiller. The cycle layout is shown in figure 7.8.

Dual Recuperated Brayton Cycle

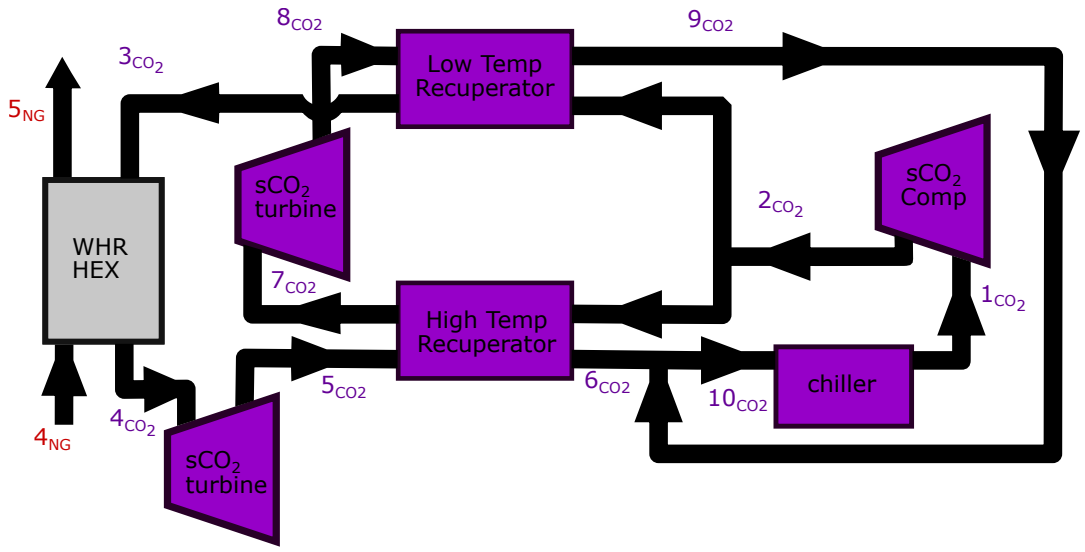

Figure 7.9: Dual recuperated sCO_2 Brayton cycle. [22]

The dual recuperated Brayton cycle includes a compressor, two recuperators, a primary WHR heat exchanger, two turbines, and a chiller, and has a split flow. The cycle layout is shown in figure 7.9.

Recompression Brayton Cycle

The recompression Brayton Cycle includes two compressors, two recuperators, a primary waste heat recovery heat exchanger, a turbine and a chiller and has one split flow. The cycle layout is shown in figure 7.10.

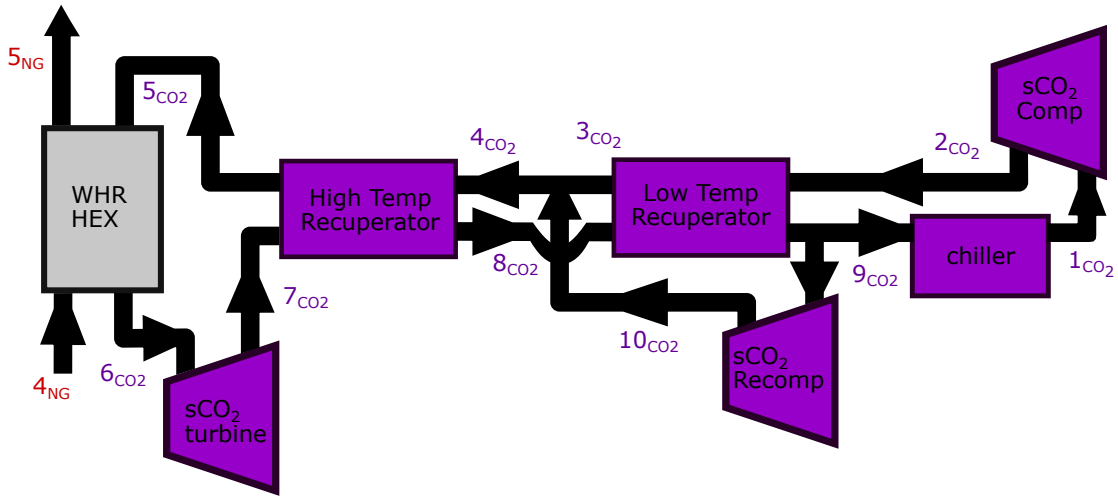

Figure 7.10: Recompression sCO_2 Brayton cycle. [22]

Dual recuperated Brayton cycle with split heating

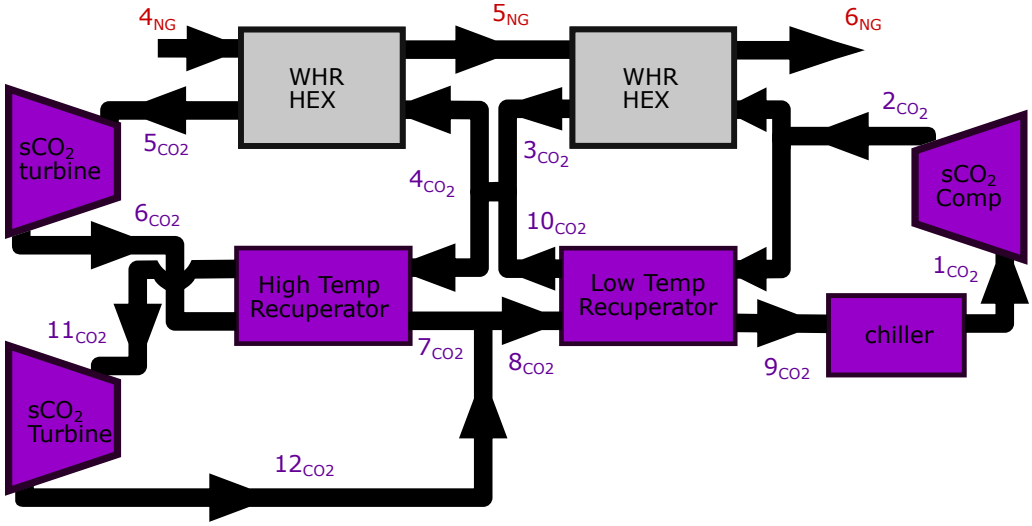

Figure 7.11: Dual recuperated sCO_2 Brayton cycle with split heating.

The dual recuperated Brayton cycle with split heating consists of a compressor, two recuperators, two waste heat recovery heat exchangers, two turbines, and a chiller, and features two split flows. The cycle layout is shown in figure 7.11.

7.4.2 Profitability

The various power plant layouts will be evaluated and compared in terms of profitability as determined by estimation of LCOE. LCOE will be estimated as a function of cycle electrical power outputs and assumed component costs. The procedure, patterned largely after that of Wright et al., is outlined in more detail in section 8.2. If the LCOE of a given plant layout is lower than that of a traditional CCPP, it is an indication that the layout may constitute a profitable alternative to the established CCPP layout.

CHAPTER 8
METHODOLOGY

8.1 Thermodynamic Modeling

In order to compare the various potential power plant layouts, power output and efficiency are determined for each. These are estimated with thermodynamic models at steady-state design point conditions.

Each of the five sCO_2 cycle layouts is modeled as both an independent bottoming cycle and as one of two bottoming cycles with a steam Rankine cycle as the other. In the case of two bottoming cycles, a model with the sCO_2 cycle preceding the steam Rankine cycle and a model with the sCO_2 cycle following the steam Rankine cycle are analyzed. This results in 15 complete models.

The natural gas turbine inlet temperature, $T_{\text{NG,turb},in}$, and the natural gas cycle compression ratio, CR_{NG}, and the sCO_2 compressor outlet pressure, $P_{\text{sCO}_2,\text{High}}$, are varied as parameters in every model. For the layouts in which they play a role, the steam Rankine cycle compression ratio, $\text{CR}_{\text{H}_2\text{O}}$, and mass split fraction (or fractions), y, are also varied as parameters. All other operation condition values remain fixed across all models. The combination of parameters resulting in the minimal LCOE is selected for the economic comparison of the various power plant layouts.

Thermodynamic modeling is conducted in the FCHART software Engineering Equation Solver (EES) and thermodynamic properties are determined using the built in thermodynamic properties library.

A module is written in EES for each of the seven cycles (the five sCO_2 Brayton cycle layouts, the natural gas cycle, and the steam Rankine cycle). The relevant cycle modules are then called within the main programs to analyze the various potential combinations.

Certain assumptions are made for all thermodynamic models in this work. It is assumed that there is no stray heat lost to the environment. It is also assumed that there is no pressure drop in pipes connecting the various components.

The thermodynamic models are built from mathematical models of the various components making up a cycle. The equations governing these models are discussed in the following section.

8.1.1 Component Models

All of the cycles to be analyzed are made up of similar basic components. The equations governing relationships between thermodynamic states are consistent for a given component and can be similarly applied in whichever cycle configuration the component appears. The components making up these cycles include compressors, turbines, heat exchangers, and flow splits and mergings.

Compressors and Pumps

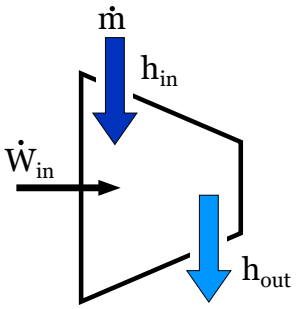

Figure 8.1: Compressor model. [30]

A compressor is shown symbolically in figure 8.1. Compressors in the model are assumed to have an isentropic efficiency, η_{comp}. The thermodynamic properties at the inlet and outlet of a compressor are related by

$$\eta_{\text{comp}} = \frac{h_{out,s} - h_{in}}{h_{out} - h_{in}}, \tag{8.1}$$

where h_{in} is the enthalpy of the working fluid at the compressor inlet, h_{out} is the enthalpy at the compressor outlet, and $h_{out,s}$ is the theoretical enthalpy at the outlet were the compression process reversible. The power input required for the compression is given by

$$\dot{W}_{in} = \dot{m}(h_{out} - h_{in}). \tag{8.2}$$

In the case of the steam Rankine cycle a pump is used rather than a compressor, but the same definition of isentropic efficiency and equation for required input power apply.

Turbines

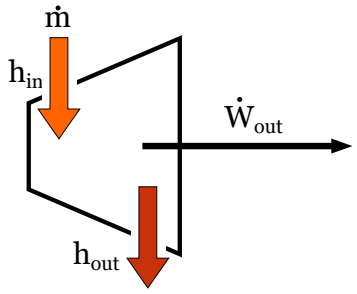

Figure 8.2: Turbine model. [30]

Figure 8.2 represents a turbine, also known as an expander. Turbines in the model are assumed to have an isentropic efficiency, η_{turb}, such that

$$\eta_{\text{turb}} = \frac{h_{in} - h_{out}}{h_{in} - h_{out,s}}. \tag{8.3}$$

Power output of a turbine is given by

$$\dot{W}_{out} = \dot{m}(h_{in} - h_{out}). \tag{8.4}$$

Generators

Generators are used to convert the power output of the turbine into electrical energy, and electrical power is similarly converted to drive the compressor. Generators are assumed to

have a mechanical efficiency, η_{mech} and an electrical efficiency, η_{el}. The electrical power output of a turbine is then

$$\dot{W}_{out,el} = \dot{W}_{out} \cdot \eta_{mech} \cdot \eta_{el}, \tag{8.5}$$

and the electrical power input required by a compressor is

$$\dot{W}_{in,el} = \frac{\dot{W}_{in}}{\eta_{mech} \cdot \eta_{el}}. \tag{8.6}$$

Heat Exchangers

The heat exchangers are modeled as counterflow heat exchangers using enthalpy based conservation of energy. A generic counterflow heat exchanger is represented in figure 8.3.

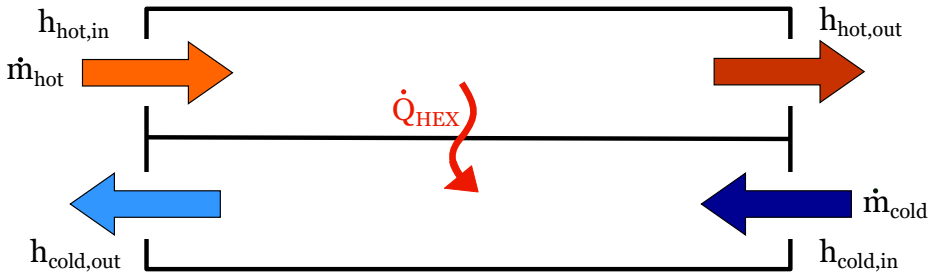

Figure 8.3: Generic counterflow heat exchanger model. [30]

$$\dot{Q}_{\text{HEX}} = \dot{m}_{\text{hot}}(h_{\text{hot},in} - h_{\text{hot},out}) = \dot{m}_{\text{cold}}(h_{\text{cold},out} - h_{\text{cold},in}), \tag{8.7}$$

where $\dot{Q}_{\text{HEX}}$ is the heat transferred within the heat exchanger, $\dot{m}_{\text{hot}}$ is the mass flow rate of the warmer fluid from which energy is extracted, $\dot{m}_{\text{cold}}$ is the mass flow rate of the cooler fluid to which heat energy is transferred, $h_{\text{hot},in}$ is the enthalpy of the warmer fluid at its inlet, $h_{\text{hot},out}$ is the enthalpy of the warmer fluid at its outlet, $h_{\text{cold},in}$ is the enthalpy of the cooler fluid at its inlet, and $h_{\text{cold},out}$ is the enthalpy of the cooler fluid at its outlet, as pictured in figure 8.3.

Further constraints on the heat exchangers are required to determine all related thermo-

dynamic states. Different constraints are applied in the models according to heat exchanger type.

The HRSG is modeled with assumed water qualities and a pinch-point temperature difference, discussed in more detail in section 8.1.4.

The WHR heat exchangers linking the natural gas cycle exhaust fumes with the sCO_2 cycles are modeled using assumed fixed temperature differences at inlets and outlets. This is discussed in more detail in section 8.1.5.

Recuperators are further constrained with an assumed fixed recuperator effectiveness. This is discussed in more detail in section 8.1.5.

Chillers and condensers are assumed to reject heat to constant temperature heat sinks. The thermodynamic states of the working fluid at the outlets are known fixed values and the thermodynamic states at the inlets are determined from other relationships in the cycle, and no further relationships are required. The heat rejected through the chiller or condenser is given by

$$\dot{Q}_{out} = \dot{m}(h_{in} - h_{out}). \tag{8.8}$$

A percentage pressure drop, $\Delta P_{\%}$, is assumed for some of the heat exchangers. This is applied using equation 8.9 or its equivalent, equation 8.10.

$$P_{out} = P_{in} - P_{in} \cdot \Delta P_{\%} \tag{8.9}$$

$$P_{in} = \frac{P_{out}}{1 - \Delta P_{\%}} \tag{8.10}$$

Split Flows

Certain of the cycles also include a split flow. When a flow is split, the thermodynamic state remains constant in the incoming and outgoing branches of the flow, but the mass

flow rates diverge. In this context, conservation of mass can be written as:

$$\dot{m}_{in} = \dot{m}_{out,1} + \dot{m}_{out,2}, \tag{8.11}$$

where $\dot{m}_{in}$ is the incoming mass flow rate and $\dot{m}_{out,1}$ and $\dot{m}_{out,2}$ are the outgoing mass flow rates, as represented in figure 8.4.

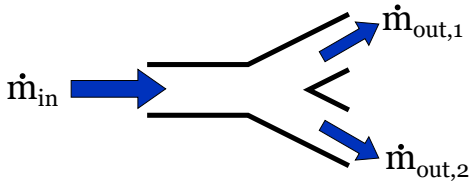

Figure 8.4: Flow split model.

The relationship between $\dot{m}_{out,1}$ and $\dot{m}_{out,2}$ is defined by the flow split fraction, y, which is defined as

$$y = \frac{\dot{m}_{out,1}}{\dot{m}_{in}}, \tag{8.12}$$

and which can be alternatively expressed as

$$y = 1 - \frac{\dot{m}_{out,2}}{\dot{m}_{in}}, \tag{8.13}$$

thanks to conservation of mass.

When these flows later rejoin each with independent thermodynamic states, the new thermodynamic state of the recombined outgoing flow can be determined with conservation of energy. Pressure is assumed to be constant in all three branches of flow (the two converging at the single outgoing). The additional state variables are related using enthalpic energy conservation:

$$\dot{m}_{in,1}h_{in,1} + \dot{m}_{in,2}h_{in,2} = \dot{m}_{out}h_{out}, \tag{8.14}$$

where $\dot{m}_{in,1}$ and $\dot{m}_{in,2}$ are the mass flow rates of the two incoming flows, $h_{in,1}$ and $h_{in,2}$

are the respective enthalpies of the two incoming streams, $\dot{m}_{out}$ is the mass flow rate of the united outgoing stream and h_{out} is the enthalpy of the outgoing stream, as represented in figure 8.5.

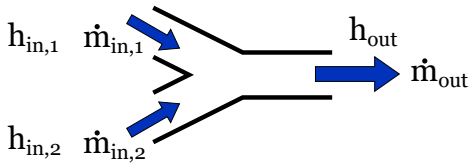

Figure 8.5: Model of split flow rejoining.

8.1.2 Power Cycle Models

Methods for modeling the power cycles are outlined in sections 8.1.3 through 8.1.5. In each of those sections, the system of equations used to determine the thermodynamic states of the cycle is summarized in a table. Table 8.3 presents the model for the natural gas cycle, table 8.6 for the steam Rankine cycle, table 8.9 for the simple sCO_2 Brayton cycle, table 8.10 for the simple recuperated cycle, table 8.11, table 8.12, and table 8.13 for the dual recuperated cycle with split heating.

The numbering of the states in each table is the same as the numbering in the corresponding cycle figure (figures 8.6, 8.7, 8.9, 8.10, 8.11, 8.12, and 8.13). The thermodynamic state variables temperature, T, pressure, P, specific enthalpy, h, and specific entropy, s, are displayed in their respective columns. In the case of the steam Rankine cycle, the water quality, x, is also displayed. Parameter values are indicated in each table with red text and assigned fixed values are indicated with blue text. Equations relating a thermodynamic state variable to the variables of other states are referenced in their corresponding cells. The word result is displayed in bold text for state variables which are determined by an attached cycle. Once two independent state variables are known for a given state, the other state variables can be determined with the fluid thermodynamic property library in EES.

Table 8.1: Natural gas cycle parameters.

Parameter	**Symbol**	**Minimum**	**Maximum**	**Units**
Turbine inlet temperature	$T_{\mathrm{NG},3}$	1200	1800	K
Compression Ratio	$\mathrm{CR}_{\mathrm{NG}}$	10	30	-

8.1.3 Natural Gas Brayton Cycle

The natural gas Brayton power cycle is modeled as a simple Brayton cycle, consisting of a compressor, a combustion chamber, and a turbine. The cycle is as represented in figure 8.6.

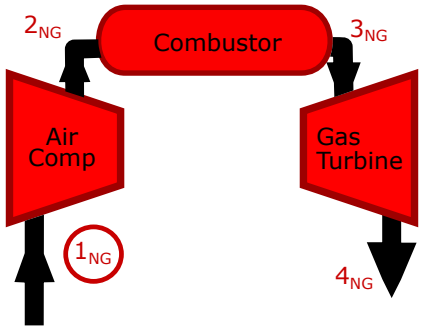

Figure 8.6: Simple natural gas Brayton cycle. [30]

Temperature at the turbine inlet, $T_{\mathrm{NG},1}$, and compression ratio, $\mathrm{CR}_{\mathrm{NG}}$, are chosen as input parameters for the model. The remaining thermodynamic states are calculated based upon these parameter values as well as fixed values of the cycle and values resulting from the models of the bottoming cycle or cycles. Table 8.1 shows these parameters and gives the minimum and maximum values of the range over which the parameters are varied.

Temperature at the turbine inlet, $T_{\mathrm{NG},1}$, is sampled at intervals of 100 K. Compression ratio, $\mathrm{CR}_{\mathrm{NG}}$, is sampled at intervals of 5.

Table 8.2 shows the variables in the model that are held constant for every run and their assigned values.

Temperature and pressure at the compressor inlet, $T_{\mathrm{NG},1}$ and P_{amb}, are chosen to correspond with the standard ISO 3977-2. [31] This standard also includes 60% humidity, but

Table 8.2: Natural gas cycle fixed values.

Parameter	**Symbol**	**Value**	**Units**
Compressor inlet temperature	$T_{\mathrm{NG},1}$	288.15	K
Ambient pressure	P_{amb}	101.3	kPa
Exhaust gas mass flow rate	$\dot{m}_{\mathrm{NG}}$	175	kg/s
Compressor isentropic efficiency	$\eta_{\mathrm{comp,NG}}$	0.92	-
Turbine isentropic efficiency	$\eta_{\mathrm{turb,NG}}$	0.90	-
Combustion chamber percentage pressure drop	$\Delta P_{\%,cc}$	5.4%	-
Generator mechanical efficiency	$\eta_{\mathrm{mech,NG}}$	0.99	-
Generator electrical efficiency	$\eta_{\mathrm{el,NG}}$	0.98	-

humidity is neglected in this model.

Values for compressor and turbine isentropic efficiencies, $\eta_{\mathrm{comp,NG}}$ and $\eta_{\mathrm{turb,NG}}$, combustion chamber percentage pressure drop, $\Delta P_{\%,cc}$ and generator mechanical and electrical efficiencies, $\eta_{\mathrm{mech,NG}}$ and $\eta_{\mathrm{el,NG}}$, are taken from Lindquist's doctoral thesis. [32]

The exhaust gas mass flow rate, $\dot{m}_{\mathrm{NG}}$, was chosen to match the power range of the class of power plants of interest.

It is assumed for the simplicity of the model that the thermodynamic properties of the exhaust gas mixture can be approximated as being equivalent to those of air. The working fluid is thus modeled as air, using the Air_ha properties from the EES property library, which uses the equation of state developed by Lemmon et al. [33]

The combustion process is modeled as simple heat addition to the air. The heat into the system is determined based on the combustion chamber inlet and outlet states:

$$\dot{Q}_{in} = \dot{m}_{\mathrm{NG}}(h_{\mathrm{NG},3} - h_{\mathrm{NG},2}). \tag{8.15}$$

Inefficiencies in combustion are neglected and it is assumed that the heat energy introduced to the system is equal to the heat of combustion of the fuel consumed.

Turbine outlet pressure, $P_{\mathrm{NG},4}$, is a result from the attached bottoming cycles, as the

Table 8.3: Thermodynamic states of the natural gas cycle.

State	Location	T	P	h	s
1_{NG}	compressor inlet	$T_{\mathrm{NG},1}$	P_{amb}	η_{comp} (8.1)	
$2_{\mathrm{NG},s}$	isentropic compressor outlet		$= P_{\mathrm{NG},2}$	η_{comp} (8.1)	$= s_{\mathrm{NG},1}$
2_{NG}	compressor outlet, combustor inlet		$=\mathrm{CR}_{\mathrm{NG}} P_{\mathrm{NG},1}$	η_{comp} (8.1)	
3_{NG}	combustor outlet, turbine inlet	$T_{\mathrm{NG},3}$	$\Delta P_{\%,cc}$ (8.9)	η_{turb} (8.3)	
$4_{\mathrm{NG},s}$	isentropic turbine outlet		$= P_{\mathrm{NG},4}$	η_{turb} (8.3)	$= s_{\mathrm{NG},3}$
4_{NG}	turbine outlet, chiller inlet		**Result**	η_{turb} (8.3)	

pressure at the final exhaust gas heat exchanger outlet will be equal to the ambient pressure, P_{amb} after a pressure drop across the heat exchanger or heat exchangers.

Each of the equations and parameters are entered into a module in EES, which performs the calculations.

8.1.4 Steam Rankine Cycle

The steam cycle used as a bottoming cycle is modeled as a simple Rankine cycle with superheating, as seen in figure 8.7. The cycle consists of a pump, the HRSG (made up of the evaporator, economizer, and superheater), a turbine, and a condenser.

The working fluid is modeled using Water from the EES thermodynamic property library, which uses the property correlations issued by the International Association for the Properties of Water and Steam (IAPWS). [34]

The cycle model varies compression ratio of the pump, $\mathrm{CR}_{\mathrm{H_2O}}$, as a parameter with the range displayed in table 8.4. The compression ratio values were chosen to match the general range of highest pressures found in the example cycles provided by Kehlhofer, Rukes, Hannemann, and Stirnimann [15].

The compression ratio of the pump, $\mathrm{CR}_{\mathrm{H_2O}}$, is sampled with an interval of 200.

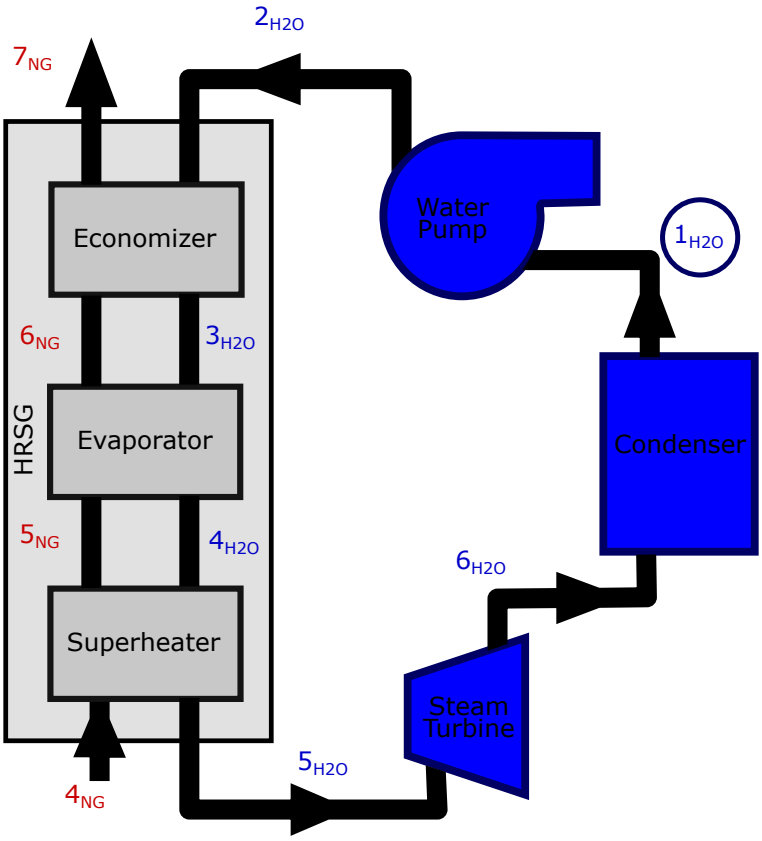

Figure 8.7: Steam Rankine cycle layout. [30]

Table 8.4: Steam Rankine parameters.

Parameter	**Symbol**	**Minimum**	**Maximum**	**Units**
Compression Ratio	CR_{H_2O}	2000	3400	-

The fixed values that are assigned for the steam Rankine cycle are shown in table 8.5.

The water at the condenser outlet and evaporator inlet is modeled as a saturated liquid ($x_{H_2O,1} = 0$, $x_{H_2O,3} = 0$) and the steam at the evaporator outlet is modeled as a saturated gas($x_{H_2O,4} = 1$). In practice there is an approach temperature difference such that the evaporator inlet temperature is 5 to 10 K below the saturation temperature to account for off design conditions, but that is neglected in this model.

The water at the steam turbine outlet is modeled as a saturated gas unless the corre-

Table 8.5: Steam Rankine cycle fixed values.

Parameter	**Symbol**	**Value**	**Units**
Condenser outlet temperature	$T_{\mathrm{H_2O},1}$	304	K
Condenser outlet quality	$x_{\mathrm{H_2O},1}$	0	-
Evaporator inlet quality	$x_{\mathrm{H_2O},3}$	0	-
Evaporator outlet quality	$x_{\mathrm{H_2O},4}$	1	-
HRSG pinchpoint temperature difference	$\Delta T_{pp,\mathrm{HRSG}}$	15	K
Pump isentropic efficiency	$\eta_{pump,\mathrm{H_2O}}$	0.90	-
Turbine isentropic efficiency	$\eta_{turb,\mathrm{H_2O}}$	0.90	-
HRSG exhaust gas percentage pressure drop	$\Delta P_{\%,\mathrm{HRSG,NG}}$	1%	-
Generator mechanical efficiency	$\eta_{\mathrm{mech},\mathrm{H_2O}}$	0.99	-
Generator electrical efficiency	$\eta_{\mathrm{mech},\mathrm{H_2O}}$	0.99	-

sponding temperature at the steam turbine inlet exceeds a maximum temperature, $T_{\mathrm{H_2O},max}$. $T_{\mathrm{H_2O},max}$ is assigned as either 900 K or 15 K less than the exhaust gas temperature at the superheater inlet, $T_{\mathrm{NG},4}$, whichever is lower. If this is the case, the temperature at the steam turbine inlet, $T_{\mathrm{H_2O},5}$ is assumed to be equal to the maximum temperature, $T_{\mathrm{H_2O},max}$ and the state of the water at the turbine outlet is determined accordingly.

The pinchpoint temperature difference for the HRSG, $\Delta T_{pp,\mathrm{HRSG}}$, is the the temperature difference between the water at the evaporator inlet and the exhaust gas at the evaporator outlet, as shown in equation 8.16, and is the lowest temperature difference along the length of the HRSG because of the latent heat of the water, as visually demonstrated in figure 8.8.

$$\Delta T_{pp,\mathrm{H_2O}} = T_{\mathrm{NG},6} - T_{\mathrm{H_2O},3}. \tag{8.16}$$

The exhaust gas in the HRSG is modeled with a pressure drop, $\Delta P_{\%,\mathrm{HRSG,NG}}$, which is applied to each of the three segments individually. No pressure drops are included in the model for the water in the HRSG.

The remaining thermodynamic states are ascertained from the parameters, fixed values,

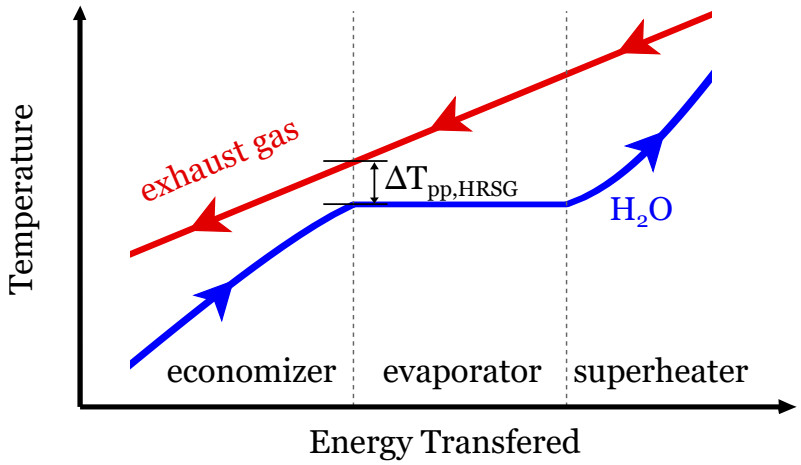

Figure 8.8: Pinchpoint temperature difference between exhaust gas and water in HRSG. [15]

and equations governing the system components. These are represented in table 8.6.

The numbering for the exhaust gas in the figures and state variable tables assumes the steam Rankine cycle comes directly after the natural gas cycle, though that may not always be the case as it is preceded by a sCO_2 bottoming cycle in certain model configurations.

Each of the given parameters and equations are entered into EES, where the remaining thermodynamic states and properties are determined.

Table 8.6: Thermodynamic states and equations for the steam Rankine cycle.

State	Location	T	P	h	s	x
4_{NG}	turb out, sup heat in	**Result**	$\Delta P_{\%}$ (8.10)	**Result** $\Delta \dot{E}_{sh}$ (8.7)	**Result**	
5_{NG}	sup heat out, evap in		$\Delta P_{\%}$ (8.10)	$\Delta \dot{E}_{ev}$ (8.7), $\Delta \dot{E}_{sh}$ (8.7)		
6_{NG}	evap out, econ in	ΔT_{pp} (8.16)	$\Delta P_{\%}$ (8.10)	$\Delta \dot{E}_{ec}$ (8.7), $\Delta \dot{E}_{ev}$ (8.7)		
7_{NG}	econ out		P_{amb} or **Result**	$\Delta \dot{E}_{ev}$ (8.7)		
$1_{\text{H}_2\text{O}}$	pump in, cond out	$T_{\text{H}_2\text{O},1}$	$P_{\text{H}_2\text{O,Sat}}$	η_{pump} (8.1)		0
$2_{\text{H}_2\text{O},s}$	isentropic pump out		$= P_{\text{H}_2\text{O},2}$	η_{pump} (8.1)	$= s_{\text{H}_2\text{O},1}$	
$2_{\text{H}_2\text{O}}$	pump out, econ in		$\text{CR}_{\text{H}_2\text{O}} P_{\text{H}_2\text{O},1}$	η_{pump} (**??**), $\Delta \dot{E}_{ec}$ (8.7)		
$3_{\text{H}_2\text{O}}$	econ out, evap in	ΔT_{pp} (8.16)	$= P_{\text{H}_2\text{O},2}$	$\Delta \dot{E}_{ec}$(8.7), $\Delta \dot{E}_{ev}$(8.7)		0
$4_{\text{H}_2\text{O}}$	evap out, sup heat in		$= P_{\text{H}_2\text{O},2}$	$\Delta \dot{E}_{ev}$ (8.7), $\Delta \dot{E}_{sh}$ (8.7)		1
$5_{\text{H}_2\text{O}}$	sup heat out, turb in		$= P_{\text{H}_2\text{O},2}$	η_{turb} (8.3), $\Delta \dot{E}_{sh}$ (8.7)		
$6_{\text{H}_2\text{O},s}$	isentropic turb out		$= P_{\text{H}_2\text{O},6}$	η_{turb} (8.3)	$= s_{\text{H}_2\text{O},5}$	
$6_{\text{H}_2\text{O}}$	turb out, chiller in		$= P_{\text{H}_2\text{O},1}$	η_{turb} (8.3)		

8.1.5 sCO_2 Brayton Cycles

Each of the sCO_2 Brayton cycle configurations introduced in section 7.4.1 are modeled separately with the same parameter values and assigned fixed values, except in the case where a given value does not apply to a given cycle layout. Table 8.7 displays the parameters applied to the cycles with range maximums and minimums.

The pressure of the carbon dioxide at the compressor outlet, $P_{\text{CO}_2,\text{High}}$, is varied as a parameter for each of the sCO_2 cycles. The dual recuperated cycle and the recompression cycle additionally have the flow split fraction, y, varied as a parameter. The dual recuper-

Table 8.7: sCO_2 Brayton cycle parameters.

Parameter	Symbol	Minimum	Maximum	Units
sCO_2 compressor outlet pressure	$P_{\mathrm{CO}_2,High}$	16000	32000	kPa
Mass flow split fractions	y	> 0	< 1	-

ated cycle with split heating has two flow split fractions, y_1 and y_2, varied as parameters over the range, one for each flow split.

The pressure of the carbon dioxide at the compressor outlet, $P_{\mathrm{CO}_2,High}$, is sampled at an interval of 2000 kPa. The flow split fraction, y, is sampled between 0.1 and 0.9 at intervals of 0.2.

Table 8.8 lists the assigned fixed values applied to each of the sCO_2 cycles.

Table 8.8: sCO_2 Brayton cycle fixed values.

Parameter	Symbol	Value	Units
Compressor inlet temperature	$T_{\mathrm{CO}_2,1}$	305.5	K
Compressor inlet pressure	P_{amb}	7700	kPa
WHR heat exchanger pinchpoint temperature difference	$\Delta T_{pp,\mathrm{WHR}}$	15	K
LTR effectiveness	$\mathrm{Eff}_{\mathrm{LTR}}$	0.91	-
HTR heat exchanger effectiveness	$\mathrm{Eff}_{\mathrm{HTR}}$	0.95	-
Percentage pressure drop in heat exchangers	$\Delta P_{\%,\mathrm{HEX},\mathrm{CO}_2}$	1%	-
WHR exhaust gas percentage pressure drop	$\Delta P_{\%,\mathrm{WHR},\mathrm{NG}}$	1%	-
Compressor isentropic efficiency	$\eta_{comp,\mathrm{CO}_2}$	0.82	-
Turbine isentropic efficiency	$\eta_{turb,\mathrm{CO}_2}$	0.85	-
Generator mechanical efficiency	$\eta_{\mathrm{mech},\mathrm{CO}_2}$	0.97	-
Generator electrical efficiency	$\eta_{\mathrm{mech},\mathrm{CO}_2}$	0.96	-

The fixed values pertaining to heat exchangers are applied only in those cycles where the type of heat exchanger is present. All cycles have a WHR heat exchanger, but the dual recuperated cycle with split heating has two WHR heat exchangers. The WHR heat exchanger pinchpoint temperature difference, $\Delta T_{pp,\mathrm{WHR}}$, is applied to both sides of the heat

exchanger, such that both

$$T_{\text{NG},in} - T_{\text{CO}_2,out} = \Delta T_{pp,\text{WHR}} \tag{8.17}$$

and

$$T_{\text{NG},out} - T_{\text{CO}_2,in} = \Delta T_{pp,\text{WHR}}. \tag{8.18}$$

In the case of one of the WHR heat exchangers in the dual recuperated cycle with split heating, the temperature difference is only applied between the exhaust gas outlet and sCO_2 inlet.

Recuperators are further constrained by an assumed recuperator effectiveness, Eff_{Rec}, which relates the actual heat transfer rate, $\dot{Q}_{\text{actual}}$, to a theoretical maximum potential heat transfer rate, $\dot{Q}_{max}$: [22]

$$\text{Eff}_{\text{Rec}} = \frac{\dot{Q}_{\text{actual}}}{\dot{Q}_{\text{max}}}. \tag{8.19}$$

The theoretical maximum potential heat transfer of the recuperator is determined by first determining the theoretical maximum heat transfer rate of the hot side, $\dot{Q}_{\text{hot},max}$, and of the cold side, $\dot{Q}_{\text{cold},max}$,

$$\dot{Q}_{\text{hot},max} = \dot{m}_{\text{hot}} \left[h\left(T_{\text{hot},in}, P_{\text{hot},in}\right) - h\left(T_{\text{cold},in}, P_{\text{hot},out}\right) \right] \tag{8.20}$$

$$\dot{Q}_{\text{cold},max} = \dot{m}_{\text{cold}} \left[h\left(T_{\text{hot},in}, P_{\text{cold},in}\right) - h\left(T_{\text{cold},in}, P_{\text{cold},out}\right) \right] \tag{8.21}$$

where $h\left(T, P\right)$ is the enthalpy of the fluid at temperature T and pressure P, with the subscripts hot and cold referring to the hot and cold side of the recuperator and with the subscripts in and out referring to the inlet and outlet, respectively.

The lesser of the two theoretical maximum potential heat transfer rate values is then

determined to be the theoretical maximum potential heat transfer rate for the recuperator:

$$\dot{Q}_{max} = \min(\dot{Q}_{\text{hot},max}, \dot{q}_{\text{cold},max}). \tag{8.22}$$

In the cycles with two recuperators they are referred to separately as the low temperature recuperator (LTR) and high temperature recuperator (HTR). In the simple recuperated cycle, which only has one recuperator, the HTR effectiveness, $\text{Eff}_{\text{HTR}} = 0.95$, is used.

The remaining thermodynamic states in each of the cycles are calculated for each combination of parameters using the component equations and assigned fixed values. This is discussed in greater detail for each of the cycles in the following subsections.

The thermodynamic state variables are related using CarbonDioxide from the EES thermodynamic property library, which uses Span and Wagner's equation of state. [35]

The numbering for the exhaust gas in the state variable tables assumes the cycle comes directly after the natural gas cycle, though that may not always be the case as it is preceded by a steam Rankine bottoming cycle in certain model configurations.

Simple sCO_2 Brayton cycle

The simple sCO_2 Brayton cycle configuration is represented in the introductory section in figure 7.7 as well as here in figure 8.9 with its state variables.

Table 8.9 includes the parameters and equations necessary for the thermodynamic model of the simple sCO_2 Brayton cycle. Each of the given parameters and equations are entered into EES, where the remaining thermodynamic states and properties are determined.

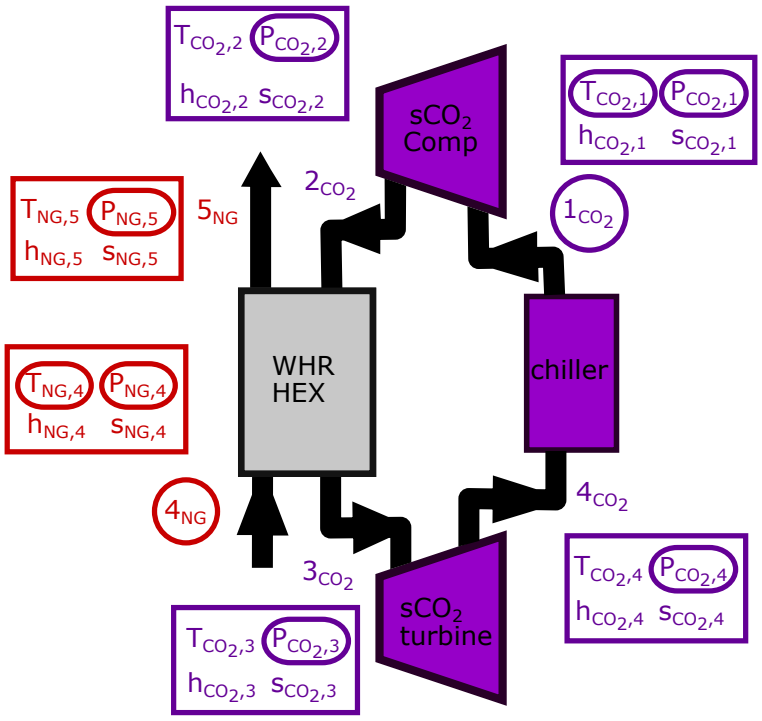

Figure 8.9: Simple sCO_2 Brayton cycle with state variables.

Table 8.9: Thermodynamic states and equations for the simple cycle.

State	Location	T	P	h	s
4_{NG}	turb out, WHR in	**Result** ΔT_{pp} (8.17)	$\Delta P_{\%}$ (8.10)	**Result** $\Delta \dot{E}_{WHR}$ (8.7)	**Result**
5_{NG}	WHR out	ΔT_{pp} (8.18)	P_{amb} or **Result**	$\Delta \dot{E}_{WHR}$ (8.7)	
1_{CO_2}	comp in, chiller out	$T_{CO_2,1}$	$P_{CO_2,Low}$	η_{comp} (8.1)	
$2_{CO_2,s}$	isentropic comp out		$= P_{CO_2,2}$	η_{comp} (8.1)	$= s_{CO_2,1}$
2_{CO_2}	comp out, WHR in	ΔT_{pp} (8.18)	$P_{CO_2,High}$	η_{comp} (8.1), $\Delta \dot{E}_{WHR}$ (8.7)	
3_{CO_2}	WHR out, turb in	ΔT_{pp} (8.17)	$\Delta P_{\%}$ (8.9)	η_{turb} (8.3), $\Delta \dot{E}_{WHR}$ (8.7)	
$4_{CO_2,s}$	isentropic turb out		$= P_{CO_2,4}$	η_{turb} (8.3)	$= s_{CO_2,3}$
4_{CO_2}	turb out, chiller in		$\Delta P_{\%}$ (8.10)	η_{turb} (8.3)	

Simple recuperated sCO_2 Brayton cycle

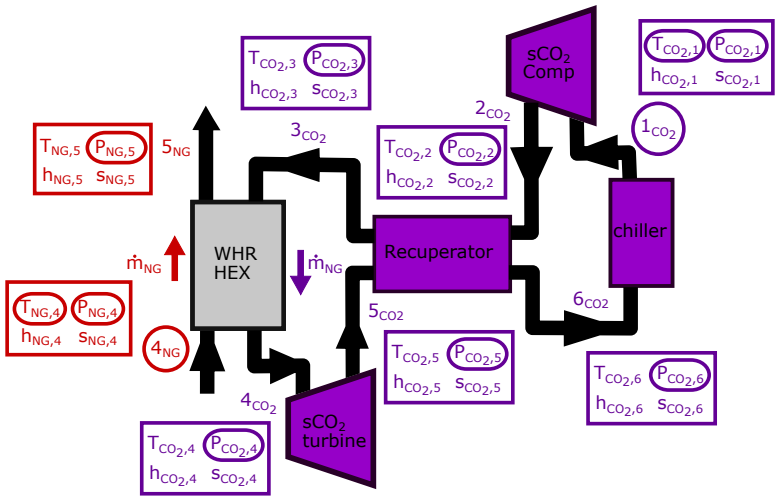

Figure 8.10: Simple recuperated sCO_2 Brayton cycle with state variables.

Figure 8.10 shows the simple recuperated sCO_2 Brayton cycle layout complete with its state variables.

The equations and values defining the thermodynamic model used for the simple recuperated sCO_2 Brayton cycle are enshrined in table 8.10

The given parameters and equations are written into an EES module, which determines the remaining thermodynamic states and properties.

Table 8.10: Thermodynamic states and equations for the simple recuperated cycle.

State	Location	T	P	h	s
4_{NG}	turb out, WHR in	**Result** ΔT_{pp} (8.17)	$\Delta P_{\%}$ (8.10)	**Result** $\Delta \dot{E}_{WHR}$ (8.7)	**Result**
5_{NG}	WHR out	ΔT_{pp} (8.18)	P_{amb} or **Result**	$\Delta \dot{E}_{WHR}$ (8.7)	
1_{CO_2}	comp in, chiller out	$T_{CO_2,1}$	$P_{CO_2,Low}$	η_{comp} (8.1)	
$2_{CO_2,s}$	isentropic comp out		$= P_{CO_2,2}$	η_{comp} (8.1)	$= s_{CO_2,1}$
2_{CO_2}	comp out, rec in		$P_{CO_2,High}$	η_{comp} (8.1), Eff_{Rec} (8.19), $\Delta \dot{E}_{Rec}$ (8.7)	
3_{CO_2}	rec out, WHR in	ΔT_{pp} (8.18)	$\Delta P_{\%}$ (8.9)	$\Delta \dot{E}_{WHR}$ (8.7), $\Delta \dot{E}_{Rec}$ (8.7), Eff_{Rec} (8.19)	
4_{CO_2}	WHR out, turb in	ΔT_{pp} (8.17)	$\Delta P_{\%}$ (8.9)	η_{turb} (8.3), $\Delta \dot{E}_{WHR}$ (8.7)	
$5_{CO_2,s}$	isentropic turb out		$= P_{CO_2,5}$	η_{turb} (8.3)	$= s_{CO_2,4}$
5_{CO_2}	turb out, rec in		$\Delta P_{\%}$ (8.10)	η_{turb} (8.3), Eff_{Rec} (8.19), $\Delta \dot{E}_{Rec}$ (8.7)	
6_{CO_2}	rec out, chiller in		$\Delta P_{\%}$ (8.10)	$\Delta \dot{E}_{Rec}$ (8.7), Eff_{Rec} (8.19)	

Dual recuperated sCO_2 Brayton cycle

The dual recuperated sCO_2 Brayton cycle configuration, with its state variables, is represented in figure 8.11.

Table 8.11 summarizes the parameters and equations necessary for the thermodynamic model of the dual recuperated sCO_2 Brayton cycle, as is described in section 8.1.2.

The values and system of equations described in the table are entered into EES, where the remaining thermodynamic states and properties are determined.

Table 8.11: Thermodynamic states and equations for the dual recuperated cycle.

State	Location	T	P	h	s
4_{NG}	turb out, WHR in	**Result** ΔT_{pp} (8.17)	$\Delta P_{\%}$ (8.10)	**Result** $\Delta \dot{E}_{\text{WHR}}$ (8.7)	**Result**
5_{NG}	WHR out	ΔT_{pp} (8.18)	P_{amb} or **Result**	$\Delta \dot{E}_{\text{WHR}}$ (8.7)	
1_{CO_2}	comp in, chiller out	$T_{\text{CO}_2,1}$	$P_{\text{CO}_2,\text{Low}}$	η_{comp} (8.1)	
$2_{\text{CO}_2,s}$	isentropic comp out		$= P_{\text{CO}_2,2}$	η_{comp} (8.1)	$= s_{\text{CO}_2,1}$
2_{CO_2}	comp out, LTR in, HTR in		$P_{\text{CO}_2,\text{High}}$	η_{comp} (8.1), Eff_{LTR} (8.19), Eff_{HTR} (8.19), $\Delta \dot{E}_{\text{LTR}}$ (8.7), $\Delta \dot{E}_{\text{HTR}}$ (8.7)	
3_{CO_2}	LTR out, WHR in	ΔT_{pp} (8.18)	$\Delta P_{\%}$ (8.9)	$\Delta \dot{E}_{\text{WHR}}$ (8.7), $\Delta \dot{E}_{\text{LTR}}$ (8.7), Eff_{LTR} (8.19)	
4_{CO_2}	WHR out, turb 1 in	ΔT_{pp} (8.17)	$\Delta P_{\%}$ (8.9)	$\eta_{\text{turb},1}$ (8.3), $\Delta \dot{E}_{\text{WHR}}$ (8.7)	
$5_{\text{CO}_2,s}$	isentropic turb 1 out		$P_{\text{CO}_2,5}$	$\eta_{\text{turb},1}$ (8.3)	$= s_{\text{CO}_2,4}$
5_{CO_2}	turb 1 out, HTR inlet		$\Delta P_{\%}$ (8.10)	$\eta_{\text{turb},1}$ (8.3), Eff_{HTR} (8.19), $\Delta \dot{E}_{\text{HTR}}$ (8.7)	
6_{CO_2}	HTR out, flow-join in		$= P_{\text{CO}_2,10}$	$\Delta \dot{E}_{\text{HTR}}$ (8.7), Eff_{HTR} (8.19), $\Delta \dot{E}_{\text{fj}}$ (8.14)	
7_{CO_2}	HTR out, turb 2 in		$\Delta P_{\%}$ (8.9)	$\eta_{\text{turb},2}$ (8.3), $\Delta \dot{E}_{\text{HTR}}$ (8.7), Eff_{HTR} (8.19)	
$8_{\text{CO}_2,s}$	isentropic turb 2 out		$= P_{\text{CO}_2,8}$	$\eta_{\text{turb},2}$ (8.3)	$= s_{\text{CO}_2,7}$
8_{CO_2}	turb 2 out LTR in		$\Delta P_{\%}$ (8.10)	$\eta_{\text{turb},2}$ (8.3), $\Delta \dot{E}_{\text{LTR}}$ (8.7), Eff_{LTR} (8.19)	
9_{CO_2}	LTR out flow-join in		$= P_{\text{CO}_2,10}$	$\Delta \dot{E}_{\text{LTR}}$ (8.7), Eff_{LTR} (8.19), $\Delta \dot{E}_{\text{fj}}$ (8.14)	
10_{CO_2}	flow-join out chiller in		$\Delta P_{\%}$ (8.10)	$\Delta \dot{E}_{\text{fj}}$ (8.14)	

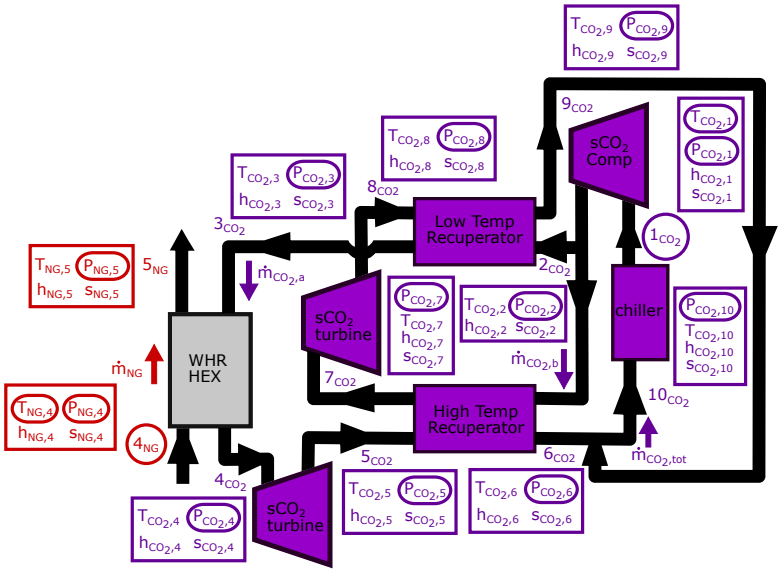

Figure 8.11: Dual recuperated sCO_2 Brayton cycle with state variables.

Recompression sCO_2 Brayton cycle

The recompression sCO_2 Brayton cycle configuration is represented in figure 8.12 with its state variables and table 8.12 includes the parameters and equations necessary for the thermodynamic model of the recompression sCO_2 Brayton cycle.

Each of the given parameters and equations are entered into EES, which is used to determine the remaining thermodynamic states and properties.

Table 8.12: Thermodynamic states and equations for the recompression cycle.

State	Location	T	P	h	s
4_{NG}	turb out, WHR in	**Result** ΔT_{pp} (8.17)	$\Delta P_{\%}$ (8.10)	**Result** $\Delta \dot{E}_{\text{WHR}}$ (8.7)	**Result**
5_{NG}	WHR out	ΔT_{pp} (8.18)	P_{amb} or **Result**	$\Delta \dot{E}_{\text{WHR}}$ (8.7)	
1_{CO_2}	comp in, chiller out	$T_{\text{CO}_2,1}$	$P_{\text{CO}_2,\text{Low}}$	$\eta_{\text{comp},1}$ (8.1)	
$2_{\text{CO}_2,s}$	isentropic comp out		$= P_{\text{CO}_2,2}$	$\eta_{\text{comp},1}$ (8.1)	$= s_{\text{CO}_2,1}$
2_{CO_2}	comp out, LTR in		$P_{\text{CO}_2,\text{High}}$	$\eta_{\text{comp},1}$ (8.1), Eff_{LTR} (8.19), $\Delta \dot{E}_{\text{LTR}}$ (8.7)	
3_{CO_2}	LTR out, flow-join in		$= P_{\text{CO}_2,10}$	$\Delta \dot{E}_{\text{LTR}}$ (8.7), $\Delta \dot{E}_{\text{fj}}$ (8.14), Eff_{LTR} (8.19)	
4_{CO_2}	flow-join out, HTR in		$= P_{\text{CO}_2,10}$	$\Delta \dot{E}_{\text{HTR}}$ (8.7), Eff_{HTR} (8.19), $\Delta \dot{E}_{\text{fj}}$ (8.14)	
5_{CO_2}	HTR out, WHR in	ΔT_{pp} (8.18)	$\Delta P_{\%}$ (8.9)	$\Delta \dot{E}_{\text{WHR}}$ (8.7), $\Delta \dot{E}_{\text{HTR}}$ (8.7), Eff_{HTR} (8.19)	
6_{CO_2}	WHR out, turb in	ΔT_{pp} (8.17)	$\Delta P_{\%}$ (8.9)	η_{turb} (8.3), $\Delta \dot{E}_{\text{WHR}}$ (8.7)	
$7_{\text{CO}_2,s}$	isentropic turb out		$= P_{\text{CO}_2,7}$	η_{turb} (8.3)	$= s_{\text{CO}_2,6}$
7_{CO_2}	turb out, HTR in		$\Delta P_{\%}$ (8.10)	η_{turb} (8.3), $\Delta \dot{E}_{\text{HTR}}$ (8.7), Eff_{HTR} (8.19)	
8_{CO_2}	HTR out LTR in		$\Delta P_{\%}$ (8.10)	$\Delta \dot{E}_{\text{LTR}}$ (8.7), Eff_{LTR} (8.19), $\Delta \dot{E}_{\text{HTR}}$ (8.7), Eff_{HTR} (8.19)	
9_{CO_2}	LTR out, comp 2 in, chiller in		$\Delta P_{\%}$ (8.10)	$\eta_{\text{comp},2}$ (8.1), $\Delta \dot{E}_{\text{LTR}}$ (8.7), Eff_{LTR} (8.19),	
$10_{\text{CO}_2,s}$	isentropic comp 2 out		$= P_{\text{CO}_2,10}$	$\eta_{\text{comp},2}$ (8.1)	$= s_{\text{CO}_2,9}$
10_{CO_2}	comp 2 out flow-join in		$P_{\text{CO}_2,\text{High}}$	$\eta_{\text{comp},2}$ (8.1) $\Delta \dot{E}_{\text{fj}}$ (8.14)	

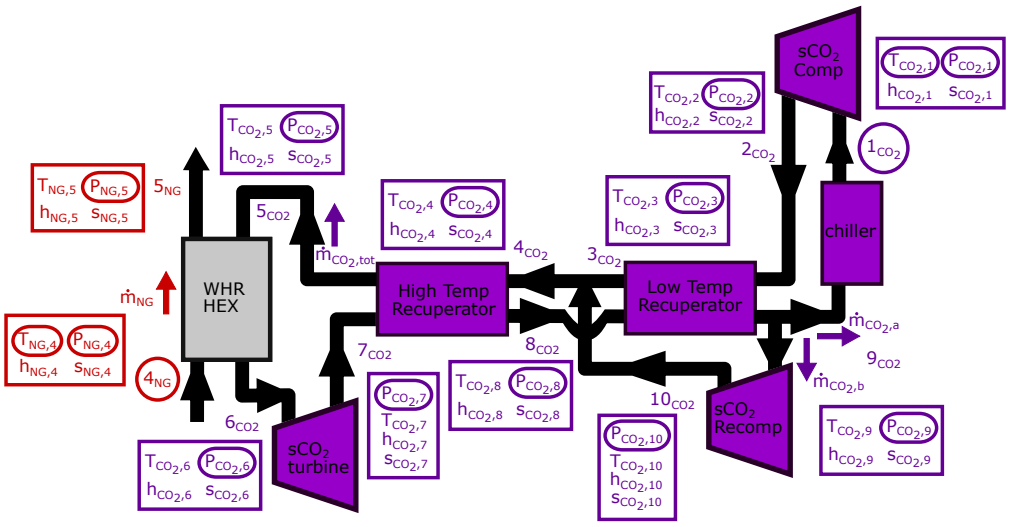

Figure 8.12: Recompression sCO_2 Brayton cycle with state variables.

Dual recuperated sCO_2 Brayton cycle with split heating

A diagram of the dual recuperated sCO_2 Brayton cycle with split heating is shown in figure 8.13 with its state variables.

The values and system of equations defining the dual recuperated sCO_2 Brayton cycle are represented in table 8.13.

An EES module is used to determine the remaining thermodynamic states and properties.

Table 8.13: Thermodynamic states for the dual recuperated cycle with split heating.

State	Location	T	P	h	s
4_{NG}	turb out, WHR2 in	**Result**	$\Delta P_{\%}$ (8.10)	**Result** $\Delta\dot{E}_{\mathrm{WHR},2}$ (8.7)	**Result**
5_{NG}	WHR2 out, WHR1 in	ΔT_{pp} (8.18)	$\Delta P_{\%}$ (8.10)	$\Delta\dot{E}_{\mathrm{WHR},1}$ (8.7), $\Delta\dot{E}_{\mathrm{WHR},2}$ (8.7)	
6_{NG}	WHR1 out	ΔT_{pp} (8.17)	P_{amb} or **Result**	$\Delta\dot{E}_{\mathrm{WHR},1}$ (8.7)	
$1_{\mathrm{CO_2}}$	comp in, chiller out	$T_{\mathrm{CO_2},1}$	$P_{\mathrm{CO_2,Low}}$	η_{comp} (8.1)	
$2_{\mathrm{CO_2},s}$	isentropic comp out		$= P_{\mathrm{CO_2},2}$	η_{comp} (8.1)	$= s_{\mathrm{CO_2},1}$
$2_{\mathrm{CO_2}}$	comp out, LTR in, WHR1 in	ΔT_{pp} (8.18)	$P_{\mathrm{CO_2,High}}$	η_{comp} (8.1), $\Delta\dot{E}_{\mathrm{WHR},1}$ (8.7), $\Delta\dot{E}_{\mathrm{LTR}}$ (8.7), $\mathrm{Eff}_{\mathrm{LTR}}$ (8.19)	
$3_{\mathrm{CO_2}}$	WHR1 out, flow-join1 in		$\Delta P_{\%}$ (8.9)	$\Delta\dot{E}_{\mathrm{WHR},1}$ (8.7), $\Delta\dot{E}_{\mathrm{fj},1}$ (8.14)	
$4_{\mathrm{CO_2}}$	flow-join1 out, WHR2 in, HTR in	ΔT_{pp} (8.17)	$= P_{\mathrm{CO_2},3}$	$\Delta\dot{E}_{\mathrm{WHR},2}$ (8.7), $\Delta\dot{E}_{\mathrm{fj},1}$ (8.14), $\Delta\dot{E}_{\mathrm{HTR}}$ (8.7), $\mathrm{Eff}_{\mathrm{HTR}}$ (8.19)	
$5_{\mathrm{CO_2}}$	WHR2 out, turb1 in		$\Delta P_{\%}$ (8.9)	$\eta_{\mathrm{turb},1}$ (8.3), $\Delta\dot{E}_{\mathrm{WHR},2}$ (8.7)	
$6_{\mathrm{CO_2},s}$	isentropic turb1 out		$= P_{\mathrm{CO_2},6}$	$\eta_{\mathrm{turb},1}$ (8.3)	$= s_{\mathrm{CO_2},5}$
$6_{\mathrm{CO_2}}$	turb1 out, HTR in		$\Delta P_{\%}$ (8.10)	$\eta_{\mathrm{turb},1}$ (8.3), $\Delta\dot{E}_{\mathrm{HTR}}$ (8.7), $\mathrm{Eff}_{\mathrm{HTR}}$ (8.19),	
$7_{\mathrm{CO_2}}$	HTR out, flow-join2 in		$= P_{\mathrm{CO_2},8}$	$\Delta\dot{E}_{\mathrm{HTR}}$ (8.7), $\mathrm{Eff}_{\mathrm{HTR}}$ (8.19), $\Delta\dot{E}_{\mathrm{fj},2}$ (8.14)	
$8_{\mathrm{CO_2}}$	flow-join2 out, LTR in		$\Delta P_{\%}$ (8.10)	$\Delta\dot{E}_{\mathrm{LTR}}$ (8.7), $\mathrm{Eff}_{\mathrm{LTR}}$ (8.19), $\Delta\dot{E}_{\mathrm{fj},2}$ (8.14)	
$9_{\mathrm{CO_2}}$	LTR out chiller in		$\Delta P_{\%}$ (8.10)	$\Delta\dot{E}_{\mathrm{LTR}}$ (8.7), $\mathrm{Eff}_{\mathrm{LTR}}$ (8.19)	
$10_{\mathrm{CO_2}}$	LTR out flow-join1 in		$= P_{\mathrm{CO_2},3}$	$\Delta\dot{E}_{\mathrm{LTR}}$ (8.7), $\mathrm{Eff}_{\mathrm{LTR}}$ (8.19), $\Delta\dot{E}_{\mathrm{fj},1}$ (8.14)	
$11_{\mathrm{CO_2}}$	HTR out turb2 in		$\Delta P_{\%}$ (8.9)	$\eta_{\mathrm{turb},2}$ (8.3), $\Delta\dot{E}_{\mathrm{HTR}}$ (8.7), $\mathrm{Eff}_{\mathrm{HTR}}$ (8.19)	
$12_{\mathrm{CO_2},s}$	isentropic turb2 out		$= P_{\mathrm{CO_2},12}$	$\eta_{\mathrm{turb},2}$ (8.3)	$= s_{\mathrm{CO_2},11}$
$12_{\mathrm{CO_2}}$	turb2 out flow-join2 in		$= P_{\mathrm{CO_2},8}$	$\eta_{\mathrm{turb},2}$ (8.3), $\Delta\dot{E}_{\mathrm{fj},2}$ (8.14)	

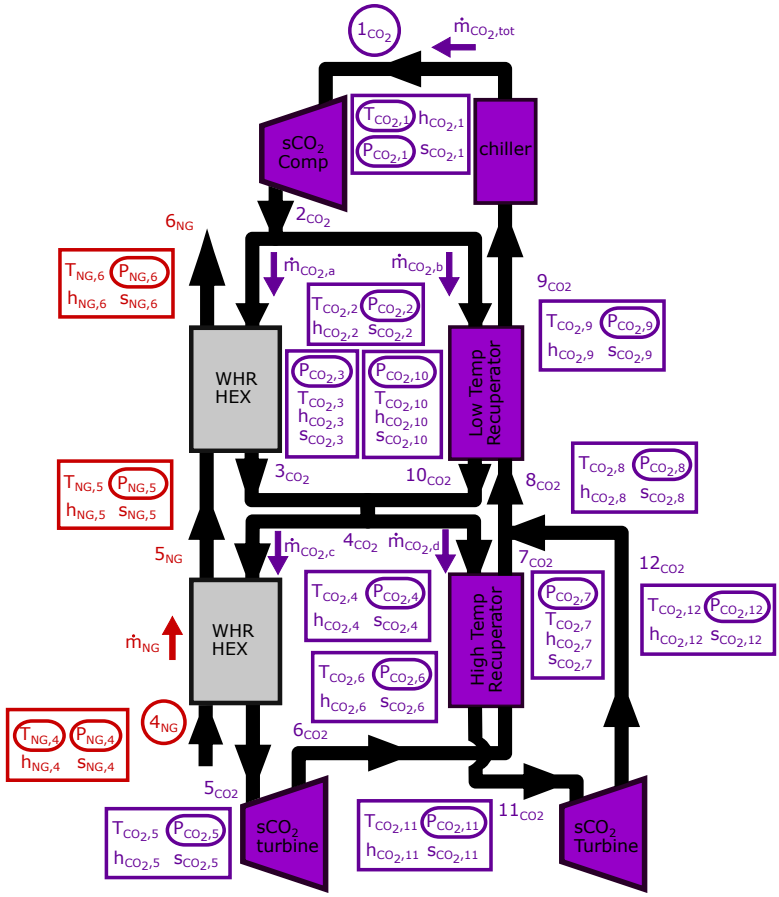

Figure 8.13: Dual recuperated sCO_2 Brayton cycle with split heating with state variables.

8.1.6 Power output and efficiency determination

With all thermodynamic states fully defined, the power output and efficiencies of each cycle and of the total power plant layout can be determined.

Net power output for a given cycle, $\dot{W}_{\text{cycle},net}$, is the balance of power generated by the turbines and power required by the compressors or pump:

$$\dot{W}_{\text{cycle},net} = \dot{W}_{\text{cycle},out} - \dot{W}_{\text{cycle},in}, \tag{8.23}$$

where the $\dot{W}_{\text{cycle},out}$ and $\dot{W}_{\text{cycle},in}$ are determined using equations 8.4 and 8.2.

Net electrical power output for a given cycle, $\dot{W}_{\text{cycle},net,el}$, is the balance of electrical power generated by the turbines and the electrical power required by the compressors or

pump:

$$\dot{W}_{\text{cycle},net,el} = \dot{W}_{\text{cycle},out,el} - \dot{W}_{\text{cycle},in,el}, \tag{8.24}$$

where the $\dot{W}_{\text{cycle},out,el}$ and $\dot{W}_{\text{cycle},in,el}$ are determined using equations 8.5 and 8.6.

Total net power output, $\dot{W}_{\text{tot},net}$, is the sum of the net power output of each cycle:

$$\dot{W}_{\text{tot},net} = \dot{W}_{\text{NG},net} + \dot{W}_{\text{CO}_2,net} + \dot{W}_{\text{H}_2\text{O},net}, \tag{8.25}$$

where the power output from a cycle not present in a given layout is zero.

Total net electrical power output, $\dot{W}_{\text{tot},net,el}$, is calculated in the same manner:

$$\dot{W}_{\text{tot},net,el} = \dot{W}_{\text{NG},net,el} + \dot{W}_{\text{CO}_2,net,el} + \dot{W}_{\text{H}_2\text{O},net,el}. \tag{8.26}$$

Thermal efficiency of a given cycle, $\eta_{\text{cycle},th}$, can be calculated by

$$\eta_{\text{cycle},th} = \frac{\dot{W}_{\text{cycle},net}}{\dot{Q}_{in}}. \tag{8.27}$$

In the case of the natural gas cycle, the heat transferred to the system, $\dot{Q}_{in}$, is the heat introduced in the combustion chambers. For sCO_2 and steam Rankine cycles, the waste heat transferred to the system, $\dot{Q}_{\text{WHR}}$ or $\dot{Q}_{\text{HRSG}}$, is used.

The cycle electrical efficiency, $\eta_{\text{cycle},el}$, is similarly calculated by

$$\eta_{\text{cycle},el} = \frac{\dot{W}_{\text{cycle},net,el}}{\dot{Q}_{in}}, \tag{8.28}$$

and the total thermal efficiency for the power plant layout, $\eta_{\text{tot},th}$, is calculated by

$$\eta_{\text{tot},th} = \frac{\dot{W}_{\text{tot},net}}{\dot{Q}_{in}}, \tag{8.29}$$

where $\dot{Q}_{in}$ is again the heat introduced in the combustion chamber.

Total electrical efficiency for the power plant layout, $\eta_{\text{tot},el}$, is similarly calculated by

$$\eta_{\text{tot},el} = \frac{\dot{W}_{\text{tot},net,el}}{\dot{Q}_{in}}. \tag{8.30}$$

8.1.7 Natural gas, steam, and sCO_2 cycle interaction and execution in EES

As discussed in the introduction of this chapter, each of the sCO_2 Brayton cycle configurations is evaluated both as a replacement to the steam Rankine cycle, and as an additional WHR cycle working in conjunction with a steam Rankine cycle. An EES script is accordingly written for each combination. The script for a given sCO_2 cycle layout calls the modules for each of the involved cycles, relays the results between them, and determines overall power plant efficiency and output.

Figure 8.14 represents all three plant layouts analyzed for each sCO_2 Brayton cycle, using a simple recuperated sCO_2 Brayton cycle as an example. The combinations are applied similarly to each sCO_2 Brayton cycle layout. A combined cycle with only an sCO_2 Brayton bottoming cycle is shown in 8.14a, while figure 8.14b shows a steam Rankine bottoming cycle subsequent to the sCO_2 cycle and 8.14c represents a layout with the waste heat in the exhaust gases being recovered first by a steam Rankine cycle and the remaining heat by an sCO_2 Brayton bottoming cycles.

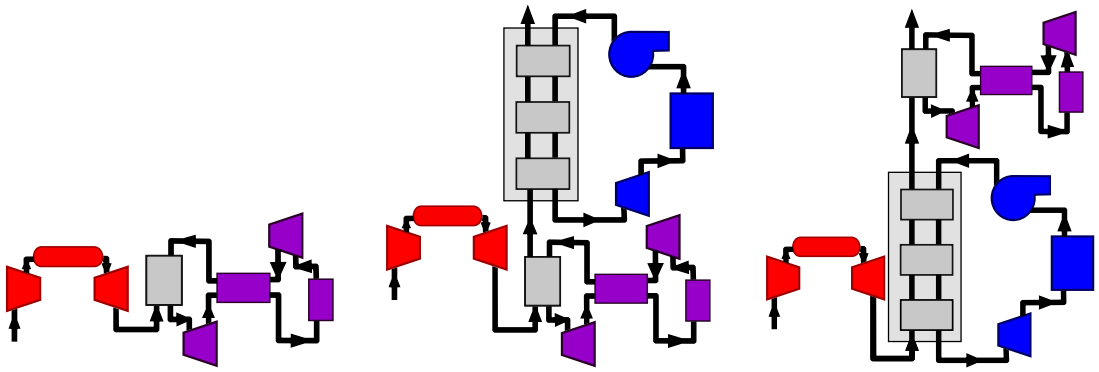

(a) NG $\rightarrow$ sCO_2. (b) NG $\rightarrow$ sCO_2 $\rightarrow$ H_2O. (c) NG $\rightarrow$ H_2O $\rightarrow$ sCO_2.

Figure 8.14: Plant configurations for each sCO_2 Brayton cycle layout.

8.2 Profitability Determination

As discussed in section 7.3, LCOE can be used to compare the profitability of the various power plant layouts. The most significant factors influencing the LCOE estimate, and especially in the difference between LCOE estimates for different power plant layouts, are the lifetime electrical energy production and project capital cost.

Lifetime electrical energy production, $W_{\text{el,lifetime}}$, is the product of the design total net electrical power output of the plant layout, expected lifetime of the plant, $t_{\text{plant life}}$, and an estimated plant utilization factor, f_{plant}:

$$W_{\text{el,lifetime}} = \dot{W}_{\text{tot},net,el} \cdot t_{\text{plant life}} \cdot f_{\text{plant}}. \tag{8.31}$$

Expected life is taken to be $t_{\text{plant life}} = 20$ years and the plant utilization factor is estimated at $f_{\text{plant}} = 0.85$ for each plant layout.

Project capital cost estimation is discussed in the following section, 8.2.1,and the remaining elements contributing to LCOE, along with a more specific discussion of LCOE estimation, are found in section 8.2.2.

8.2.1 Project capital cost estimation

The total capital costs of the natural gas cycles and steam Rankine cycles are estimated as a function of the design power output of the given cycle.

The cost function is estimated by applying the rule of thumb taken from Kehlhofer et al. [15] that each of the cycles comprising a traditional CCPP account for approximately half of the cost to the project cost data from the 2014-15 Gas Turbine World Handbook. [28] The project cost data is first adjusted for inflation from 2015$ to 2020$. The rule of thumb is then applied to estimate the cost of each cycle (with the cost of each being half the total project cost). This cost is then divided by the electrical power output of the individual cycles to determine specific cost on a per kW_e basis. These specific costs are then plotted

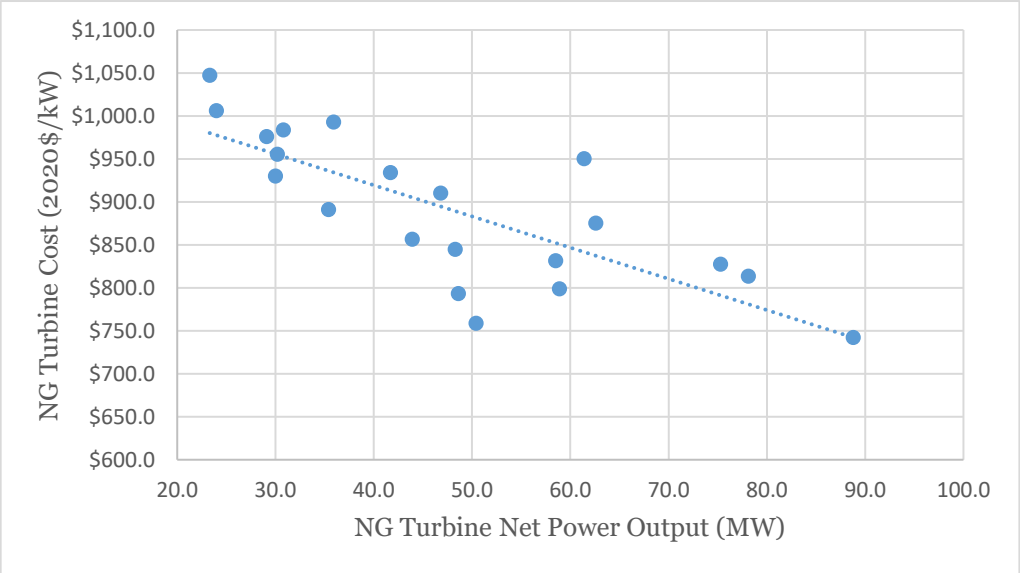

Figure 8.15: Natural gas cycle cost as a function of net cycle electrical power output as estimated from data in [28].

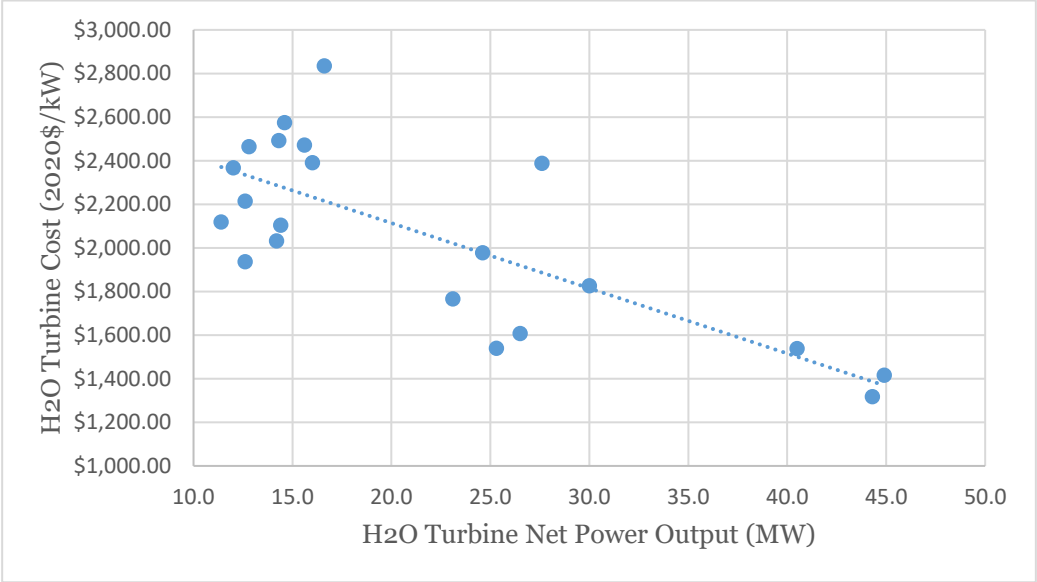

Figure 8.16: Steam Rankine cycle cost as a function of net cycle electrical power output as estimated from data in [28].

against the cycle electrical power output to determine how the cost scales with power plant size. The resulting plot for the natural gas cycle is shown in figure 8.15 and the resulting plot for the steam Rankine cycle is given in figure 8.16.

The trend is then approximated with a linear fit. The resulting linear equation for the

Table 8.14: Estimated sCO_2 component costs, adjusted from [29].

Component	specific cost
Recuperators	$2700\ [\frac{\$}{\mathrm{kW}_{th}/\mathrm{K}}]$
Primary WHR Heat Exchanger	$5300\ [\frac{\$}{\mathrm{kW}_{th}/\mathrm{K}}]$
Chiller	$1800\ [\frac{\$}{\mathrm{kW}_{th}/\mathrm{K}}]$
Other Components	$1100\ [\frac{\$}{\mathrm{kW}_{e}}]$

specific cost of the natural gas cycle is

$$\mathrm{cost}_{\mathrm{NG}} = 1065\frac{\$}{\mathrm{kW}} - 0.00363\frac{\$}{\mathrm{kW}^2}(\dot{W}_{\mathrm{NG},net,el}). \tag{8.32}$$

This results in a second order polynomial equation for the total cycle cost:

$$\mathrm{Cost}_{\mathrm{NG}} = 1065\frac{\$}{\mathrm{kW}}(\dot{W}_{\mathrm{NG},net,el}) - 0.00363\frac{\$}{\mathrm{kW}^2}(\dot{W}_{\mathrm{NG},net,el})^2. \tag{8.33}$$

The resulting linear equation for the specific cost of the steam Rankine cycle is

$$\mathrm{cost}_{\mathrm{H_2O}} = 2712\frac{\$}{\mathrm{kW}} - 0.0299\frac{\$}{\mathrm{kW}^2}(\dot{W}_{\mathrm{H_2O},net,el}), \tag{8.34}$$

which results in a second order polynomial equation for the total cycle cost:

$$\mathrm{Cost}_{\mathrm{H_2O}} = 2712\frac{\$}{\mathrm{kW}}(\dot{W}_{\mathrm{H_2O},net,el}) - 0.0299\frac{\$}{\mathrm{kW}^2}(\dot{W}_{\mathrm{H_2O},net,el})^2. \tag{8.35}$$

The total capital costs of the sCO_2 Brayton cycles are determined on a component basis. The assumed costs are taken directly from Wright et al, but are adjusted to 2020$. The values used are shown in table 8.14.

The procedure used by Wright et al. as described in section 7.3 is then used to determine sCO_2 cycle cost, yielding

$$\mathrm{Cost}_{\mathrm{HEX}} = \mathrm{cost}_{\mathrm{HEX}}(\frac{\dot{Q}_{\mathrm{HEX}}}{\mathrm{LMTD}_{\mathrm{HEX}}}) \tag{8.36}$$

for the cost of each heat exchanger, where cost_{HEX} is the specific cost according to the heat exchanger type from table 8.14, $\dot{Q}_{\text{HEX}}$ is the heat transferred in the heat exchanger, and LMTD_{HEX} is the log mean temperature difference between the warm and cold streams in the heat exchanger.

The cost of the turbomachinery, piping and all other elements of the cycle are estimated as the product of the net electrical power output and the specific cost estimated for the balance of plant (other Components in table 8.14), $\text{cost}_{\text{other}}$:

$$\text{Cost}_{\text{other}} = \text{cost}_{\text{other}}(\dot{W}_{\text{CO}_2,net,el}). \tag{8.37}$$

The total sCO_2 Brayton cost estimate is then the sum of the heat exchanger costs and other component costs:

$$\text{Cost}_{\text{sCO}_2} = \sum \text{Cost}_{\text{HEX}} + \text{Cost}_{\text{other}}. \tag{8.38}$$

Finally, the total project capital cost for a given power plant layout is the sum of the costs of the component power cycles

$$\text{Cost}_{\text{project}} = \text{Cost}_{\text{NG}} + \text{Cost}_{\text{H}_2\text{O}} + \text{Cost}_{\text{sCO}_2}. \tag{8.39}$$

8.2.2 LCOE calculation

The LCOE of the various power plant layouts are estimated following the general process outlined by Wright et al.[29]. Equation 7.2, repeated here as equation 8.40, is the formula used for the LCOE:

$$\text{LCOE} = \frac{\text{Cost}_{\text{project}} - \text{tax shield}_{\text{depreciation,PV}} + \text{Cost}_{\text{lifetime operation,PV}} - \text{Cost}_{\text{salvage,PV}}}{W_{\text{el,lifetime}}}. \tag{8.40}$$

The procedures for project capital cost and lifetime electrical energy production having

been described above, the determination of the remaining contributing factors are discussed here.

Salvage cost is simply assumed to be zero for every plant model.

The tax shield of depreciation is the product of the project capital cost and an assumed tax rate, r_{tax},:

$$\text{tax shield}_{\text{depreciation}} = \text{Cost}_{\text{project}} \cdot r_{tax}. \tag{8.41}$$

The tax rate is assumed to be $r_{tax} = 0.35$ for all plant layouts.

The cost of lifetime operation is modeled with an estimated fuel cost, $\text{Cost}_{\text{fuel,lifetime}}$, and a bulk estimation of other operation and maintenance costs, $\text{Cost}_{\text{O\&M,lifetime}}$:

$$\text{Cost}_{\text{lifetime operation}} = \text{Cost}_{\text{fuel,lifetime}} + \text{Cost}_{\text{O\&M,lifetime}}. \tag{8.42}$$

The fuel cost on a per energy basis is chosen to be 5 $\frac{\$}{\text{MBTU}}$ or roughly 4.74×10^{-6} $\frac{\$}{\text{kJ}}$. The total lifetime fuel cost is then the product of the specific fuel cost and the lifetime electrical energy production divided by the total plant electrical efficiency:

$$\text{Cost}_{\text{fuel,lifetime}} = \frac{\text{cost}_{\text{fuel}} \cdot W_{\text{el,lifetime}}}{\eta_{\text{cycle},tot,el}}. \tag{8.43}$$

Other operation and maintenance costs, $\text{cost}_{\text{O\&M}}$, are estimated to be $0.008\ ^{\$}/_{\text{kWh}}$, which, when multiplied by lifetime electrical production gives the lifetime operation and maintenance cost estimate:

$$\text{Cost}_{\text{O\&M,lifetime}} = \text{cost}_{\text{O\&M}} \cdot W_{\text{el,lifetime}}. \tag{8.44}$$

The project capital cost is an initial expense, but the depreciation tax shield and operation and salvage costs are incurred across the lifetime of the plant. In order to determine equivalent values, the present value of each of those sums which are distributed over the lifetime of the plant is determined using a ten year straight line depreciation schedule

(SLDS $= 10$) with a 0.02 discount rate ($r_d = 0.02$) such that, for some expected future quantity X_{lifetime}, the present value of that quantity, X_{PV},

$$X_{\text{PV}} = X_{\text{lifetime}} \cdot \frac{(1+r_d)^{\text{SLDS}} - 1}{\text{SLDS} \cdot r_d(1+r_d)^{\text{SLDS}}}. \tag{8.45}$$

LCOE and its contributing terms are calculated in an EES module which is called by the script for each plant layout model.

As is also discussed in section 7.3, the costs of a sCO_2 cycle-incorporating power plant are especially difficult to predict because the technology is still in research stages. The analysis in this work relies heavily on the process and assumptions of Wright et al [26] in their cost estimations for sCO_2 Brayton combined cycle power plants. Wright et al. estimate for example that their heat exchanger cost estimates have an uncertainty of $\pm 30\%$, and even -50%/+30% in the case of the primary WHR heat exchanger. Wright et. al's cost assumptions are for sCO_2 Brayton WHR bottoming cycles for a smaller scale natural gas power plant in the 10 - 30 MW_e power range, where the use of a steam Rankine cycle is impractical. Because the cost estimates used for the current work rely heavily on the figures provided by Wright et al., but are applied to power cycles in a higher power range, where steam Rankine bottoming cycles are typically used, the uncertainty can be expected to be considerably higher than in Wright et al's analysis.

The LCOE can then be used to compare the profitability of the various power plant layouts, so long as the high uncertainty is borne in mind. Reasonable shifts in any of the assumptions made have the potential to shift the relative LCOE significantly, but the estimation of LCOE can capture broad patterns of what can be expected from the various cycle layouts.

CHAPTER 9

RESULTS

9.1 Minimum LCOE Results

The minimum LCOE values resulting from each of the power plant layout models are displayed in table 9.1.

The first column indicates the sCO_2 Brayton cycle layout used in the given model plant layout. The second and third columns indicate the combination of bottoming cycles present in the particular plant layout model. The column with the header $\mathbf{1^{st}}$ indicates if a steam Rankine cycle or sCO_2 Brayton cycle is the initial bottoming cycle to which the exhaust gas transfers heat directly after the natural gas turbine outlet. The column with the header $\mathbf{2^{nd}}$ indicates which, if any, cycle subsequently recovers additional waste heat from the exhaust gas further downstream. The minimum resulting LCOE of all the parameter combinations sampled is displayed in the fourth column. The remaining columns detail the parameter values that resulted in the given LCOE value.

For certain plant layout models, none of the parameter combinations sampled resulted in valid results. In these cases, the LCOE and parameter cells are marked with a dash. For some of these models parameter values that would have given valid results may lay outside of the range tested. For others only a very narrow range of parameter values would have given valid results and this narrow range may have fallen entirely between the values sampled.

The lowest minimum LCOE estimate, 0.0276 \$/kWh, is provided by he plant layout employing the steam Rankine cycle as the primary bottoming cycle with a secondary simple sCO_2 Brayton bottoming cycle. This falls slightly below the LCOE estimate for a traditional CCPP, 0.0292 \$/kWh. The LCOE estimates for all other sCO_2 plant layouts are

Table 9.1: Minimum LCOE results for each plant layout

CO_2 cycle	WHR Cycles		LCOE	Corresponding Parameter Values					
	1^{st}	2^{nd}	$\left[\frac{\$}{kWh}\right]$	$T_{NG,t,in}$ [K]	CR_{NG}	$P_{CO_2,Hi}$ [kPa]	CR_{H_2O}	y_1	y_2
None (TCCPP)	H_2O		0.0292	1800	15		3000		
Simple	sCO_2		0.0419	1800	15	32000			
	sCO_2	H_2O	-	-	-	-	-		
	H_2O	sCO_2	0.0276	1800	20	16000	2200		
Simple Rec.	sCO_2		0.0393	1800	20	32000			
	sCO_2	H_2O	0.0387	1800	10	16000	3400		
	H_2O	sCO_2	0.0362	1800	30	16000	3400		
Dual Rec.	sCO_2		0.0376	1800	15	32000		0.5	
	sCO_2	H_2O	0.0437	1800	10	24000	2000	0.5	
	H_2O	sCO_2	0.0394	1600	30	16000	2200	0.9	
Recomp	sCO_2		-	-	-	-		-	
	sCO_2	H_2O	-	-	-	-	-	-	
	H_2O	sCO_2	-	-	-	-	-	-	
Dual Rec. w/ split heat	sCO_2		-	-	-	-		-	-
	sCO_2	H_2O	-	-	-	-	-	-	-
	H_2O	sCO_2	-	-	-	-	-	-	-

greater than the LCOE of the traditional CCPP. These differences potentially fall within the margin of error.

9.2 Plant Layouts Thermodynamic Results

Figures 9.1 through 9.4 represent the thermodynamic states found to result in the lowest LCOE estimate for a given plant layout in the form of Temperature-entropy (Ts) diagrams. The natural gas cycles are represented in red, steam Rankine cycles are represented in blue, and the sCO_2 Brayton cycles are represented in purple. Cycles are ordered from left to right according to the order of the cycles in the given plant layout. The same scale is applied to all Ts diagrams for a given working fluid to allow for easy visual comparison.

Figure 9.1 represents the traditional CCPP, figure 9.2 shows CCPPs using a simple sCO_2 bottoming cycle, figure 9.3 shows those using a simple recuperated sCO_2 bottoming cycle, and figure 9.4 represents those using a dual recuperated sCO_2 bottoming cycle.

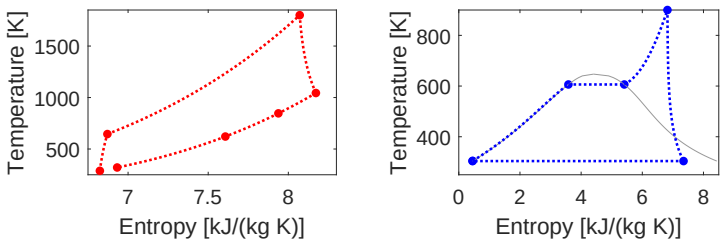

Figure 9.1: Traditional CCPP Ts diagrams

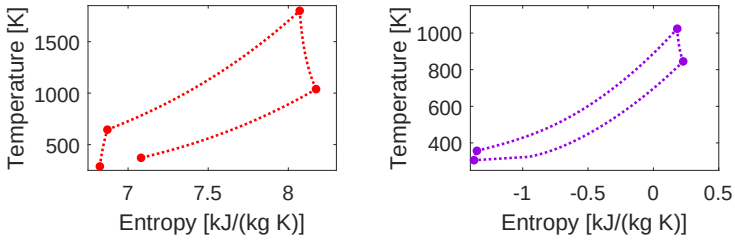

(a) NG $\rightarrow$ sCO_2

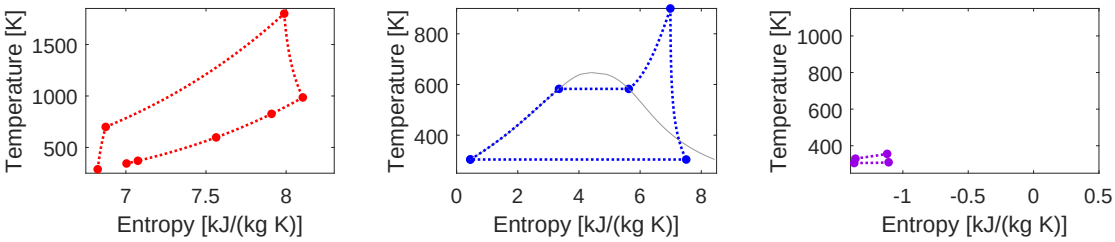

(b) NG $\rightarrow$ H_2O $\rightarrow$ sCO_2

Figure 9.2: simple sCO_2 Brayton cycle plant layout Ts diagrams

In several of the natural gas cycles there is a large gap in temperature between the exhaust gas outlet and the ambient intake temperature. Notably, in the case of the natural gas cycle topping a lone simple recuperated sCO_2 cycle (figure 9.3), there is a temperature difference of 403.3 °C and for the natural gas cycle topping a dual recuperated sCO_2 cycle and subsequent steam Rankine cycle (figure 9.4) there is a temperature difference of 295 °C between the exhaust outlet and ambient, with a temperature difference of only 16.5 °C across the HRSG. This is accomplished with a minuscule water flow of 1.41 kg/s compared to 175 kg/s of exhaust gas. In these cases a great deal of waste heat goes unrecovered; in the case with the single simple recuperated bottoming cycle, an additional 72.8 MW could theoretically be recovered if the exhaust gas were cooled all the way to ambient conditions.

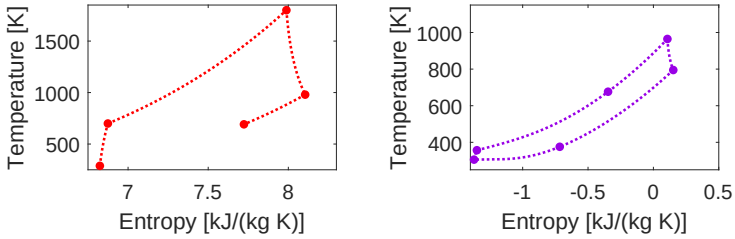

(a) NG $\rightarrow$ sCO_2

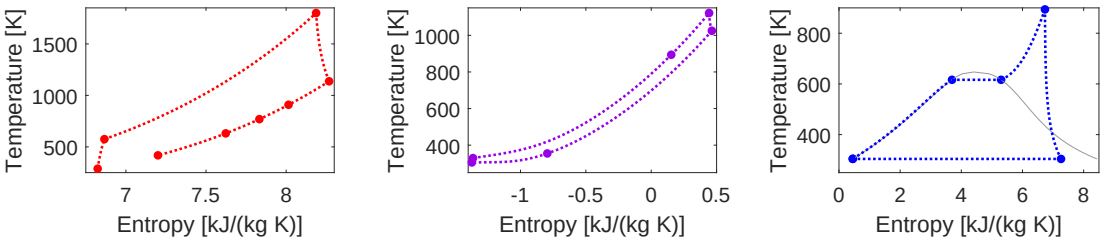

(b) NG $\rightarrow$ sCO_2 $\rightarrow$ H_2O

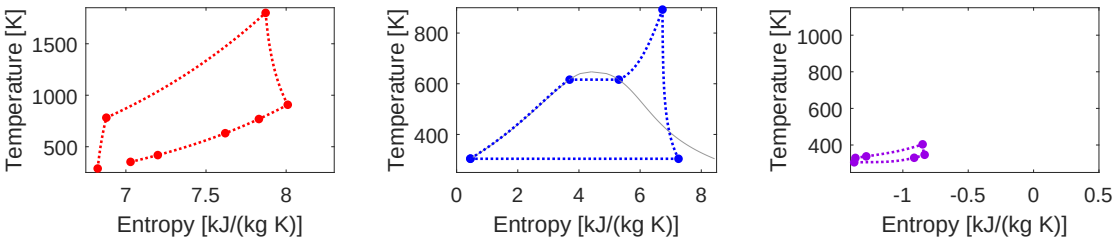

(c) NG $\rightarrow$ H_2O $\rightarrow$ sCO_2

Figure 9.3: simple recuperated sCO_2 Brayton cycle plant layout Ts diagrams

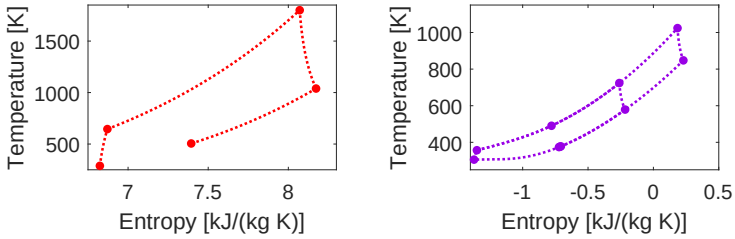

(a) NG $\rightarrow$ sCO_2

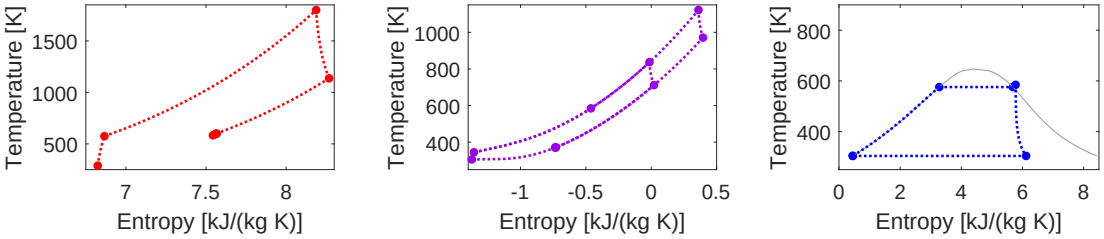

(b) NG $\rightarrow$ sCO_2 $\rightarrow$ H_2O

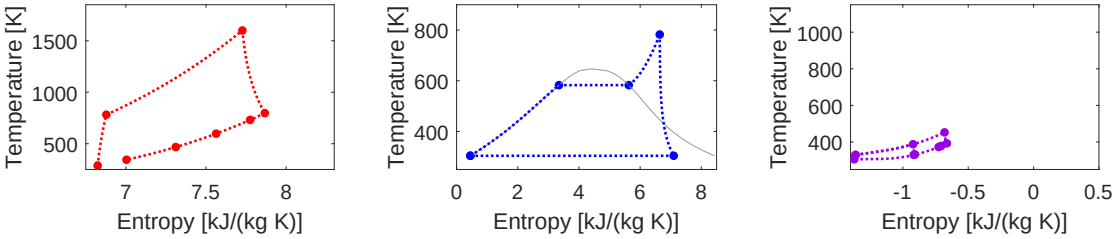

(c) NG $\rightarrow$ H_2O $\rightarrow$ sCO_2

Figure 9.4: dual recuperated sCO_2 Brayton cycle plant layout Ts diagrams

Figures 9.5 through 9.13 provide a visualization of the relationship between LCOE, plant total electrical efficiency and plant specific work as well as the effect of each parameter on those values.

The first column of plots in each figure is populated with the total plant electrical efficiency versus plant specific work resulting from every valid combination of parameters tested. The second column plots LCOE versus efficiency and the third LCOE vs specific work. The same axis limits are used for each of these values in every plot to allow for easy comparison. In the first row, all points are shown in the same shade of blue to outline the entire range of conditions tested. Subsequent rows show the same values plotted but are colored according to the value of a given parameter resulting in the values on the plot, with color brightness increasing with the parameter. The legends to the left indicate which values correspond to which shades. Natural gas turbine inlet temperature is indicated with red, natural gas compression ratio with yellow, CO_2 high pressure with purple, H_2O compression ratio with blue and mass flow split fraction with green.

In each case, the effect of natural gas turbine inlet temperature is most readily apparent. Increasing temperature is strongly correlated with both higher plant specific work and lower LCOE. The outcomes of the other parameters show a greater level of interdependence and dependence on the plant layout.

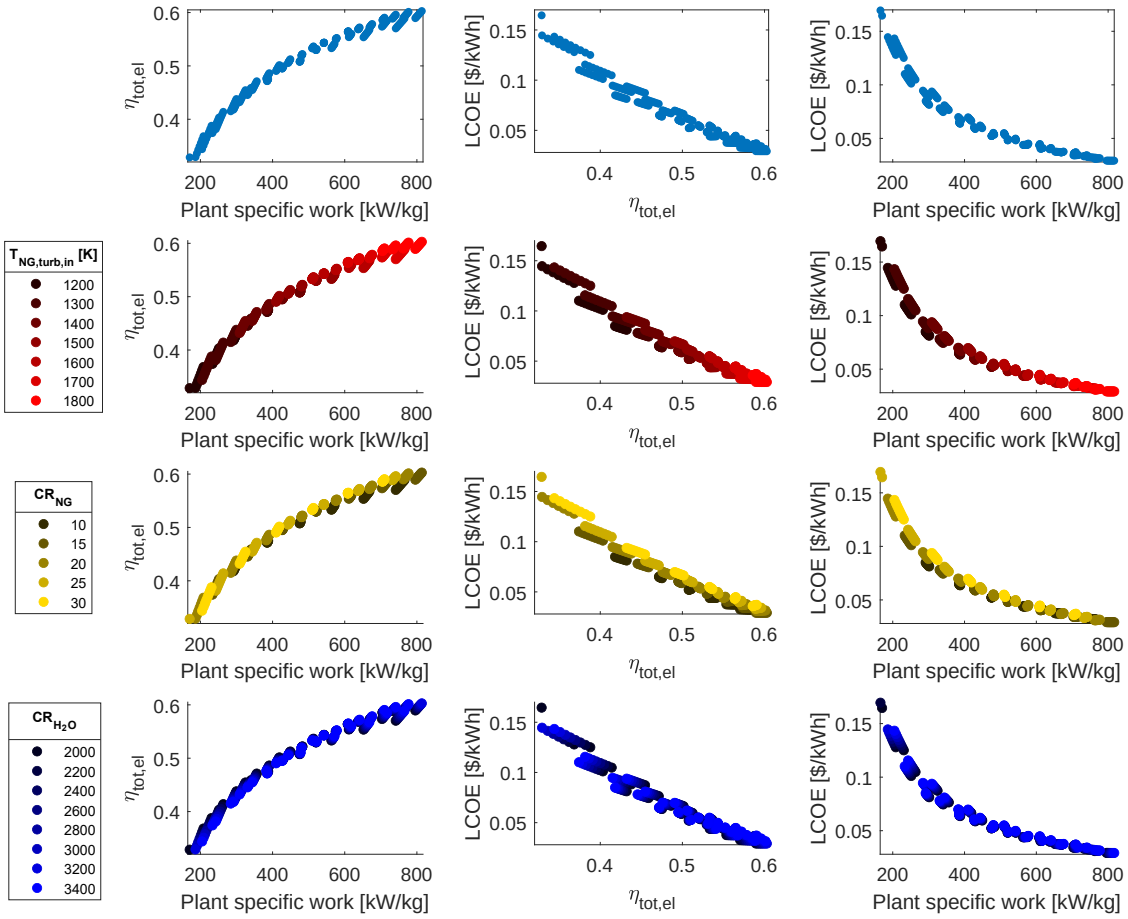

Figure 9.5: TCCPP parameter effects

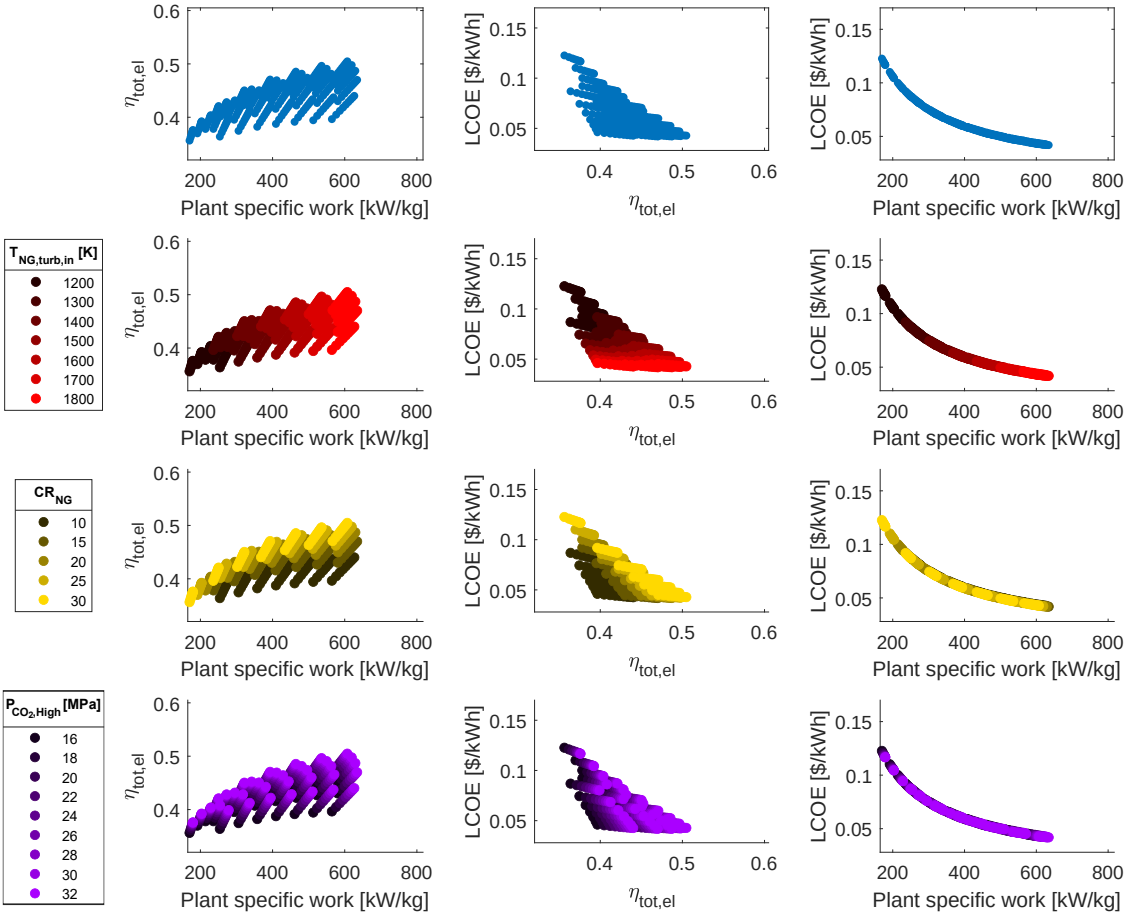

Figure 9.6: **NG → simple sCO$_2$** layout parameter effects

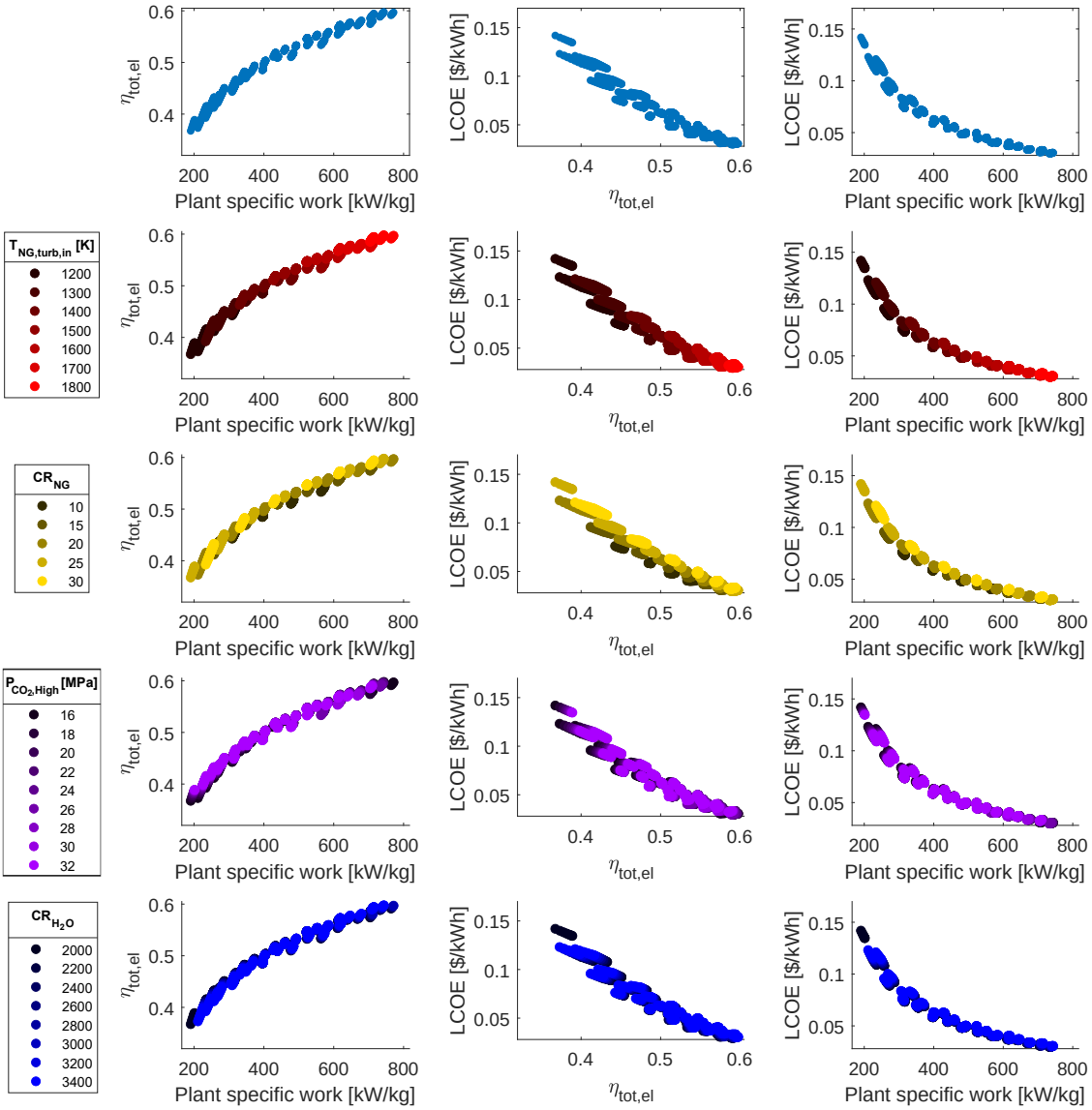

Figure 9.7: **NG → H_2O → simple sCO_2** layout parameter effects

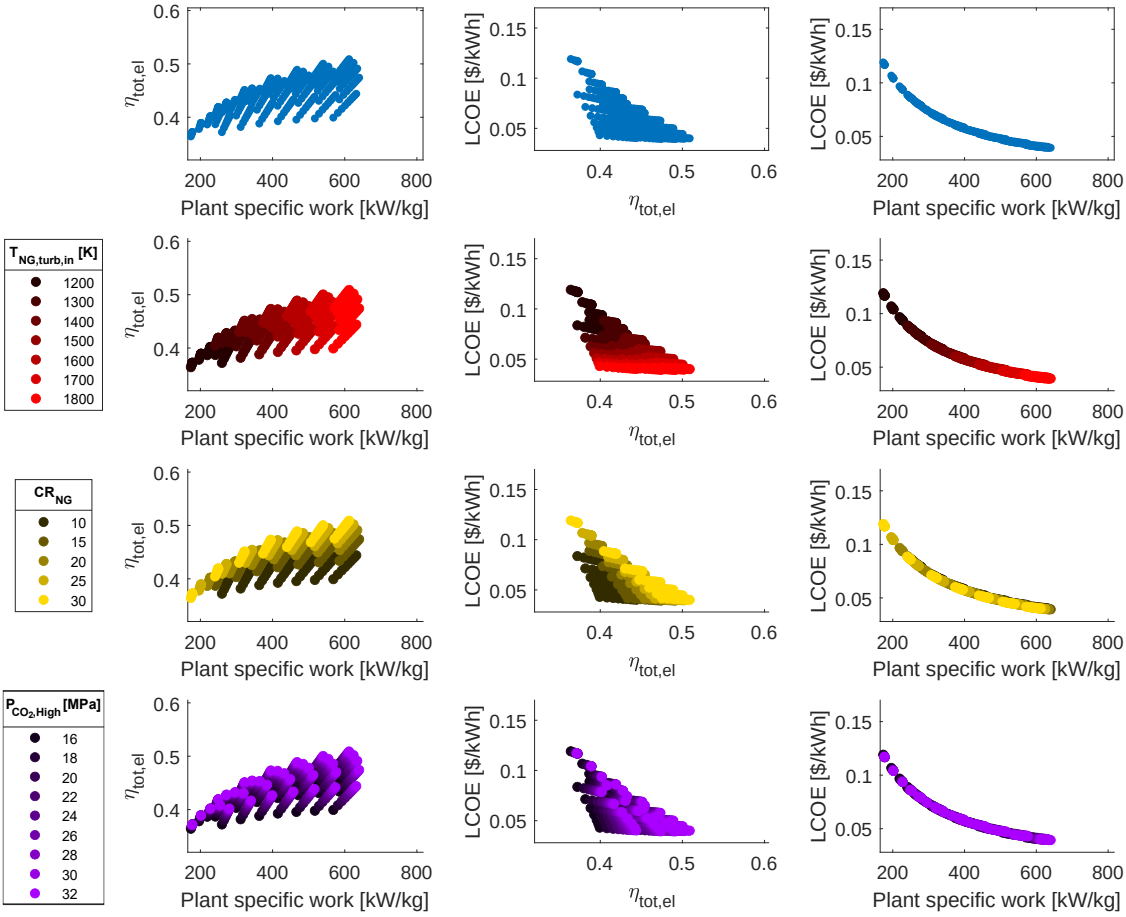

Figure 9.8: **NG → simple recuperated sCO_2** layout parameter effects

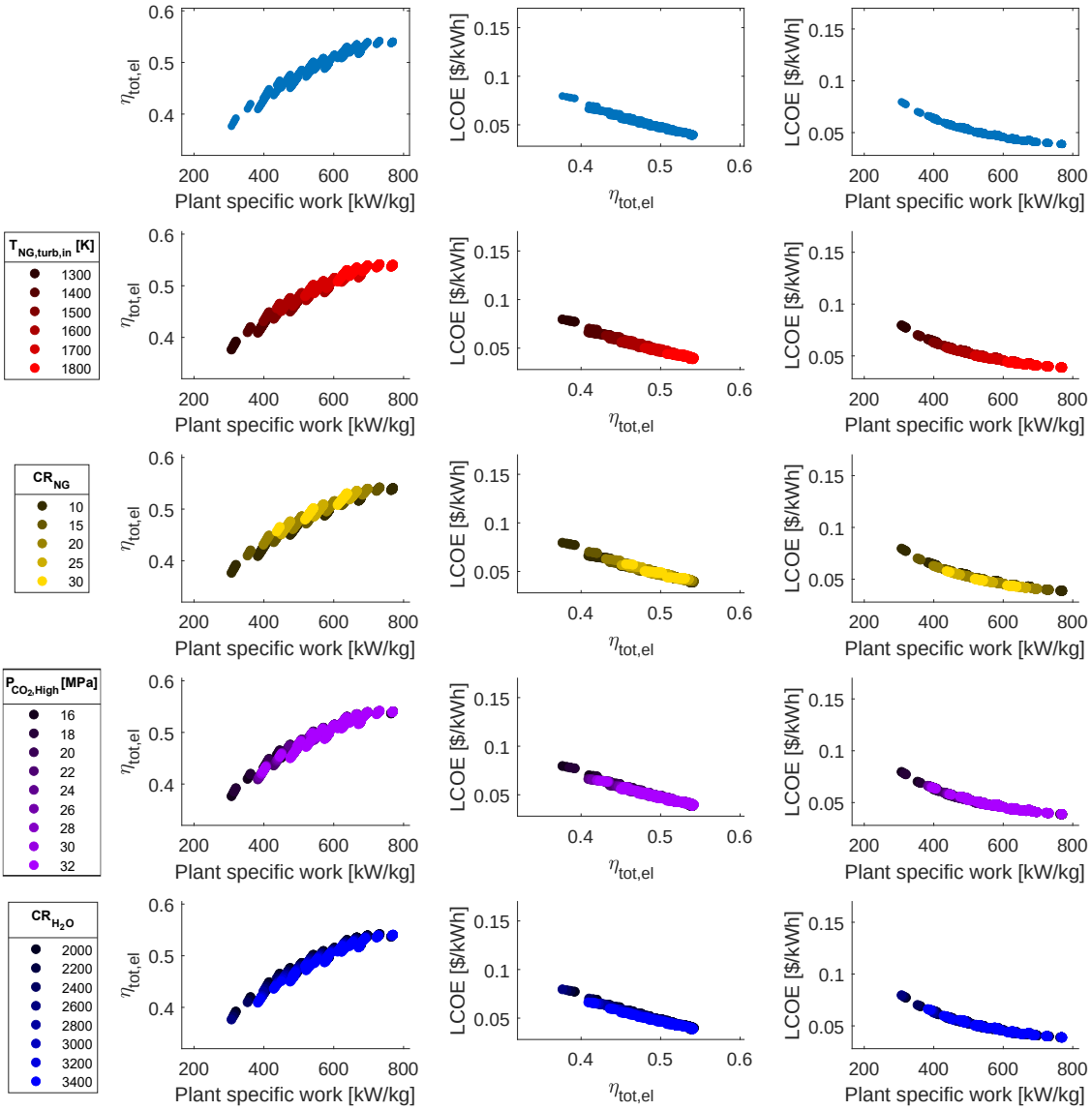

Figure 9.9: **NG → simple recuperated sCO_2 → H_2O** layout parameter effects

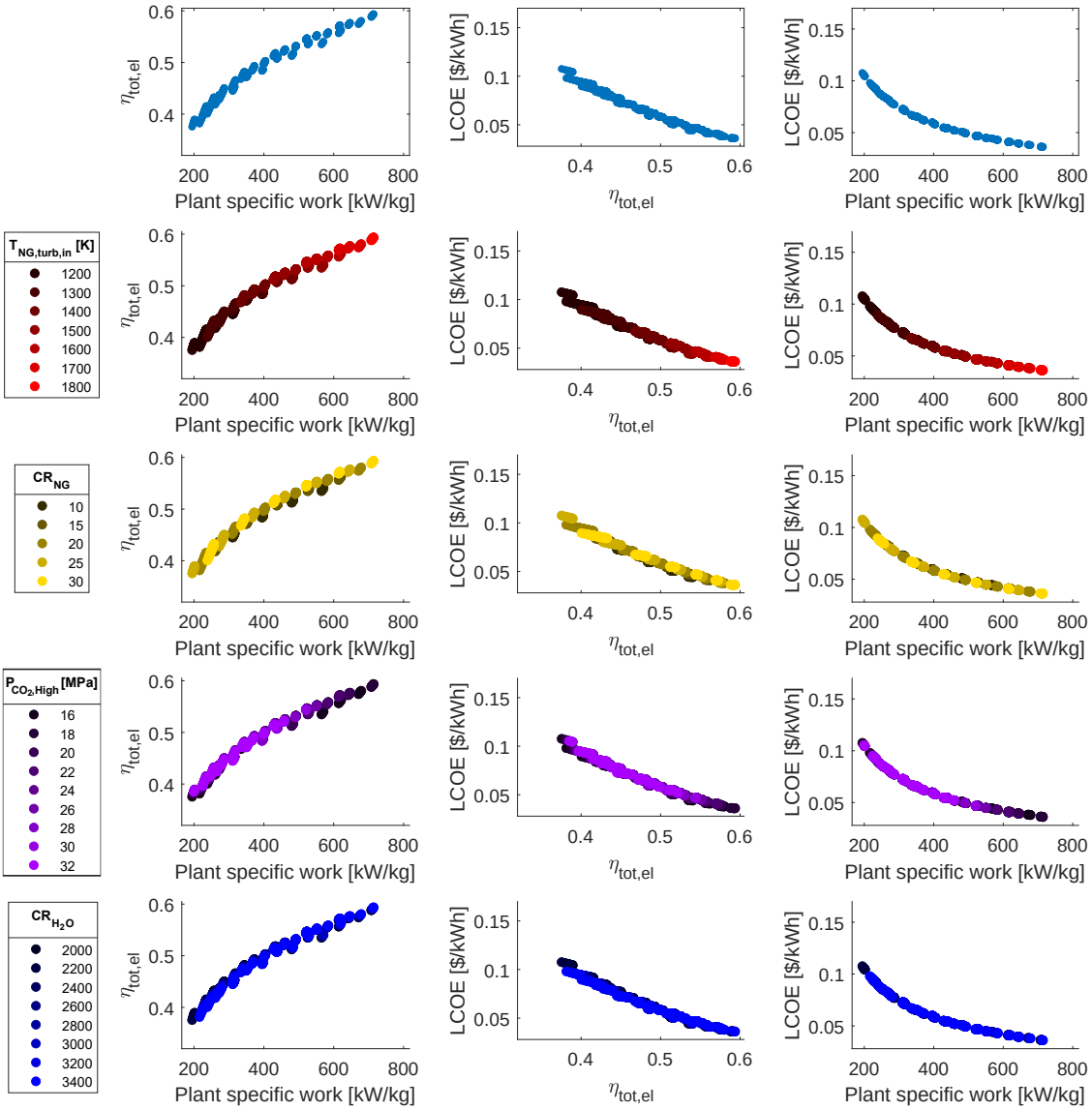

Figure 9.10: **NG → H_2O → simple recuperated sCO_2** layout parameter effects

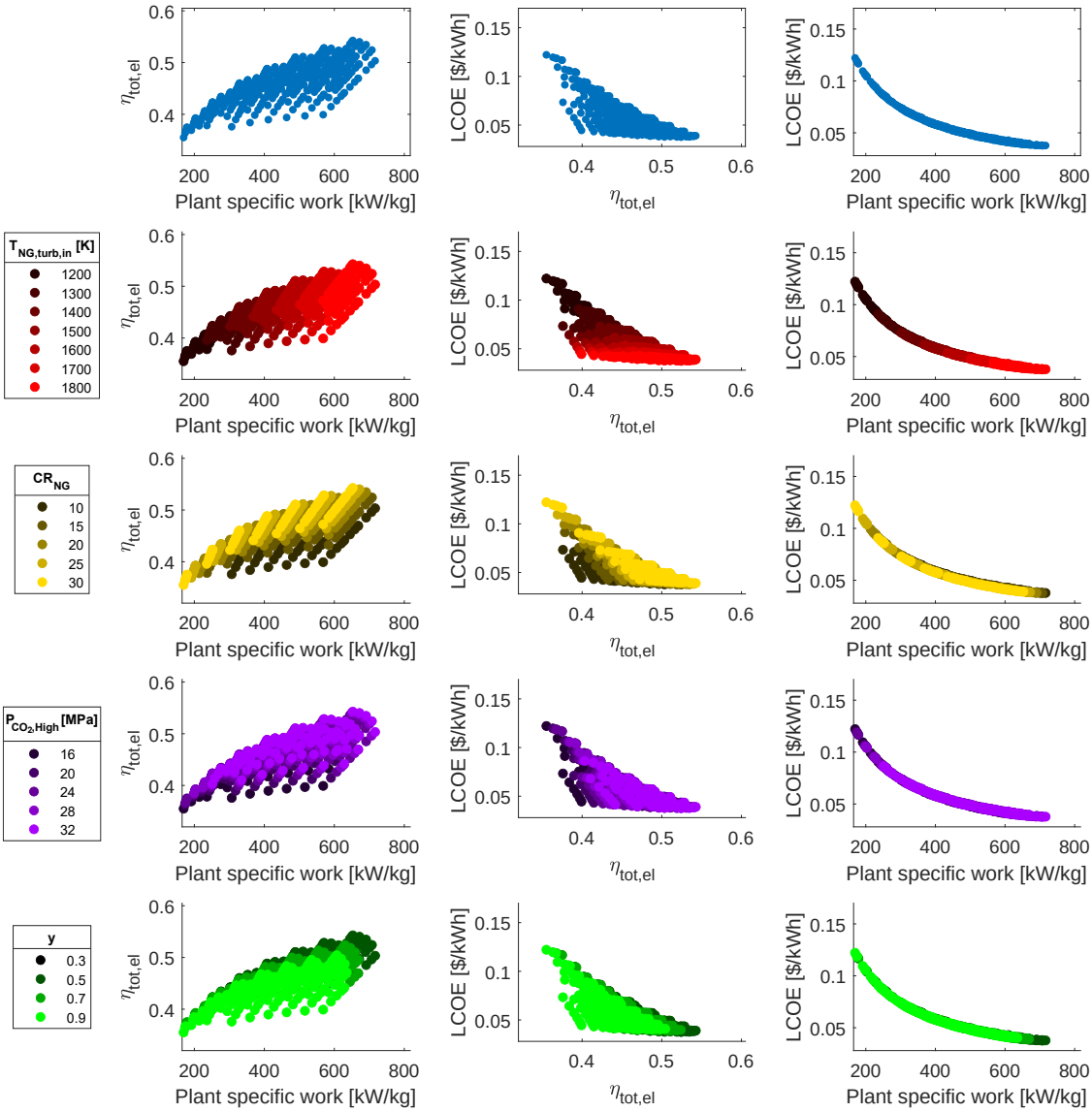

Figure 9.11: **NG → dual recuperated sCO$_2$** layout parameter effects

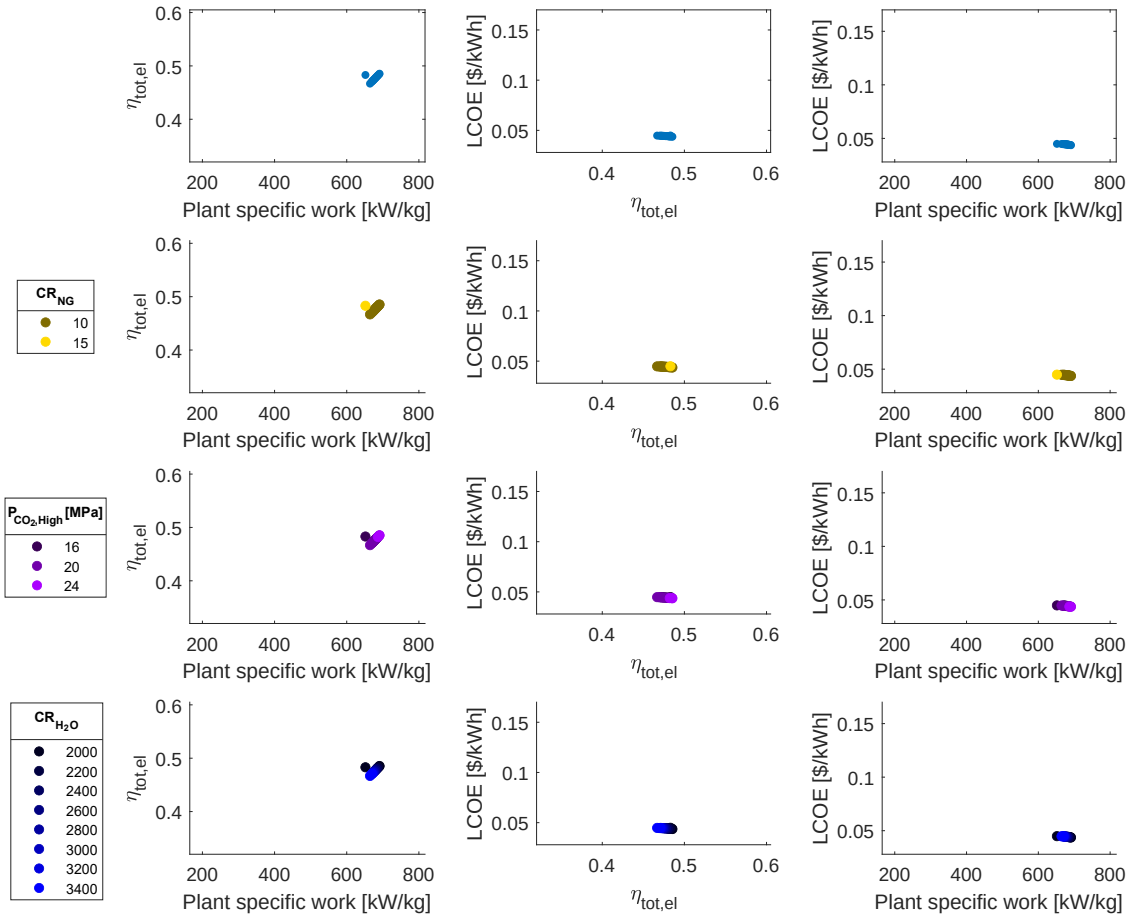

Figure 9.12: **NG → dual recuperated sCO_2 → H_2O** layout parameter effects

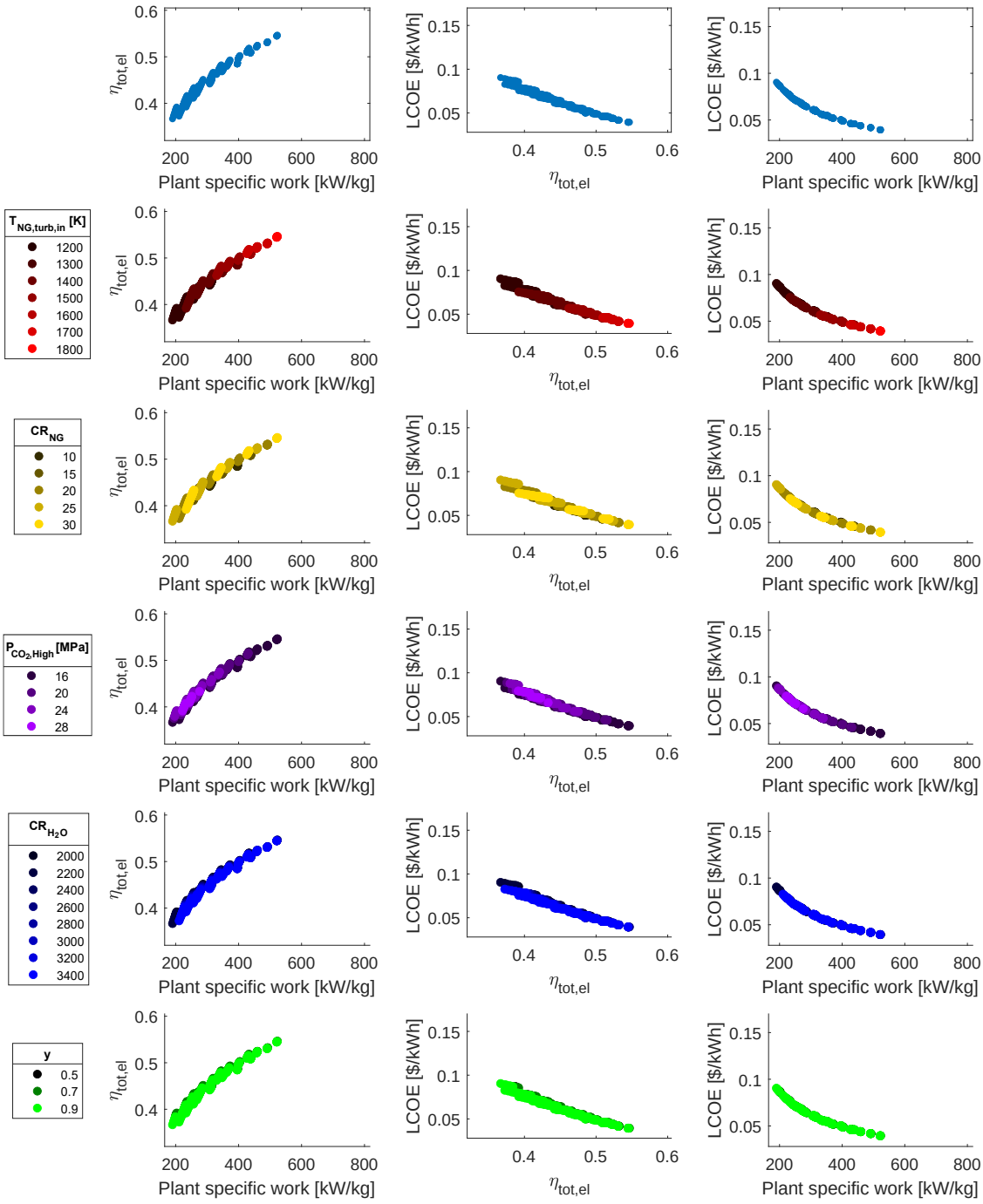

Figure 9.13: **NG → H_2O → dual recuperated sCO_2** layout parameter effects

CHAPTER 10
DISCUSSION AND CONCLUSION

10.1 Potential Implications of Results

The result of the models that the addition of a small simple sCO_2 Brayton cycle would result in a lower LCOE and therefore higher profits compared to a traditional combined cycle power plant is encouraging. Possibilities such as the incorporation of a WHR heat exchanger for a small sCO_2 cycle into the HRSG of new combined cycle power plant or even the addition of a small sCO_2 cycle to currently active combined cycle power plants seem worthy of investigation. Even the profitable replacement of a steam Rankine cycle with an sCO_2 cycle remains in the realm of possibility, though the estimated LCOEs of such plants are higher than those of traditional combined cycle power plants.

Unfortunately the limitations of this analysis warrant caution in assigning too much significance to any implications of the results.

10.2 Limitations

There are consequential limitations in both cost estimation and thermodynamic analysis of this work.

One limitations to this work are the large uncertainties associated with the cost estimates. High uncertainty is inherent in cost estimations of a new technology, and a thorough itemized investigation of other comparable technologies was beyond the scope of this project. As sCO_2 power cycle technology advances, more cost information will become available and more accurate estimates will be possible.

The fixed values and constraints chosen for the thermodynamic models represent only a subset of what could be possible. The results illuminate some flaws in the constraints and

parameters used in the thermodynamic models. The high quantities of lost exhaust heat in the results of several models indicate that the plant operating conditions defined by the given constraints and parameter values are not the most effective and do not reflect realistic conditions. The constraints on the waste heat recovery heat exchangers seem to play the greatest role in this. Because the constraints used in the model define heat exchanger performance on the temperature difference between fluids at both the inlet and outlet, those conditions are in many cases fulfilled at the expense of plant efficiency. In the cases where a steam Rankine cycle is used as a secondary bottoming cycle, the range of pressures tested through the water compression ratio parameter, CR_{H_2O}, limit the potential of these bottoming cycles. The lowest pressures tested are still so high that the saturation temperature at the evaporator inlet is too high to allow for significant heat transfer through the HRSG. The range of pressures investigated was chosen to match those in traditional combined cycle power plants, for which a lower pressure range would be disadvantageous, but for plant layouts using a steam Rankine cycle as a secondary bottoming cycle, a relatively lower pressure range would be needed to foster heat transfer.

The thermodynamic models are simplifications of the power cycles employed in actual power plants and offer no information on transient or off-design conditions. More complex thermodynamic modeling would yield more accurate information. The steam Rankine cycle, for instance, is modeled as a simple Rankine cycle with superheating, whereas a typical steam Rankine cycle in an operating combined cycle power plant will often have two or three pressure levels and reheat.

10.3 Future Work

The most immediately warranted work is the continuation of this investigation with improved thermodynamic model constraints. An adjustment of these values and constraints could potentially lead to more profitable or more realistic representations of possible power plant operating conditions. Exhaust gas outlet temperature could for instance be fixed rather

than temperature differences at the heat exchanger inlets and outlets to define a subset of operating conditions that better ensure potential to recover a greater percentage of waste heat. The lower limit of the range of water compression ratio could also be lowered for the same reason. A higher quantity of parameter values could be tested within the given ranges.

The plant layouts that show promise based on these results, such as the combined cycle power plant with a natural gas cycle with a steam Rankine and subsequent simple recuperated sCO_2 Brayton bottoming cycle, could be more closely investigated. Transient and off-design conditions, as well as simply a broader range of operating conditions could be analyzed.

Pricing information availability will increase as sCO_2 power cycles are developed, but plant cost can already be investigated at a greater depth than was possible in this work. Future projects could take a closer look at the pricing of similar technologies and develop better cost estimates from them.

10.4 Conclusion

Although the weaknesses of this work limit the conclusions that can be drawn, the results from the models indicate that the incorporation of sCO_2 Brayton cycles into combined cycle power plants has the potential for profitability and warrants further investigation.

For the subset of operating conditions tested, one configuration provides a lower cost of electricity that the traditional combined cycle power plant. The other layouts tested, while estimated to be more costly, were near enough in range that a profitable application is still indicated to be plausible. With constraints that better tailor plant operating conditions general trends of comparable profitability could be identified with greater certainty.

As sCO_2 power cycles are developed commercially, the costs can be expected to drop, so it is likely that combined cycle power plants incorporating them will become more economically viable with time.

Appendices

APPENDIX A

DATA SHEETS

A.1 InfraTec ImageIR 8300 hp S

2.3 Technical Data

Model ImageIR®	5300	5800	8300	8300 hp
Spectral range	(2 ... 5.7) µm	(8 ... 9.3) µm	(2.0 ... 5.7) µm	(2.0 ... 5.7) µm
Pitch	30 µm	30 µm	15 µm	15 µm
Detector	MCT or InSb	MCT or QWIP	MCT or InSb	MCT or InSb
Detector format (IR pixels)	(320 × 256)	(320 × 256)	(640 × 512)	(640 × 512)
Image acquisition	Snapshot			
Selection mode	ITR	ITR	ITR / IWR*	ITR / IWR*
Aperture ratio	f/3.0 or f/2.0	f/2.0	f/3.0 or f/2.0	f/3.0 or f/2.0
Detector cooling	Stirling cooler			
Temperature measuring range	(-40 ... 1,500) °C (up to 3,000 °C)*	(-40 ... 600) °C (up to 1,500 °C)*	(-40 ... 1,500) °C (up to 3,000 °C)*	(-40 ... 1,500) °C (up to 3,000 °C)*
Measurement accuracy	± 1 °C or ± 1 % of reading			
Temperature resolution @ 30 °C	0.015 K (15 mK)	0.025 K (25 mK)	Better than 0.02 K (20 mK)	Better than 0.02 K (20 mK)
Frame rate (full frame / half frame / quarter frame / sub-frame)	Up to 450 / 1,500 / 4,500 / 25,000 Hz	Up to 250 / 900 / 4,500 / 10,000 Hz	Up to 151 / 540 / 1,520 / 2,807 Hz	InSb up to 355 / 670 / 1,200 / 5,000 Hz MCT up to 232 / 828 / 2,300 / 3,725 Hz
Focus	Manually, motorised or automatically*			
Dynamic range	Up to 16 bit	14 bit	Up to 16 bit	Up to 16 bit
Integration time	(1 … 20,000) µs in increments of 1 µs	(1 … 20,000) µs in increments of 1 µs	(0.6 … 20,000) µs in increments of 1 µs	(0.6 … 20,000) µs in increments of 1 µs
Rotating filter wheel*	Up to 5 positions	Up to 5 positions	Up to 5 positions	Up to 5 positions
Rotating aperture wheel*	Up to 5 positions	No	Up to 5 positions	Up to 5 positions
Multi integration time*	Yes			
Interfaces	GigE, CamLink*, USB	GigE, CamLink*, USB	GigE, CamLink*, USB	GigE, 10 GigE*, USB, 2 x CamLink*, HDMI*
Trigger*	2 IN / 2 OUT, TTL	2 IN / 2 OUT, TTL	2 IN / 2 OUT, TTL	2 IN / 2 OUT, TTL
Analog signals*, IRIG-B*	1 IN, no	1 IN, yes	1 IN / 2 OUT, yes	1 IN / 2 OUT, yes
Tripod adapter	1/4" and 3/8" photo thread, 2x M5			
Power supply	24 VDC, wide-range power supply (100 – 240) V AC			
Storage temperature	(-40 ... 70) °C			
Ambient temperature in operation	Camera (-20 … 50) °C Power supply (0 … 50) °C			
Protection degree	IP54, IEC 60529			
Shock / vibration operational	2 G, IEC 60068-2-27/6			
Dimensions	(244 x 120 x 160) mm	(244 x 123 x 160) mm	(250 x 120 x 160) mm	(244 x 120 x 160) mm
Mass without lens	3.3 kg	3.5 kg	3.3 kg	3.3 kg

Tab. 1: Technical data of the ImageIR® camera series 5300 / 5800 / 8300 / 8300 hp

A.2 Nextel Velvet-Coating

MANKIEWICZ
Coating Concepts of the Future

NEXTEL® Velvet-Coating 811-21 Technical Datasheet 811-21

Characteristics

- Special black topcoat used to create matte and completely anti-glare surfaces
- Diffuse scattering of 98 % of the irradiated light - irrespective of the angle of incidence
- Specific technological stability
- Features good resistance to condensate and temperature stability
- High resistance to shock and impact

Range of Application

- For application to surfaces whenever light reflection is to be avoided, e.g. instrument scales, optical instruments and scientific equipment

Color and Gloss

Color: jet black
Gloss: dull matte

reflectance value ≤ 2/85° (DIN 67530 / ISO 2813)

Theoretical Coverage

Area	Quantity	Film thickness
436 m²	1 l	1 µm

Recommended dry film thickness: 45 - 55 µm

Surface Pre-treatment

- Is applied directly onto the appropriately cleaned / pre-treated substrate, e.g. metal substrates, thermoplastics and duroplasts.
- The use of NEXTEL Primer 5523 ist advisable on difficult surfaces, such as aluminium, and to improve adhesion, mechanical resistance and corrosion protection.

Trade Names and Packaging

Material	Trade name	Container size [net]
Base material	NEXTEL Velvet-Coating 811-21	1 l, 10 l
Thinner	NEXTEL Verdünner 8061	1 l, 5 l, 25 l

Mankiewicz Gebr. & Co. (GmbH & Co. KG)
Georg-Wilhelm-Str. 189
21107 Hamburg, Germany
Tel. +49 (40) 751030
Fax +49 (40) 75103510

MANKIEWICZ Coating Concepts of the Future
www.mankiewicz.com

Revision: 2
Date of Issue: 2017-03-23
Page: 1/2

Mixing

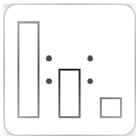

Material is delivered ready for use.

Pot Life

Without restriction within the scope of application of single-component systems.

Application

	Compressed air spraying
Addition of thinner	approx. 5 %
Efflux time (DIN 53211-4)	nicht measurable
Nozzle size	1.5 - 1.8 mm
Spraying pressure	approx. 3.0 bar

Please review the technical recommendations of the equipment manufacturers.

Drying

	20 °C drying	80 °C drying	120 °C drying
Flash-off time at 20 °C	-	30 min	30 min
Dust-dry	15 -20 min	-	-
Assembly-dry	approx. 6 h	60 min	30 min

The temperature specified is the object temperature.

Mankiewicz Gebr. & Co. (GmbH & Co. KG)
Georg-Wilhelm-Str. 189
21107 Hamburg, Germany
Tel. +49 (40) 751030
Fax +49 (40) 75103510

A.3 Chalk Spray

E-COLL

Kreidespray

Produktbeschreibung:	•	E-Coll Kreidespray hinterlässt eine gut sichtbare Markierung, die nach einigen Tagen durch den Wettereinfluß von selbst wieder verschwindet.
Anwendungsbeispiele:	•	E-Coll Kreidespray ist besonders geeignet für kurzfristig ange-brachte Baustellenmarkierungen, Sportevents (Golf, Marathon, Fußball, etc.) und Werbeaktionen.
	•	Markierung auf jeder Oberfläche möglich, sogar auf Erde und Gras. Sehr kurze Trocknungszeit.
Verarbeitung:	•	Dose kräftig schütteln, bis sich die Mischkugeln frei bewegen, während des Sprühvorganges mehrmals wiederholen.
	•	Nicht zu besprühende Flächen gut abdecken.
	•	Idealtemperatur: 20°C, Sprühdose 25 - 30 cm vom Gegenstand entfernt halten
	•	und Sprühkopf ganz hineindrücken.
	•	Die Überkopfsprühdüse gewährleistet eine einfache und praktische Arbeitsweise auf Bodenflächen, da es nicht zu Materialverlusten durch einen falschen Neigungswinkel (Bügelbrettverfahren) kommt.
	•	Die ausgesprochen kurze Trocknungszeit (ca. 3 Minuten) ermöglicht ein schnelles und problemloses Arbeiten.
	•	Zur Reinigung der Sprühdüse die Dose aufrecht, mit dem Sprühkopf nach oben, solange gedrückt halten, bis nur noch Treibmittel ohne Farbstoff austritt. Verstopfte Düse, von der Dose abnehmen und mit einer Nadel wieder öffnen.
Lieferart:	•	Lieferform: 400 ml Spray — 1 Stück / 6 Stück
Technische Daten	•	Treibgas: — Propan/Butan
	•	Farben: — gelb, weiss, rot
	•	Kenndaten: — bleifrei, cadmiumfrei, aromatenfrei
		Ergiebigkeit (pro Dose): — je nach Untergrund ca. 3 m²
Anmerkungen:	•	Behälter steht unter Druck. Auch nach Gebrauch nicht gewaltsam öffnen oder verbrennen. Darf nicht in die Hände von Kindern gelangen. Aerosol nicht einatmen. Berührungen mit der Haut und den Augen vermeiden. Behälter an einem gut belüfteten Ort aufbewahren. Sprühnebel und Lackdämpfe leicht entzündbar. Nicht gegen Flammen oder auf glühende Gegenstände sprühen. Von Zündquellen fernhalten. Nicht rauchen. Nur in gut belüfteten Bereichen verwenden. Bei Gebrauch Bildung explosionsfähiger/leichtentzündlicher Dampf-Luftgemische möglich. Vor Sonnenbestrahlung und Temperaturen über 50°C schützen. Nur restentleerte Gebinde der Wertstoffsammlung zuführen. Dosen mit Resten bei der Sammelstelle für Altlacke abgeben. EAK-Nr. 150104. Nicht in die Kanalisation gelangen lassen. Wiederholter Kontakt kann zu spröder oder rissiger Haut führen. Dämpfe können Schläfrigkeit und Benommenheit verursachen. Reizt die Augen.
Besondere Hinweise:	•	Weitere Hinweise zur Produktsicherheit und Handhabung entnehmen Sie bitte unserem Sicherheitsdatenblatt

Zur Beachtung:
Vorstehende Angaben können nur allgemeine Hinweise sein. Wegen der außerhalb unseres Einflusses liegenden Verarbeitungsund Anwendungsbedingungen und der Vielzahl unterschiedlicher Materialien empfehlen wir in jedem Fall zunächst ausreichende Eigenversuche durchzuführen. Eine Haftung für konkrete Anwendungsergebnisse kann daher aus den Angaben und Hinweisen in diesem Merkblatt nicht abgeleitet werden.

A.4 Developer

Technical Data Sheet **ARDROX® 9D1B & NQ1**

Non-aqueous liquid developers

1 General Description

Ardrox® 9D1B and NQ1 are liquid suspensions of an inert white powder in a quick drying solvent with low sulfur, halogen and alkali metal content.

Ardrox® 9D1B and NQ1 are used as developers in penetrant testing of forged parts, welds, cast and drop forged parts. Ardrox® NQ1 is designed to offer best results with both color contrast and fluorescent penetrants while the thin layer provided by Ardrox® 9D1B will make it especially suited for fluorescent penetrant testing applications.

Ardrox® 9D1B and NQ1 are available as bulk material and as aerosol. They are typically used together in a penetrant system with the Ardrox® penetrants and developers.

Conformances:

✓ ASME Boiler & Vessel Code	Section V, Article 6
✓ Electricité de France	PMUC (Ardrox® NQ1)
✓ EN ISO 3452-2	Form d & e
✓ Pratt & Whitney	FPM PMC 4357 (Ardrox® 9D1B)
✓ Rolls Royce	RRP 58003
✓ SAE	QPL-2644
✓ SAFRAN	IN-5000

Ask your Chemetall representative for a complete list of approvals

2 Physical and Chemical Properties

		Ardrox®	
Property	Unit	9D1B	NQ1
Appearance	-	White solid particle in a clear liquid	
Density	g/ml @ 20 °C / 68 °F	0.88	0.8
Flash point	°C / °F	-18 / 0	16 / 61

These are typical values only and do not constitute a specification.

3 Method of use

3.1 Pre-cleaning

Clean part with e.g. Ardrox® 9PR5, 9PR50 or 9PR88 before applying Ardrox® penetrant. Apply cleaner to the part and wipe clean with cloth. Surface has to be free of grease, oil and dirt. Allow part to dry before applying penetrant.

3.2 Penetrant

Apply a thin even film of penetrant to cover test area. Allow penetrant 10 – 30 minutes penetration time before removing.

3.3 Penetrant removal

Remove excess surface penetrant with clean cloths, pre-moistened with cleaner (e.g. Ardrox® 9PR5, 9PR50 or 9PR88). Alternatively, removal can be effected by gentle water spray or by rinsing with water (for application over 5°C / 41°F). Do not flush surface with cleaner as sensitivity will be impaired. Repeat procedure until surface penetrant has been removed.

Chemetall expect more

Thoroughly dry the component surface before developer application.

3.4 Developer

Ardrox® 9D1B and NQ1 are solid suspensions of solid particles which settle-out on standing; and therefore aerosols and bulk containers must be shaken thoroughly before and during use.

Spray thin, even developer film over area to be inspected (spraying distance 30 cm / 1 ft.).
Ardrox® 9D1B and NQ1 must be applied by a light even spray as any other method such as immersion or brushing will cause a loss of process sensitivity. When Ardrox® 9D1B is used as part of a Ardrox® fluorescent penetrant process, it should be applied by successive spraying until a translucent layer is achieved and it is possible to see the test surface through the developer film.

Surface temperature should be between -10 and 50°C (15-120°F).
Allow 10 – 30 minutes developing time before evaluation.

For Ardrox® color contrast processes, inspection should be carried out in diffused white light of at least 500 lux (approx. 46 ft.cdl) and in the case of Ardrox® fluorescent penetrant processes under UVA of 365 nm peak wavelength, typical output of 1200 µwatts/cm² at 38 cm from the component.

Attention:
The procedure above is a recommendation only; where relevant, the process specifications of the approving authorities must be followed.

4 Effects on materials

When Ardrox® 9D1B or NQ1 is used in the prescribed manner, no significant corrosion is likely to occur on commonly used constructional metals. Ardrox® 9D1B and NQ1 may cause swelling of some rubbers and plastics, the product should be tested for compatibility before application.

5 Storage

Store in a cool place, with protection from freezing conditions.

6 Safety guidance & waste release

Before operating the process described it is important that this complete document, together with any relevant Safety Data sheets, be read and understood.
All waste waters must be treated in accordance with national legislation and local regulations prior to discharge to the sewer.

7 General information

Chemetall supplies a wide range of chemical products and associated equipment for cleaning, descaling, paint and carbon removal, metal working and protection and non-destructive testing. Sales Executives are available to advice on specific problems and applications.

Issue 2 of September, 2017

Head Office
Chemetall GmbH
Trakehner Straße 3
60487 Frankfurt am Main
Germany

T +49 69 7165 0
F +49 69 7165 3018
surfacetreatment@chemetall.com
www.chemetall.com

Chemetall
expect more

REFERENCES

[1] P. Childs, J. Greenwood, and C. Long, "Review of temperature measurement," *Review of Scientific Instruments*, vol. 71, no. 8, 2000.

[2] P. Ireland and T. Jones, "Liquid crystal measurements of heat transfer and surface shear stress," *Meas. Sci. Technol.*, vol. 11, 2000.

[3] R Poser, J von Wolfersdorf, and E Lutum, "Advanced evaluation of transient heat transfer experiments using thermochromic liquid crystals," *Proceedings of the Institution of Mechanical Engineers, Part A: Journal of Power and Energy*, vol. 221, no. 6, pp. 793–801, 2007. eprint: https://doi.org/10.1243/09576509JPE464.

[4] T Kissel, E Baum, A Dreizler, and J Brübach, "Two-dimensional thermographic phosphor thermometry using a CMOS high speed camera system," *Applied Physics B*, vol. 96, 2009.

[5] M Lorenz, T Horbach, A Schulz, and H.-J. Bauer, "A novel measuring technique utilizing temperature sensitive paint: Measurement procedure, validation, application, and comparison with infrared thermography," *Journal of Turbomachinery*, vol. 135, 2013.

[6] M Martiny, R Schiele, M Gritsch, A Schulz, and S Wittig, "In Situ Calibration for Quantitative Infrared Thermography," *Quantitative InfraRed Thermography, QIRT 96*, 1996, Proceedings of Eurotherm Seminar No. 50, Stuttgart, Germany.

[7] M Ochs, T Horbach, A Schulz, R Koch, and H.-J. Bauer, "A novel calibration method for an infrared thermography system applied to heat transfer experiments," *Measurement Science and Technology*, vol. 20, no. 7, 2009.

[8] M Ochs, A Schultz, and H.-J. Bauer, "High dynamic range infrared thermography by pixelwise radiometric self calibration," *Infrared Physics and Technology*, vol. 53, no. 2, pp. 112 –119, 2010.

[9] M. Ochs, "Filmkühlung transsonischer Turbinen: Infrarot Thermographisches Messverfahren zur Charakterisierung des Wärmeübergangs," PhD Thesis, Karlsruher Institut für Technologie: Institut für Thermische Strömungsmaschinen, 2011.

[10] S. Kyle, T. Luhmann, S. Robson, and J. Boehm, *Close-Range Photogrammetry and 3D Imaging.* Ser. De Gruyter Textbook. De Gruyter, 2013, ISBN: 9783110302691.

[11] J. Lohrengel and R. Todtenhaupt, "Wärmeleitfähigkeit, Gesamtemissionsgrade und spektrale Emissionsgrade der Beschichtung Nextel-Velvet-Coating 811-21 (RAL 900 15 tiefschwarz matt)," *PTB Mitteilungen 4/96*, 1996.

[12] VDI/VDE3511, *Richtlinien - Technische Temperaturmessungen - Strahlungsthermometrie*, Verein Deutscher Ingenieure, 1995.

[13] R. W. Smith and S. C. Gülen, "Natural gas power," in *Encyclopedia of Sustainability Science and Technology*, R. A. Meyers, Ed. New York, NY: Springer New York, 2017, pp. 1–59, ISBN: 978-1-4939-2493-6.

[14] U.S. Energy Information Administration, "Table 1.1. net generation by energy source: Total (all sectors), 2010-february 2020," *Electric Power Monthly*, Apr. 2020.

[15] R. Kehlhofer, B. Rukes, F. Hannemann, and F. Stirnimann, *Combined-Cycle Gas & Steam Turbine Power Plants*, 3rd ed. PennWell Corporation, 2009.

[16] U.S. Energy Information Administration, "Table 1.7.c. utility scale facility net generation from natural gas by technology: Total (all sectors), 2010-february 2020," *Electric Power Monthly*, Apr. 2020.

[17] S. Can Gülen, "Étude on gas turbine combined cycle power plant — next 20 years," *Journal of Engineering for Gas Turbines and Power*, vol. 138, no. 5, Oct. 2015.

[18] H. M. Kwon, S. W. Moon, T. S. Kim, D. W. Kang, J. L. Sohn, and J. Lee, "A study on 65 % potential efficiency of the gas turbine combined cycle," *Journal of Mechanical Science and Technology*, vol. 33, no. 9, pp. 4535–4543, Sep. 2019.

[19] G. Angelino, "Carbon Dioxide Condensation Cycles For Power Production," *Journal of Engineering for Power*, vol. 90, no. 3, pp. 287–295, Jul. 1968.

[20] E. Feher, "The supercritical thermodynamic power cycle," *Energy Conversion*, vol. 8, no. 2, pp. 85 –90, 1968.

[21] V. Dostal, "A supercritical carbon dioxide cycle for next generation nuclear reactors," Sc.D. thesis, Massachusetts Institute of Technology, 2004.

[22] K. Brun, P. Friedman, and R. Dennis, Eds., *Fundamentals and Applications of Supercritical Carbon Dioxide Based Power Cycles*. Woodhead Publishing, 2017.

[23] Y. Ahn, S. J. Bae, M. Kim, S. K. Cho, S. Baik, J. I. Lee, and J. E. Cha, "Review of supercritical co2 power cycle technology and current status of research and development," *Nuclear Engineering and Technology*, vol. 47, no. 6, pp. 647 –661, 2015.

[24] F. Crespi, G. Gavagnin, D. Sánchez, and G. S. Martínez, "Supercritical carbon dioxide cycles for power generation: A review," *Applied Energy*, vol. 195, pp. 152 –183, 2017.

[25] *Investigation of the Bottoming Cycle for High Efficiency Combined Cycle Gas Turbine System With Supercritical Carbon Dioxide Power Cycle*, vol. Volume 9: Oil and Gas Applications; Supercritical CO2 Power Cycles; Wind Energy, Turbo Expo: Power for Land, Sea, and Air, V009T36A011, Jun. 2015.

[26] S. Wright and W. Scammell, "6 - Economics," in *Fundamentals and Applications of Supercritical Carbon Dioxide (sCO2) Based Power Cycles*, K. Brun, P. Friedman, and R. Dennis, Eds., Woodhead Publishing, 2017, pp. 127 –145.

[27] W. Short, D. J. Packey, and T. Holt, *A Manual for the Economic Evaluation of Energy Efficiency and Renewable Energy Technologies*. National Renewable Energy Laboratory, 1995, pp. 47 –50.

[28] Gas Turbine World, "Combined Cycle Plant Prices," in *2014-15 GTW Handbook*. Pequot Publishing, 2015, vol. 31, pp. 47–48.

[29] S. A. Wright, C. S. Davidson, and W. O. Scammell, "Thermo-economic analysis of four sco2 waste heat recovery power systems," in *Supercritical CO2 Power Cycles Symposium*, Mar. 2016.

[30] M. J. Moran, H. N. Shapiro, D. D. Boettner, and M. B. Bailey, *Fundamentals of Engineering Thermodynamics*, 7th ed. John Wiley and Sons, Inc., 2011.

[31] ISO 3977-2:1997, *Part 2: Standard reference conditions and ratings – Gas Turbines – Procurement*. ISO, Geneva, Switzerland.

[32] T. Lindquist, "Evaluation, experience and potential of gas turbine based cycles with humidification," Ph.D. dissertation, Lund University, Sweden, Sep. 2002.

[33] E. W. Lemmon, R. T. Jacobsen, S. G. Penoncello, and D. G. Friend, "Thermodynamic properties of air and mixtures of nitrogen, argon, and oxygen from 60 to 2000 k at pressures to 2000 mpa," *Journal of Physical and Chemical Reference Data*, vol. 29, no. 3, pp. 331–385, 2000.

[34] W. Wagner and A. Pruß, "The iapws formulation 1995 for the thermodynamic properties of ordinary water substance for general and scientific use," *Journal of Physical and Chemical Reference Data*, vol. 31, no. 2, pp. 387–535, 2002.

[35] R. Span and W. Wagner, "A new equation of state for carbon dioxide covering the fluid region from the triple-point temperature to 1100 k at pressures up to 800 mpa,"

Journal of Physical and Chemical Reference Data, vol. 25, no. 6, pp. 1509–1596, 1996.